Università degli Studi di Cagliari

DOTTORATO DI RICERCA

In SCIENZE E TECNOLOGIE CHIMICHE

Ciclo XXVIII

TITOLO TESI

Colloidal $CoFe_2O_4$-based nanoparticles

for Magnetic Fluid Hyperthermia

Settore/i scientifico disciplinari di afferenza

CHIM/03

Presentata da: Valentina Mameli

Coordinatore Dottorato   Prof. Mariano Casu

Tutor   Prof.ssa Carla Cannas

Esame finale anno accademico 2014 – 2015

UNIVERSITY OF CAGLIARI

PhD SCHOOL OF PHARMACEUTICAL AND CHEMICAL SCIENCES AND TECHNOLOGIES

PhD course of Chemical Sciences and Technologies

XXVIII cycle

Colloidal CoFe₂O₄-based nanoparticles for Magnetic Fluid Hyperthermia

SUPERVISOR

PhD. Carla Cannas

CANDIDATE

Valentina Mameli

Acknowledgements

My sincere gratitude first goes to my supervisor Prof. Carla Cannas, who has been since my bachelor thesis an inspiring mentor, a model of strong and independent woman and honest researcher. During these years, she has been always on my side making me grow up by both encouraging and correcting me.

Then, I would like to thank Prof. Anna Musinu for her efforts and suggestions either as head of our research group or for her academic roles.

Great acknowledgements go also to Prof. Giorgio Piccaluga, whose interesting comments are always cause for reflection.

I particularly acknowledge my dear friend Francesca Dalu for being always genuine and for her helpful suggestions.

A special thank goes to my colleagues and friends PhD. Andrea Ardu, Claudio Cara and Marco Sanna, who have been always ready to help me. Moreover, I will not forget the willingness and the helping of PhD. Federica Orrú, PhD. Mauro Mureddu, PhD. Giuseppe Muscas.

Prof. Nguyen T. K. Thanh is particularly acknowledged for having kindly accepted me in her research group at the University College London, for her useful suggestions and for understanding in some difficult moments.

Moreover, I feel necessary to thank all the people who have helped me in the research activity:

- Prof. Guido Ennas (University of Cagliari)
- Prof. Daniel Niznansky (University Charles of Prague)
- PhD. Davide Peddis (Istituto di Struttura della Materia - Consiglio Nazionale delle Ricerche)
- PhD. Claudio Sangregorio (Istituto di Chimica dei Composti OrganoMetallici - Consiglio Nazionale delle Ricerche)
- PhD. Claudia Innocenti (University of Florence)

PhD. Elvira Fantechi is also acknowledged for her kind support and for having shared with me her knowledge.

Finally, I would like to especially thank my family and Cristiano that, with their immense love, have accompanied me during this difficult but enriching "path".

Table of contents

List of figures

List of tables

Introduction

In the field of biomedicine, important issues to address are the early-stage diagnosis and targeted therapies. Since the last two decades, magnetic nanoparticles have been proposed as potentially powerful due to their unique chemical-physical properties. Magnetic nanoparticles can be applied in a wide variety of biomedical fields from the magnetic separation and Magnetic Resonance Imaging (MRI) to drug delivery and Magnetic Fluid Hyperthermia (MFH).(Krishnan, 2010) In particular, MFH is based on the heat released by magnetic nanoparticles subjected to an alternate external magnetic field. Among the different material features affecting the hyperthermic efficiency, the magnetic properties are clearly the most important. Therefore, the optimisation of the magnetic properties, aimed to increase the heating ability and to reduce the magnetic material dose to be inserted in the human body, is still an active research field. In 2013 alone, 682 works have been published in the literature on the topic of magnetic hyperthermia.(Wildeboer et al., 2014)

Despite cobalt toxicity, cobalt-containing materials and especially cobalt ferrite nanoparticles have been proposed as promising heat mediators due to its high anisotropy.(Alphandéry et al., 2011; Baaziz et al., 2014; Fantechi et al., 2015; Joshi et al., 2009; Kim et al., 2008; Kita et al., 2010; Mazarío et al., 2012; Nappini et al., 2015; Pichon et al., 2011; Torres et al., 2010; Veverka et al., 2010)

In this thesis, the results obtained on two different systems, designed with the idea of studying the effect on the hyperthermic properties of proper tuning of the magnetic properties, are presented. Both the sets of samples are based on cobalt ferrite nanoparticles. The first strategy consists on the substitution of cobalt ions with zinc ones with the aim of tuning the magnetic properties of the system and, at the same time, decrease the toxicity of the material. The second way is on the contrary represented by the coating of cobalt ferrite cores by means of biocompatible or less toxic isostructural phases (i.e. magnetite/maghemite or manganese ferrite).

The thesis is divided within five chapters. The introduction session is divided in three different chapters. *Chapter 1* gives a general overview about nanomaterials and their chemical-physical properties. *Chapter 2* is fully dedicated to Magnetic Fluid Hyperthermia (MFH). In *Chapter 3*, the structural and magnetic properties of spinel ferrites are briefly outlined. The experimental session is given in two different chapters. The first one (*Chapter 4*) deals with the study of the magnetic properties and the heating abilities of $Zn_xCo_{1-x}Fe_2O_4$ nanoparticles, synthesised with different zinc content ($0<x<0.6$) but with all the other properties unchanged (i.e. with similar crystallite size, particle size and polydispersity index, same capping agent amount and type). The second chapter (*Chapter 5*) is dedicated to the synthesis, microstructural and hyperthermic properties of cobalt ferrite-based core@shell structures, $CoFe_2O_4@M^{II}Fe_2O_4$, with a shell $M^{II}Fe_2O_4$ of magnetite/maghemite or manganese ferrite. Finally, general conclusions are given.

1 Nanoparticles and their properties

Abstract

In this chapter, a general discussion about nanomaterials and the chemical-physical properties that arise from scaling-down the matter to the nanoscale is given. Particular attention is paid on the description of magnetic nanoparticles and their properties.

1.1 Nanomaterials

The prefix "*nano*" is derived from a Greek word that means *dwarf* so that the term *nanomaterials* refers to materials with at least one dimension ranging between the atomic level (0.2 nm) and 100 nm (1 nanometre = 10^{-9} metres). This class of materials is the bridge between the atoms and the bulk-solids. For this reason, nanomaterials can show different and novel properties in comparison with their bulk-counterparts due to two effects: the higher surface/volume (S/V) ratio and the occurrence of quantum effects. The first effect deals with the chemical reactivity that increases with increasing number of surface atoms, i.e. with increasing S/V (**Fig. 1.1.1**).
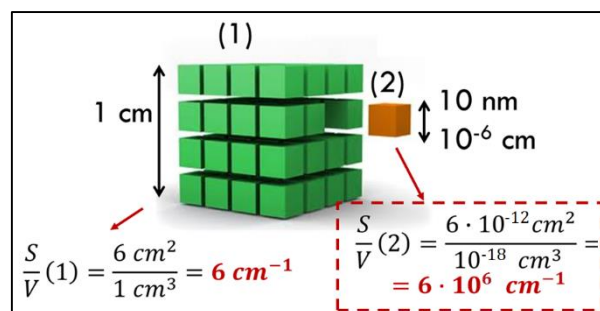
Fig. 1.1.1 Surface/volume (S/V) ratio for a bulk material (1) and a nanoparticle (2).

The second one is particularly important for materials approaching the lower bound of the nanoscale (tens of nanometres) and affects their physical (optical, magnetic, electrical) properties (**Fig. 1.1.2**).
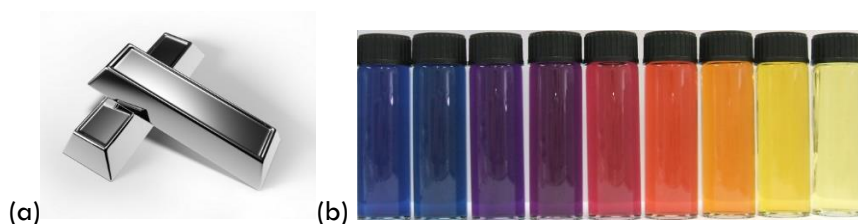
Fig. 1.1.2 (a) Silver ingots (bulk material) and (b) colloidal dispersions of silver nanoparticles of different sizes.(Dalu, 2014)

The comprehension of these phenomena is the subject matter of *nanoscience*.(Dowling et al., 2004)

Depending on how many dimensions are nanosized, nanomaterials can be classified as nanocrystals or nanoparticles (3-D nanoscaled), nanowires and nanotubes (2-D nanoscaled), surfaces and thin films (1-D nanoscaled).(Dowling et al., 2004; Rao and Cheetham, 2001) In addition, two dimensional or three dimensional (superlattices) arrays of nano-objects are considered nanomaterials too.(Rao and Cheetham, 2001)

In 1959, Richard Feynman with his lecture titled "*There's plenty of room at the bottom*" first suggested the idea of "*manipulating and controlling things on a small scale*", i.e. the nanoscale.(Feynman, 1959) This moment is considered as the beginning of *nanotechnology* which concerns with the design, characterisation, production and application of materials by controlling shape and size at the nanoscale.(Dowling et al., 2004) However, nanotechnology is actually older than 50 years. A good example dates back to the fourth century AD with the *Lycurgus cup*, a Roman cup made of a dichroic glass containing silver-gold alloy nanoparticles homogeneously dispersed in the glassy matrix which are responsible for the different colours, green or red, shown when the visible light is reflected or transmitted, respectively.(Barber and Freestone, 1990; Freestone et al., 2007) Gold and silver nanoparticles have been further used in the Middle ages to build the stained glass windows of Gothic cathedrals. Another example concerns the extraordinary mechanical properties of Damascus blades (300-1700 AD) which are ascribed to the presence of cementite elongated nanoparticles and nanowires.(Reibold et al., 2009) It is worth noting that all these craftsmen were not narrowly *nanotechnologists* because they create their nanomaterials by a *trial and error* approach being unaware of controlling the material properties at the nanoscale.

Finally, nature itself is responsible for different nanostructured materials such as the magnetic nanoparticles produced by magnetotactic bacteria(Bellini, 1963a, 1963b; Blakemore, 1975), the nanofibers in the gecko's feet that allow it to hang upside down or on inclined surfaces(Autumn et al., 2002) and the hair-like nanostructures found in the lotus leaves responsible for self-cleaning mechanisms.(Cheng et al., 2006)

1.2   Magnetic nanoparticles

As mentioned in the paragraph **1.1**, the magnetic properties are among those physical properties that dramatically change within the nanoscale. Indeed, when the size of a ferromagnetic material is scaled down to create a nanoparticle (i.e. a 3D nanoscaled object), peculiar magnetic phenomena emerge. Pierre Weiss in 1907 first described the magnetic structure of a *bulk*-ferromagnet by the presence of sub-domains consisting of aligned moments inside each domain but unaligned moments among different domains (Weiss, 1907). In this view, these magnetic domains are clearly separated by highly disordered regions called domain walls. This multi-domain structure is favoured as long as the magnetostatic energy is higher than the domain wall energy. Being the magnetostatic and the domain wall energy proportional to the volume and the surface of the material, respectively, the relative extent of these two energy contributions depends on the S/V ratio. In particular, when the particle size drops down to a critical value called "*radius for single domain*" (r_{sd}), a multi-domain magnetic structure is no longer energetically convenient due to the high wall domain energy. To minimise it, a single-domain magnetic structure is instead established, i.e. each particle is composed by a unique uniformly

magnetised region and is characterised by a magnetic moment $m \approx 10^3$-10^5 μ_B (μ_B is the Bohr magneton defined as $\mu_B = e\hbar/2m_e$ and equal to $9.274 \cdot 10^{-24}$ Am^2), thus leading to the label "*superspins*".

This critical radius, r_{sd}, depends on the properties of the material, such as anisotropy constants (A, K_u) and saturation magnetisation (M_s) according to the equation:

$$r_{sd} \approx 9 \frac{\sqrt{A \cdot K_u}}{\mu_0 M_s^{\,2}}$$

Eq. 1.2.1

For this reason, this property can be considered specific for each material.

Another critical radius called "*radius for superparamagnetism*" is the size under which a ferromagnetic materials exhibits a zero coercivity, the magnetic cooperative properties are lost and a paramagnetic behaviour is established (**Fig. 1.2.1**). All these critical sizes fall within the nanoscale, as shown in **Tab. 1.2.1** for different magnetic materials.
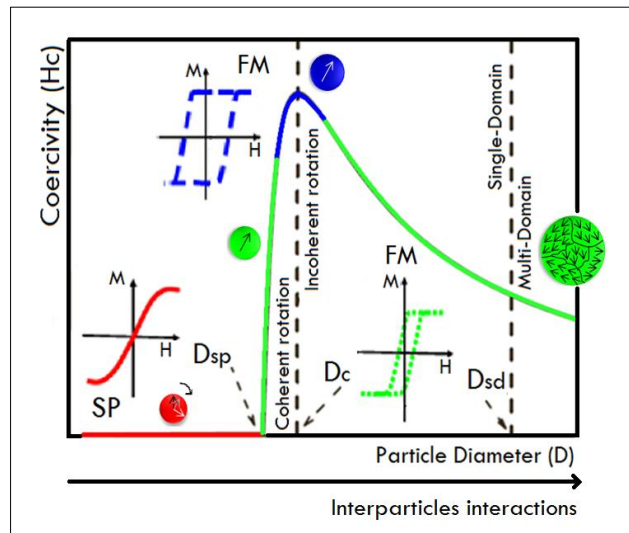
Fig. 1.2.1 Variation of the coercive field with nanoparticle size.

Tab. 1.2.1 Magnetic properties of various bulk materials estimated at room temperature (Coey, 2010; Cullity and Graham, 2009; Thuy et al., 2012). *Maghemite (γ-Fe$_2$O$_3$) reverts to hematite (α-Fe$_2$O$_3$) above 800 K.

Materials	K_u (10^5 erg·cm^{-3})	M_s (emu cm^{-3})	T_c (K)	r_{sd} (nm)	r_{SP} (nm)
bcc-Fe	4.8	1745.9-1714	1044	15	10
fcc-Co	41	1460.5	1388	30	10
hcp-Co	27	1435.9	1360	34	-
FeCo	-	1910	-	50	10
Fe$_3$Co	-	1993	-	-	10
γ-Fe$_2$O$_3$	-0.5	380	985*	30	20
Fe$_3$O$_4$	-1.3	415-480	840	38	15
CoFe$_2$O$_4$	29	425	790	-	-
MnFe$_2$O$_4$	-0.3	400	575	-	-

Single-domain nanoparticles (NPs) act as single magnetic moments (i.e. superspins) that are able to reproduce in "a bigger scale" different magnetic behaviours (*paramagnetism*, *spin-glass*, *ferromagnetism*) as the atomic magnetic moments do. The occurrence of these supermagnetic behaviours (*superparamagnetism*, *super spin glass*, *superferromagnetism*) is affected by the relative strength of inter-particle interactions and thermal energy. Indeed, non-interacting NPs act independently and the thermal energy is sufficient to disorder the superspins. To be more precise, usually single-domain NPs are characterised by the existence of particular directions along which the magnetisation process easily occurs (*easy-axes*). Therefore, the parallel or antiparallel alignment of the magnetisation with respect to this axis represent energy minima conditions. For instance, uniaxial particles with an anisotropy energy equal to $E = KV \sin^2 \theta$, where K is the anisotropy constant, V is the particle volume and θ is the angle between the magnetisation and the easy axis, shows two minima energy for a parallel and an antiparallel alignment of the magnetisation with respect to the easy axis, i.e. $\theta = 0$ and $\theta = 180°$. When the energy barrier $\Delta E = KV$ is lower than the thermal energy ($k_B T$) and the particles do not interact each other, the magnetisation can fluctuate between these two energy minima, giving rise to a superparamagnetic behaviour (**Fig. 1.2.2**). When the energy barrier becomes higher than the thermal energy (note that ΔE increases with increasing anisotropy constant or particle volume), this spin-flip process is no more possible and the magnetisation will be blocked on a certain minimum.
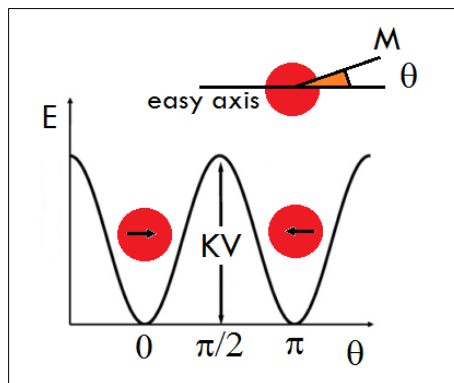
Fig. 1.2.2 Energy profile of a single-domain particle with uniaxial anisotropy as a function of the angle θ between the magnetization and the easy axis magnetization direction.

Nevertheless, it is worth noting that the magnetisation reversal is a dynamic process with a characteristic time necessary to overcome the energy barrier. This time is known as the *Néel-Brown relaxation time* and exponentially depends on the ratio between the energy barrier and the thermal energy, as follows:

$$\tau_N = \tau_0 e^{KV/k_B T}$$

Eq. 1.2.2

Where τ_0 is the characteristic relaxation time.

For a certain anisotropy constant and a certain particle volume, a system of NPs can show either a superparamagnetic or a blocked state according to the relative extent of the relaxation time (τ_N) and the

measurement time (τ_m). In other words, depending on the measurement timescale, a superparamagnetic state will be exhibited at a different temperature. The temperature at which the relaxation time is equal to the measurement time is called *blocking temperature* (T_B) and such a definition implies that this quantity is not an intrinsic property of the material:

$$T_B \approx KV/k_B \, ln(\tau_m/\tau_N)$$

Eq. 1.2.3

Therefore, when $\tau_m \gg \tau_N$ the NPs show superparamagnetic behaviour whereas when $\tau_m \ll \tau_N$ the NPs appear to be blocked.

As before-mentioned, the superparamagnetism translates into a linear magnetic field dependence of the magnetisation with a zero coercivity similarly to a paramagnet (**Fig. 1.2.3a**) and an S-shaped curve (**Fig. 1.2.3b**). On the contrary, NPs in a blocked state are responsible for an hysteresis loop (**Fig. 1.2.3c**).
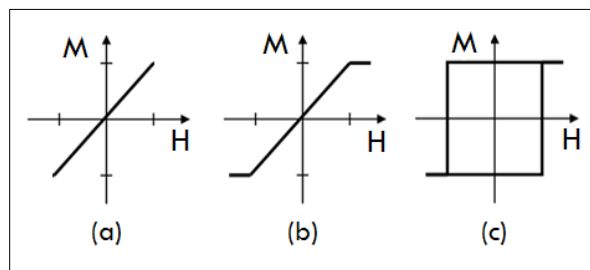
Fig. 1.2.3 *Magnetisation versus magnetic field curves (M vs H) for a paramagnet (a), a superparamagnet (b) and a ferro/ferrimagnet (c).*

Contrary to superparamagnetic NPs, interacting single-domain ones provides a collective responses because the particles affect each other's behaviour. This happens with different extent in *super spin glass* systems and *superferromagnetic* ones.(Bedanta and Kleemann, 2009)

1.3 Biomedical applications of magnetic nanoparticles

Early diagnosis and targeted therapies are fundamental questions in the field of biomedicine. The development of new technologies designed to answer to these issues has strongly driven the research in this field. Since the last two decades, magnetic nanostructured materials have been proposed as suitable platforms due to their novel chemical-physical properties for *in vivo* and *in vitro* diagnostic, therapeutic and theranostic purposes.(Krishnan, 2010)

The use of magnetic nanoparticles in biomedicine provides different novel functionalities:

- Having sizes smaller or comparable to those of different biological entities (a cell (10–100 μm), a virus (20–450 nm), a protein (5–50 nm) or a gene (2 nm wide and 10–100 nm long)), they can directly interact with them;

- Being magnetic, they can be remotely controlled by an external magnetic field;

- Being magnetic, they can be responsible for an energy transfer in the tissue as a result of the application of an AC magnetic field.(Pankhurst et al., 2003)

Clearly, some requirements are necessary for a magnetic material to be applied in this field:

- non-toxicity;

- biocompatibility;

- biodegradability;

- good response to the applied magnetic field;

- negligible remnant magnetisation when the external field is turned off;

- the smallest size as possible to increase the surface area available for the functionalisation;

- well-defined morphological properties (particle size, size distribution);

- good microstructural properties (crystallinity);

- chemical stability;

- colloidal stability;

- ease of production;

- low cost.

Different specific biomedical applications of magnetic nanoparticles have been identified such as magnetic separation, Magnetic Resonance Imaging (MRI), drug delivery and Magnetic Fluid Hyperthermia (MFH).(Pankhurst et al., 2003)

The basic principles of these applications are briefly described in the following paragraphs with the exception of Magnetic Fluid Hyperthermia that is discussed in detail in Chapter 2.

1.3.1 Magnetic separation

For numerous biological and biomedical assays and analyses, it is necessary to separate specific biological entities from their original environment. Magnetic separation can be applied with this aim. The biological entities need first to be labelled with the magnetic material by a proper surface functionalisation with molecules as dextran, polyvinyl alcohol (PVA) and phospholipids. Then, the fluid passes through a magnetic field gradient which stops the labelled entities. Nanoparticles are preferred with respect to the microparticles because their magnetophoretic mobility is lower and the separation can be carried out rapidly. Moreover, the reduced size permits a lower interference with successive tests on the separated entities.(Pankhurst et al., 2003)

1.3.2 Magnetic Resonance Imaging (MRI)

Among other techniques, MRI has become dominant in the non-invasive imaging of soft-tissues. It is based on the nuclear magnetic resonance of the protons of the water present in the body. Although the proton magnetic moment is small, the high proton density in the body can be exploited to get high resolution images of internal organs. Indeed, the available proton moments per mm^3 are $2 \cdot 10^{14}$, producing a net magnetisation when an intense static magnetic field (B_0, longitudinal field) is applied due to the parallel alignment of the proton moments in the field direction (z-axis). More precisely, the protons moments start to spin around B_0 field at a Larmor precession frequency ($\omega_0 = \gamma B_0$) that fall in the radiofrequency range (for $B_0 = 1T$, $\omega_0 = 43$ MHz).

When the transverse field gets back to zero, relaxation processes of the longitudinal and transverse magnetisations occur with characteristic times called T_1 and T_2, respectively. The profiles of the magnetisation components are described by the following equations:

$$M_z = (1 - e^{-t/T_1})$$

Eq. 1.3.1

$$M_{xy} = m\,sin(\omega_0 t + \phi)e^{-t/T_2}$$

Eq. 1.3.2

The longitudinal and transverse magnetisations relax by spin-lattice dipolar interactions and spin-spin interactions, respectively. From these relaxation processes is possible to reconstruct the magnetic resonance images, which contrast strongly depends on T_1 and T_2.

In T_1-weighted images, water is darker than fat whereas the opposite contrast is obtained for T_2-weighted images. However, in many tissues, the intrinsic contrast is not sufficient and external agents are used to improve it. Contrast agents usually shorten the relaxation times T_1 (positive contrast agents) or T_2 (negative contrast agents). Paramagnetic ions complexes of gadolinium are typical T_1 contrast agents but a serious drawback in their use is the tendency to accumulate in the liver. Among T_2 agents superparamagnetic (usually iron oxides) nanoparticles are used because they are able to generate a secondary magnetic field that render faster the relaxation process of the transverse magnetisation.(Krishnan, 2010; McNamara and Tofail, 2015; Pankhurst et al., 2003; Yoo et al., 2011)

1.3.3   Drug delivery

Magnetically targeted drug delivery is another important biomedical application of magnetic nanoparticles that can be used as carriers for anti-cancer drugs. A ferrofluid containing the drug/carrier system is first intravenously or intra-arterially injected into the patient and, once a magnetic field has conducted it to the target tissue, the drug is released by means of enzymatic activity or a physiological variation for instance in the pH or temperature.

This therapy aims to sort out some of the main drawbacks of conventional chemotherapy, making the treatment more specific and effective, avoiding side effects on the healthy tissues and reducing the necessary dosage. These objectives can be reached by means of an appropriate functionalisation of the nanoparticles surface by active or passive targeting. The former is based on the conjugation with antibodies, ligands or aptamers that can be recognised by specific receptors present in the tissues. The latter is based on the preferential accumulation of nanoparticles within cancer tissues (Enhanced Permeability and Retention effect) or by intra-tumour injections.

2   Magnetic Fluid Hyperthermia

Abstract

After a brief introduction about the cancer and the conventional anti-cancer therapies, this chapter will be dedicated to *hyperthermia*, i.e. heating up of tumour tissues aimed to damage or kill cancer cells. The possibility of using magnetic nanoparticles (MNPs) in the form of ferrofluids as heat mediators for moderate hyperthermia treatments (41-46 °C), have defined the so-called Magnetic Fluid Hyperthermia (MFH). This therapy has potentially great advantage since it would be no*n-invasive* due to reduced size of the heat mediators and *selective* due to the intrinsic higher thermal sensitivity of cancer cells with respect to the healthy ones. The different heat release mechanisms from magnetic nanoparticles will be discussed together with the description of the experimental method used to measure their hyperthermal ability. Finally, a paragraph will aim to summarise the main literature results.

2.1   What is cancer?

Cancer, *malignant tumour*, *neoplasm* are generic terms referring to a group of about two hundred diseases characterised by a rapid growth of abnormal cells through uncontrolled and anomalous mechanisms. During their growth, these cells start to differentiate increasingly from the healthy ones.(AIOM and AIRTUM, 2012; World Health Organisation, 2015) Cancer is the result of a multi-stage process from one single cell that transforms into a tumour one. Usually, the starting point is a pre-cancer lesion.(World Health Organisation, 2015) It can be caused by both internal and external factors. Gene mutations, hormones, immune defence system functionalities are internal causes whereas the external carcinogens can be physical (radiations), chemical (food or drinking water contaminant, asbestos, tobacco components) or biological (infections agents).(AIOM and AIRTUM, 2012; World Health Organisation, 2015) Obviously ageing is another key factor.

Although remarkable progress has been made in cancer therapy, cancer is still one of the leading causes of death worldwide. In 2012, 8.2 million deaths and 14 million new cases have been recorded. The most common tumours affect lungs (1.59 million deaths), liver (745 000 deaths), stomach (723 000 deaths), colon-rectum (694 000 deaths), breast (521 000 deaths) and oesophagus (400 000 deaths).(World Health Organisation, 2015)
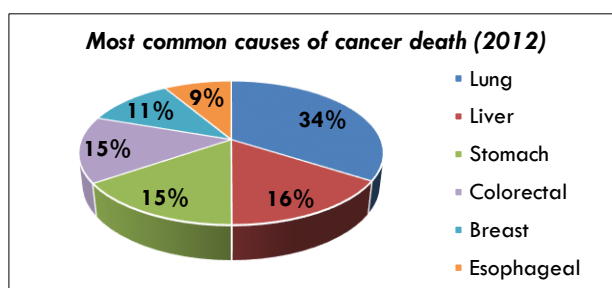
Fig. 2.1.1 Worldwide most common causes of cancer death in 2012.(World Health Organisation, 2015)

Estimates indicate 22 million of new cases in the next two decades.(World Health Organisation, 2015)

In Italy, malignant tumours represent one of the principal causes of death. Among them, the trachea, bronchi, lung tumours have caused 33 538 deaths in 2012, being the fourth cause of death overall and the second one for males.(*Anno 2012 Le principali cause di morte in italia*, 2014)

2.2 How to treat cancer?

Among the various oncological therapies, *surgery* is the oldest one. It is also used as a diagnostic tool to determine the stage, the extent and amount of disease. Surgery can be classified as:

- *Diagnostic* surgery with the aim of getting a tissue sample to be tested;
- *Staging* surgery with the aim of detecting the disease stage;
- *Prophylactic* surgery with the aim of removing a tissue that is not malignant but which may become malignant;
- *Curative* surgery with the aim of removing a tumour tissue;
- *Palliative* surgery with the aim of treating complications and/or pain.

Surgery is often carried out in combination with other therapies, such aschemotherapy or radiotherapy.

Radiotherapy uses high-energy radiations as X-rays or γ-rays to destroy cancer cells by stopping their dividing process. A drawback of this therapy is that it also affects other rapidly dividing cells as mouth, hair and blood cells (white cells, red cells). Radiotherapy is usually administered over an extended period of time (e.g. every weekday for 6 weeks) by either external focusing of the beam in the targeted tissue (*external radiotherapy*) or internal radioactive materials (*brachytherapy*).

The use of specific drugs to treat cancer is called *chemotherapy* and, as radiotherapy does, it stops the cell division. Chemotherapeutic agents can be alkylating agents, antimetabolites, and enzyme inhibitors and are usually given in cycles from 3 months to 3 years with some rest periods in between.

Both radio- and chemotherapies can be used in combination with surgery, before or after it to reduce the tumour size (*neoadiuvant*) or to hinder relapses (*adiuvant*), respectively.

Other therapies are *hormone therapy*, which slows down or inhibits the production of certain hormones that favour the cancer growth, *biological therapies* (e.g. the *immunotherapy* promotes and supports the body immune system), which act directly in the cell biological processes. Finally, other more recently developed treatments are *antiangiogenesis*, *photodynamic* and *gene therapies* and *bone marrow* and *stem cell transplantations*.("Associazione Italiana per la Ricerca sul Cancro (AIRC)," n.d., "Cancer Research UK," n.d.; Foote, 2005)

Unfortunately, despite the extraordinary successes achieved by Cancer research, cancer is still a global big issue to deal with (see paragraph 2.1 for some statistical data). In particular, problems are related to the ineffectiveness of the therapies in some cases as well as the extremely rapidity of cancer to become resistant to them. Also, it cannot be ignored that the main oncological therapies show a high number of side effects both temporary or long-term, from anemia to appetite loss, cognitive problems, clotting problems, constipation, dehydration, dental and oral health problems, diarrhoea, hair loss, skin problems, osteoporosis, nervous system

side effects, nausea and vomiting, pain, fatigue, etc.("American Cancer Society," n.d., "Associazione Italiana per la Ricerca sul Cancro (AIRC)," n.d.)

2.3 Hyperthermia

Conventional therapies (surgery, radiation, chemotherapy, immunotherapy) for treating cancer are still ineffective in some cases, especially for some solid tumours.(Baronzio and Hager, 2006) In addition, they are characterised by some serious drawbacks as invasiveness, non-selectivity and toxicity so that they are always accompanied by side effects, as described in the previous paragraph 2.1. Often, the tolerable toxic level of the patient to radiotherapy or chemotherapy restricts their applications creating a gap between the tolerance and the beneficial destruction.(Baronzio and Hager, 2006) Heating of tumour tissues within 41°C-46°C by means of external mediators, known as *hyperthermia*, is considered the fifth cancer therapy due to the synergistic effect obtained when it is provided with the traditional treatments.(Baronzio and Hager, 2006; van der Zee, 2002) It is considered as a potential bridging therapy able to fill the gap between the tolerable toxicity and the desirable benefits, due to its low toxicity.(Baronzio and Hager, 2006) To be more precise, this kind of thermal treatment should be called *moderate hyperthermia* in order to be distinguished from others associated with lower or higher temperature reached during the treatment. The *adjuvant hyperthermia* is characterized by temperatures lower than 41°C, whilst the *thermo ablation* is the heating to a temperature higher than 56°C and implies cell death by necrosis, coagulation and carbonization of the exposed tissue.(Jordan et al., 1999) Hereafter, the term "*hyperthermia*" will be used referring to the *moderate hyperthermia*.

In Europe, many trials have been carried out demonstrating the effectiveness of this therapy and the reduction of collateral effects. If used alone, it can destroy or damage cancer cells, being responsible for antineoblastic and immunological effects, whereas it renders them more sensitive to radiations or chemotherapeutic agents if coupled with other strategies.(Baronzio and Hager, 2006)

The basis of the efficacy of hyperthermia in treating cancer is represented by different studies showing the higher heat-sensitivity of cancer cells in comparison to the healthy ones.(Cavaliere et al., 1967; Roti Roti, 2008) Clearly, this feature could render in principle hyperthermia more selective than other common treatments, keeping most normal tissues undamaged after treatment for 1 hour at a temperature up to 44 °C.(Fajardo, 1984; van der Zee, 2002) Cancer physiology is different from the normal cells one. A disordered vasculature with hypoxic, acidic and energy lacking regions are typical features of solid tumours.(van der Zee, 2002) Concerning the vasculature, it is worth to note that, actually, the blood flows is not the same in all the tumour types and even in the same one, it can be locally different. Moreover, tumour tissues can be characterised by lower or higher blood flows than that in normal tissues. Usually, the blood flow decreases with increasing tumour size due to damages of the blood vessels and a rapid growth of the cancer tissues nearby them. Nevertheless, heating induces a deterioration of the vasculature system within tumour tissues making them less able to dissipate the thermal energy and reaching higher temperature, responsible for a greater damage when compared to normal tissues.(Song, 1984)

Although the exact mechanisms of cell injury is still not completely known, it seems that hyperthermia induces cell death by apoptosis and that the main damage is protein denaturation.(Hildebrandt et al., 2002; Lepock, 2003)

Commonly, cell death may occur by necrotic or apoptotic processes. *Necrosis*, involving cell swelling, plasma membrane rupture and leakage of the cell content, causes changes or losses of the cell structure and an in vivo inflammatory response.(Fairbairn et al., 1995; Lawen, 2003) *Apoptosis* is a physiological form of cell death in response to an environmental (physiological or pathological) stimulus without an inflammatory response and the cell membrane breakage. It requires metabolic energy and often causes DNA fragmentation.(Fairbairn et al., 1995; Kerr et al., 1972; Lawen, 2003) Apoptosis dying cells are targeted by surface markers by phagocytes and selectively removed.(Fairbairn et al., 1995) Kerr *et al.* in 1972 first proposed the term "apoptosis" indicating the morphological changes they observed by electron microscopy.(Kerr et al., 1972) Apoptosis especially refers to different biochemical and physical changes of the cytoplasm, nucleus and plasma membrane and it does not correspond, as commonly believed, to the Programmed Cell Death which occurs during developments of organisms via apoptotic processes.(Kerr et al., 1972; Lawen, 2003) In addition, apoptosis can be detected also in untreated malignant tumours and in their regression after hyperthermia, radio- and chemotherapies.(Hervault and Thanh, 2014; Kerr et al., 1972) Indeed, different studies demonstrated the induction of apoptosis by moderate hyperthermia.(Barry et al., 1990; Fairbairn et al., 1995; Harmon et al., 1991; Lim et al., 2006; Mack, Y. Rong, 2000; Papadimitriou and Van Bruggen, 1993; Shchepotin et al., 1997; Takano et al., 1991; van Bruggen et al., 1991) As already mentioned, it seems that the main involved mechanism is probably protein denaturation as the thermal energy at temperatures higher than 40°C is close to the energy needed for protein denaturation in cytoskeleton and membranes and enzyme complexes for DNA synthesis and repair.(Hervault and Thanh, 2014; van der Zee, 2002) Moreover, it is known the synergistic effect observed as a result of the close sequential application of radiotherapy or chemotherapy with hyperthermia.(Baronzio and Hager, 2006; van der Zee, 2002) The radiosensitisation seems to be increased by heat probably because of two phenomena. First, an increase of the blood flow due to heat may improve the tissue oxygenation.(Song et al., 2001; van der Zee, 2002) Secondly, being the cellular repair mechanisms of DNA damages seriously compromised by hyperthermia, radiotherapy results to be more effective.(Dikomey, H. H. Kampinga, 2001; van der Zee, 2002) The improved effectiveness of chemotherapy due to hyperthermia is on one hand again related to an increase of blood flow that permits higher concentration of anti-cancer drugs within the tumour tissue and, on the other hand, can be the direct effect of drugs with improved efficacy by heat, for instance caused by a higher intracellular uptake.(van der Zee, 2002)

Another interesting effect of hyperthermia on tumour cells is the angiogenesis inhibition. Angiogenesis is the production of new vessels from pre-existing ones by which the tumour receives the necessary nutrition and oxygenation to progress.(Baronzio and Hager, 2006; Iyer et al., 2006) However, the neo-blood vessels have defective architecture, being irregular in shape, dilated, leaky or defective, and the endothelial cells are poorly aligned or disorga- nized with large fenestrations.(Iyer et al., 2006) Heating above 42 °C acts by hindering endothelial cell (EC) differentiation by three mechanisms: direct cytotoxicity on proliferating ECs, down-modulation of vascular endothelial growth factor (VEGF) production by tumor cells and induction of the plasminogen activator inhibitor-1 (PAI-1) expression. Despite the impressive biological effects of hyperthermia,

the medical community appears to be somehow sceptical to it due to the not negligible technical problems related to *deepness*, *focusing*, *reproducibility*, *control* and *personalisation*.(Baronzio and Hager, 2006)

In dependence on how extended is the part of the body to treat, hyperthermia is classified as:

- *Whole body hyperthermia*, if the treatment affects the entire patient;
- *Regional hyperthermia*, when a substantial region surrounding the tumour tissue is treated;
- *Local hyperthermia*, if the heating is restricted to the tumour volume.

Another classification is usually based on the kind of technology used to deliver heat, i.e. contact or contactless:

1. contact with a heat mediator:
    a. superficial applicators;
    b. interstitial (needles, antennas, catheters, ferromagnetic seeds);
    c. extracorporeal circulation of hot blood in an organ;
    d. thermostatic bath (whole body hyperthermia);
2. contactless:
    a. ultrasound waves (0.3-3 MHz);
    b. radiofrequencies (0.1-100 MHz);
    c. microwaves (100-2450 MHz).

The interstitial mediators can be capacitive or inductive according to the main component of the electromagnetic field, i.e. electric or magnetic, respectively.(Fantechi, 2014)(Baronzio and Hager, 2006; Fantechi, 2014; Strohbehn and Douple, 1984)

The above-cited technical limits of *deepness*, *focusing*, *reproducibility*, *control* and *personalisation* characteristic of these methods together with *invasiveness* (at least in some cases where a surgical implantation is necessary) have act as the driving force in this research field oriented towards more suitable technological solutions, as for instance nanostructured heat mediators as will be described in the following paragraph (**2.4**).

2.4 Magnetic Fluid Hyperthermia (MFH)

2.4.1 Basis

The use of magnetic nanoparticles (MNPs) in the form of ferrofluids (i.e. colloidal dispersions) as heat mediators for moderate hyperthermia treatments, defines the so-called Magnetic Fluid Hyperthermia (MFH).(Krishnan, 2010; Laurent et al., 2008) The process involves two steps. The first one consists in the introduction of the MNPs within the tumour tissue through intratumour or intravenous injections. The second one corresponds to the application of an external alternate magnetic field with proper frequency f and amplitude H_0.(Mehdaoui et al., 2011) Under this AC magnetic field, the MNPs continuously convert the electromagnetic energy into heat.

The first research group dealing with the application of nanotechnology to oncology is *Dr. Andreas Jordan*'s one from *Charité - University Medicine Berlin*. These pioneer researchers in 1993 tested single domain ferrite NPs (1-10 nm) in comparison with multi-domain ones (1-300 μm) for hyperthermia, demonstrating the superiority

of the single domain particles.(Jordan et al., 1993) Since this publication, the company MagForce® Nanotechnologies GmbH have been founded in Berlin and many clinical trials have been conducted. In the chapter titled "*Thermotherapy and Nanomedicine: Between Vision and Reality*" of the book "*Hyperthermia in Cancer Treatment: A Primer*"(Baronzio and Hager, 2006), Dr. Andreas Jordan clearly describes the exclusive advantages of the use of NPs for MFH:

1. High released thermal energy per applied mass;
2. High surface that permits a proper functionalisation with targeting molecules;
3. High depth of penetration within the tumour tissue:
4. If properly coated, NPs can:
    a. Be late recognised by the immune system and, consequently, be able to reach the target tissues;
    b. Be highly uptaken by cancer cells;
    c. Be dispersed in water in the form of low-viscosity colloidal dispersions;
    d. Stay for long time in the tumour tissue.

Therefore, potentially, MFH could be n*on-invasive* due to reduced size of the heat mediators and *selective* due both to the intrinsic higher thermal sensitivity of cancer cells with respect to the healthy ones (see paragraph 2.3) and to the *Enhanced Permeability and Retention (EPR)* effect. The latter represents a preferential accumulation within the tumour tissues of small systems (such as macromolecules or nanoparticles) caused by anatomical abnormalities of solid tumours (extensive angiogenesis, defective vascular architecture, insufficient lymphatic clearance, etc...).(Iyer et al., 2006) Finally, the use of ferrofluid should, in principle, allow to *magnetically transport* the MNPs in the targeted tissue by intravenous injection making possible the treatment of small tumours or metastasis of basically every region of the body.(Baronzio and Hager, 2006)

To date, NanoTherm™ therapy by MagForce® Nanotechnologies GmbH is the only MFH-based therapy approved by European regulatory for the treatment of brain tumour. The heat mediators are made by ~15 nm iron oxide with an aminosilane coating, that are directly injected in the tumour. Different clinical trials are carried out by this company on the treatment of glioblastoma multiforme (80 patients), prostata cancer (29 patients), esophageal cancer(10 patients), pancreatic cancer (7 patients) and other indications (~20 patients).("http://www.magforce.de/en/home.html," n.d.)

2.4.2   Heat Generation Mechanisms and Theoretical models

Heat poduction by MNPs can involve either hysteresis losses or relaxation ones depending on the material features and on their magnetic structure. Multi-domain or blocked single-domain nanoparticles (ferromagnetic nanoparticles, FM), being responsible for hysteretic magnetic responses, are characterised by hysteresis losses. The power per unit of volume is given by the product of the frequency f and the hysteresis loop area $\mu_0 \oint H dM$:

$$P_{FM} = \mu_0 f \oint H dM$$

Eq. 2.4.1

For FM materials, other contributes, commonly considered negligible in the case of MFH, are low frequency losses as eddy-currents and high-frequency losses related to the ferromagnetic resonance.(Pankhurst et al., 2003) Eddy-currents losses are produced in conductive material at the centimetre or larger scale where closed currents occur because of an alternating magnetic flux. They are irrelevant in the range of frequencies normally used in hyperthermia treatments and for nanoparticles(Deatsch and Evans, 2014; Jordan et al., 1993; Pankhurst et al., 2003), being dependent on the radius a of the ferromagnetic seed:

$$P_{eddy} \sim \pi a (\pi f \mu / \sigma_{FM})^{1/2} H_0^2 L$$

Eq. 2.4.2

where a is the radius and L the length of the seed, μ is the magnetic permeability, σ_{FM} is the conductivity of the ferromagnetic material, f is the frequency and H_0 is the amplitude of the external magnetic field.(Stauffer et al., 1984) Losses due to the ferromagnetic resonance are considered negligible too in the commonly used frequency range (below the GHz range). $P_{FM} = \mu_0 f \oint H dM$ indicates that the hysteresis loop area do not depend on the frequency. This makes possible, in principle, to determine P_{FM} by quasi-static measurements (VSM or SQUID magnetometers). However, this equation suggests that the maximum thermal energy delivered by such systems corresponds to rectangular loops that can be obtained only by perfectly aligned uniaxial NPs, a utopian condition to be achieved *in vivo*. Indeed, for real systems only a 25 % of the ideal power can be obtained. Moreover, fully saturated loops are produced only at high field amplitudes, that cannot be used for clinical application, whereas the unsaturated loops are responsible for limited heating.(Pankhurst et al., 2003)

The theoretical model known as the *linear response theory* (LRT) describes the heat release of colloidal superparamagnetic nanoparticles (SPM).(de la Presa et al., 2012) In 2002, Rosensweig developed the analytical treatment, by which the heat release of SPM NPs depends on the out-of-phase χ" component of their magnetic susceptibility(Rosensweig, 2002):

$$P_{SPM} = \pi \mu_0 f H_0^2 \chi"$$

Eq. 2.4.3

which physically means that the magnetic energy is positively converted into internal energy when magnetisation lags the magnetic field.(Pankhurst et al., 2003)

Being

$$\chi" = \chi_0 \frac{2\pi f \tau}{1 + (2\pi f \tau)^2}$$

Eq. 2.4.4

the following equation is obtained:

$$P_{SPM} = \pi \mu_0 f H_0^2 \chi_0 \frac{2\pi f \tau}{1 + (2\pi f \tau)^2}$$

Eq. 2.4.5

where τ is the *effective relaxation time*.

The dependence from the material's features can be further pointed out by substituting $\chi_0 = \frac{\mu_0 M_S^2 V}{3 k_B T}$ in (**Eq. 2.4.5**):

$$P_{SPM} = \frac{\pi \mu_0^2 M_S^2 V f H_0^2}{3 k_B T} \frac{2\pi f \tau}{1 + (2\pi f \tau)^2}$$

Eq. 2.4.6

Where M_S is the saturation magnetisation and V is the particle volume. (Hergt et al., 2010; Shliomis, 1974)

The relaxation of SPM NPs can involve both Nèel and Brown mechanisms involving the reversal of the magnetisation vector inside the nanoparticle (Nèel) or through the physical rotation of the particles themselves (Brown), respectively. Therefore, the effective relaxation time τ depends on the relaxation times characteristic for the two mechanisms (τ_N, τ_B) in agreement with the following equation:

$$\frac{1}{\tau} = \frac{1}{\tau_N} + \frac{1}{\tau_B}$$

Eq. 2.4.7

Where $\tau_N = \tau_0 e^{KV/k_B T}$ and $\tau_B = \frac{3\eta V_H}{k_B T}$.

In particular, this equation indicates that the shortest the relaxation time the highest the contribute is. The relative influence of the mechanisms depends on the size and magnetic properties of the NPs but also on the medium. Generally, Néel relaxation is the major contribution for small particles whereas Brownian relaxation dominates for big ones.

The relationship for P_{SPM} is valid only for a monodisperse system. In order to describe the heat released power per volume unit from a log normal distributed NPs assemble, P_{SPM} should be numerically integrated over the size distribution, $g(R)$:

$$\overline{P_{SPM}} = \int_0^\infty P_{SPM}\, g(R) dR$$

Eq. 2.4.8

Where $g(R) = \frac{1}{\sqrt{2\pi}\sigma R} exp\left[\frac{-(lnR/R_0)^2}{2\sigma^2}\right]$ is the *log normal* function.(Rosensweig, 2002)

It is worth to note that the linear response theory is valid only for superparamagnetic nanoparticles with a linear-frequency dependence and a square-amplitude dependence from the applied magnetic field.

Beside the validity fields of the hysteretic losses model and the linear response theory, real systems often show both types of losses, especially if they are nearby the transition region between the superparamagnetic regime and the ferromagnetic one. Carrey et al. have discussed this topic in a recent article, providing another approach for the computation of the hysteresis area of a single-domain particle and highlighting the key-role of the anisotropy of the synthesized MNPs to tune the magnetic hyperthermia properties.(Carrey et al., 2011)

All the described theory models indicate, as expected, a strong dependence of the power from the frequency and amplitude of the applied magnetic field. However, it is known that clinical applications of MFH

cannot be carried out by exceeding a threshold of the product fH_0 that accounts for side effects in the patients as direct consequence of eddy currents in the tissues. This threshold has been found experimentally by Atkinson *et al.* to be equal to $4.85 \cdot 10^8$ A m^{-1} s^{-1} for a loop diameter of 30 cm and one hour of treatment.(Atkinson et al., 1984) Then, Hergt *et al.* proposed to increase this threshold to the value $5 \cdot 10^9$ A m^{-1} s^{-1} taking into account that smaller body regions are expected to be exposed during MFH therapy.(Hergt and Dutz, 2007) Indeed, the heat associated with such eddy currents is proportional to the square of the product fH_0D, where D is the diameter of the induced current loop in the body.(Krishnan, 2010) Thus, this limit value is actually the common considered one in the literature.

2.4.3   Specific Absorption Rate (SAR) or Specific Loss Power (SLP)

A useful tool to estimate the power released by MNPs subjected to an alternate magnetic field is the *specific absorption rate* (SAR) or *specific loss power* (SLP). This quantity represents the power per unit mass, expressed in W/g, and can be obtained by means of the following equation:

$$SAR = SLP = \frac{\sum_i m_i C_i}{m_{MNPs}} \frac{\Delta T}{\Delta t}$$

Eq. 2.4.9

Where m_i and C_i are mass and specific heat of the *i-th* specie composing the sample, m_{MNPs} is the total MNPs mass and ΔT is the temperature increase in the interval Δt during which the AC field is on.(Natividad et al., 2009) Note that this parameter differs from the clinically-adopted SAR that is used to denote the power dissipation per gram of living human tissue, when the transfer of energy into the human body by electromagnetic fields needs to be defined.(Wildeboer et al., 2014)

SAR values are commonly obtained by means of experimental set-up made of an AC magnetic field generator, a sample holder surrounded by an isolating material, temperature probes and a data acquisition system. Under adiabatic conditions, temperature linearly increases with time and the slope of the heating curve directly provides the SAR. On the contrary, common homemade systems work under non-adiabatic conditions and the determination of SAR values is less accurate due to heat transfer with the environment in comparison with an adiabatic system, leading to underestimated values. Indeed, a fitting curve is necessary to determine the SAR value. (Natividad et al., 2008; Wildeboer et al., 2014)

Wildeboer *et al.* in 2014 dealt with the heat losses associated with the use of non-adiabatic systems, suggesting also a standardised procedure to measure and analytically determine SAR values. The heat transfers between the sample and the environment during non-adiabatic measurements involve different mechanisms of heat losses as the conduction, convection or evaporation or melting phenomena and may depend on the different temperature of the sample (T) and the surroundings (T$_0$). Conduction represents the heat transfer from the sample to adjacent materials and depends on the temperature difference T-T$_0$, on the thermal properties and on the surface area. The convection involves the motion or diffusion of a heated medium and takes place in the air surrounding the sample.   In addition, the temperature close to the heat source may reach the boiling or melting point of some components of the system, causing anomalies in the heating curves. Another phenomenon, strongly dependent on the experimental apparatus used to measure the heating curve, is the so-called peripheral

heating that involves the heat release due to the magnetic coil itself and the eddy currents in the fluid (water rather than other solvents or salt solutions).

For an adiabatic system, all the heat released by the heat source contributes to the increase of the temperature in agreement with the equation

$$C \cdot \frac{dT(t)}{dt} = P$$

Eq. 2.4.10

Where C is the capacity of the sample, P is the power.

On the contrary, due to heat losses, in non-adiabatic systems the temperature do not rise linearly with time, as depicted in **Fig. 2.4.1.**
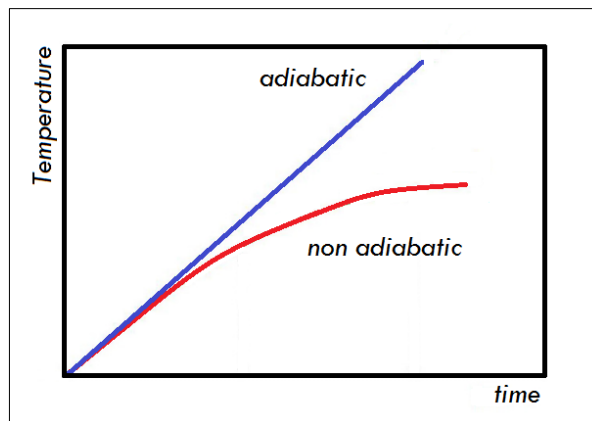
Fig. 2.4.1 Time dependence of temperature for adiabatic and non-adiabatic SAR measuring setups.

For this reason, the heating curve measured by non-adiabatic systems can be described by the following equation instead of Eq. 2.4.10:

$$C \cdot \frac{dT(t)}{dt} = P - P_L(T)$$

Eq. 2.4.11

Where P_L (T) is the power lost by the different heat losses mechanisms and which is dependent on the temperature.

Other basic aspects that has to be taken into account during SAR measurements are related to the presence of spatial or temporal temperature gradients in the sample and time delay in the heating curve between the switching on of the field (t=0) and the effective time at which an increase of the temperature is recorded.(Wildeboer et al., 2014)

The same authors also reviewed the various analytical models used to determine the SAR values: initial slope method, decay method, Box-Lucas method and steady state method. In addition, they proposed a novel method called "corrected slope method"(Wildeboer et al., 2014). Among these models, the most widely used is the initial slope method, although it has been applied with many variants. It is based on a linear curve fitting

in the initial region of the heating curve, when it is supposed to have negligible heat losses. It consider only this region of the curve as approaching the ideal adiabatic conditions.

Due to the difficult comparison of SAR values obtained by different research groups under different experimental conditions (i.e. different values of field frequency and strenght), Pankhurst *et al.* proposed an additional parameter to compare the heating abilities and called it as the Intrinsic Loss Power (ILP)(Kallumadil et al., 2009) expressed in [nH·m2/kg] and defined as follows:

$$ILP = \frac{SAR}{f \cdot H_0{}^2}$$

Eq. 2.4.12

Where SAR is expressed in W/kg, f in kHz and H_0 in kA/m. This formula arises from the observation that SAR increases linearly with the frequency quadratically with the amplitude.(Wildeboer et al., 2014) It is valid under certain conditions as frequency values of up to several MHz, crystallite polydispersity of more than 0.1. Furthermore, a comparison among ILP values is possible only if similar environmental thermodynamic losses are involved.(Kallumadil et al., 2009)

2.4.4   State of the art

For MFH *in vivo* applications, the concentration of the exogenous material in the tissue should be minimised to avoid unwanted side effects. For instance, a maximum recommended value of 0.1 mmol/kg has been suggested for MRI contrast agents.(Laniado and Chachuat, 1995; Zeisberger et al., 2007) In this framework, much effort has been spending in this research field to optimise the hyperthermal efficiency by proposing different systems: from the single colloidal nanoparticles to magnetosomes, aggregates and exchange-coupled core@shell structures. Superparamagnetic nanoparticles (usually referred as SPIOs, i.e. superparamagnetic iron oxides) of magnetite, Fe_3O_4, and/or maghemite, γ-Fe_2O_3, are the most studied systems in particular due to their biocompatibility (safety, well-known metabolic pathway in the human body) and their successful clinical use as MRI contrast agents.(Blanco-Andujar et al., 2015) In 1993, Jordan *et al.* compared the heating abilities of multi-domain and single-domain (1-10 nm) nanoparticles of magnetite and other ferrites, both bare and dextran coated, in different media (agar-embedded, water, glycerol) and field amplitudes and frequencies. By this study, they were able to establish the suitability of magnetic nanoparticles as hyperthermia mediators and the superiority of single domain nanoparticles in comparison with multi-domain ones.(Jordan et al., 1993) Some of the works published on SPIOs nanoparticles as single nanoparticles are reported in **Tab. 2.4.1**. This table clearly shows all the problems related to the comparison of literature data. First, a variety of field amplitudes and frequencies have been used to date, either above or below the threshold fH_0 product accounting for human tolerability (see paragraph 2.4.2). Secondly, sometimes the proposed materials are poorly characterised or with a broad size distribution (>20 %) or, moreover, they are sometimes highly agglomerated. This means that SAR values cannot be discussed easily in terms of material's features and the behaviour can be rarely attributed univocally to a specific effect. In the case of SPIOs, also some papers refer generically to spinel-structured nanoparticles as "iron oxides" nanoparticles without any assignments of the crystalline phase as *magnetite* rather than *maghemite*. Please, also note that the ILP parameter can be used only in the validity field of the linear

response theory but most of the promising systems do not show actually linear-frequency and square-amplitude dependences so that the ILP cannot help us in the comparison (see paragraph 2.4.3). Despite all this limits, among the proposed SPIOs systems, recently very high SAR values have been achieved for single water-soluble nanocubes of sizes around 20 nm or more(Guardia et al., 2014, 2012). These systems are responsible for a heat release mainly by hysteretic losses in agreement with other promising results obtained for magnetosomes(Alphandéry et al., 2011a, 2011b; Hergt et al., 2005) or nanoflowers(Hugounenq et al., 2012) or other multi-core aggregates(Blanco-Andujar et al., 2015) (**Tab. 2.4.2**). Therefore, it is worth noting that part of the researchers are moving from superparamagnetic systems with sizes below 15-20 nm for magnetite/maghemite nanoparticles towards systems with sizes higher or in the limit between superparamagnetic and blocked-single domain in order to achieve better performances with SPIOs. However, as the magnetic interactions increase with increasing particle volume, these systems in principle may suffer of some biological constraints arising from possible agglomeration phenomena that in the human body may translate into blood vessels obstruction or low circulation times. With this respect, Guardia *et al.* have also developed a strategy to coat by a polymer each nanocube producing single water-soluble particle to prevent possible agglomeration phenomena.(Guardia et al., 2014) Spinel ferrites with M^{II} alternative to Fe^{II} have been less studied (**Tab. 2.4.3**). Fantechi *et al.* have investigated the substitution of Fe^{II} by Co^{II} in the magnetite structure of 8.5 nm particles, showing an increase of the SAR with increasing Co^{II} content up to 0.6 per formula unit.(Fantechi et al., 2015) Both manganese and cobalt ferrite nanoparticles have been also investigated even though with a lower extent. However, the efficiency of these systems is still lower than the SPIOs one. Moreover, the heat delivery of metallic nanoparticles have been characterised, both as bare particles(Lacroix et al., 2011, 2009; Mehdaoui et al., 2011, 2010; Zeisberger et al., 2007) and as core@shell systems aimed to overcome the limit of their poor chemical stability.(Balivada et al., 2010; Ibrahim et al., 2012; Kline et al., 2009; Lacroix et al., 2009; Wang et al., 2012; Zeng et al., 2007)

Finally, other platforms for MFH have been proposed from cobalt and zinc-doped magnetosomes(Alphandéry et al., 2011; Céspedes et al., 2014) to exchange-coupled bimagnetic core@shell nanostructures(Lee et al., 2011; Noh et al., 2012). This latter strategy has been demonstrated to be powerful being responsible for SAR values ranging from 1000 to 4000 W/g (f=500 kHz, H_0=37.3 kA/m) for 15 nm core@shell nanoparticles, that are one order of magnitude higher than their single-component counterparts.(Lee et al., 2011) In a later study, the same authors have also tuned the properties of these bimagnetic nanostructures by increasing the size and changing the shape and they finally reached a SAR of 10600 W/g for a 60 nm core@shell nanocubes.

From this discussion, it appears clear that the best results to date in terms of highest SAR values have been achieved for systems with a dominant contribute of hysteretic losses. However, it should be underlined that smaller nanoparticles especially in the superparamagnetic regime offer a better control of their magnetic behaviour due to almost negligible interparticle interactions that make the systems more appealing for biomedical application, hindering possible undesired agglomeration or precipitation phenomena. All limits evidenced in this paragraph justify the great efforts and number of publications published per year in this research field, aimed to design and synthesise alternative magnetic heat nanomediators with improved magnetic and hyperthermal properties.

Tab. 2.4.1 Superparamagnetic nanoparticles (SPIOs, i.e. superparamagnetic iron oxides) of magnetite, Fe_3O_4, and/or maghemite, γ-Fe_2O_3 proposed in the literature as heat mediators for Magnetic Fluid Hyperthermia.

Reference	System	Shape	D (nm)	Solvent	f (kHz)	H₀ (kA/m)	SAR (W/g)	ILP
(Hilger et al., 2001)	Fe_3O_4	Spherical	10	Human breast tissue	300	14	211	3.6
(Fortin et al., 2007)	Citrate-γ-Fe_2O_3	Cubic (?)	16.5 (D_{TEM})	Water	700	24.8	1650	3.8
(Pradhan et al., 2007)	Lauric acid-Fe_3O_4	Spherical	10 (D_{TEM})	Water	300	15	120	1.8
(Zhang et al., 2007)	Dextran-Fe_3O_4	-	19 (D_{XRD})	Water-glycerol	55	15.9	75	5.4
(Gonzales-Weimuller et al., 2009)	Pluronic F127-Fe_3O_4	Spherical	14 (D_{TEM})	Phosphate buffer solution	400	24.5	447	1.9
(Purushotham et al., 2009)	Polymer- γ and α Fe_2O_3	Irregular	43	Water	375	1.7	42.8	-
(Suto et al., 2009)	Surfactant-Fe_3O_4	-	14.6 (D_{TEM})	Water	600	3.2	28.3	4.6
(Kikuchi et al., 2011)	Polymer-Fe_3O_4	Spherical or polyhedral	12.5	Water	600	3.2	22.5	3.7
(Lartigue et al., 2011)	Rhamnose-iron oxides	Spherical	16.2 (D_{TEM})	Water	168	21	185	1.2
(Lee et al., 2011)	Oleic acid-Fe_3O_4	Spherical	12 (D_{TEM})	Toluene	500	37.3	349	0.5
(de la Presa et al., 2012)	APS-γ-Fe_2O_3	Spherical	12.7 (D_{TEM})	Water	522.3	7.5	56	1.9
(Guardia et al., 2012)	Polymer-iron oxides	Cubic	19 (D_{TEM})	Water	320	15	509	**7.0**
(Liu et al., 2012)	mPEG-Fe_3O_4	Spherical	19 (D_{TEM})	Water	400	27	930	3.2
(Song et al., 2012)	DMSA-Fe_3O_4	Quasi cubical	9.5 (D_{TEM})	Water	100	30	35.1	0.4
(Jadhav et al., 2013)	Oleic acid-Fe_3O_4	-	7 (D_{TEM})	0.1M sodium carbonate	265	26	45	0.2
(Guardia et al., 2014)	PEG-iron oxides	Cubic	35	Water	320	24	1391	**7.6**
(Shete et al., 2014)	Chitosan-Fe_3O_4	Spheroidal (?)	15.1	Water	265	26.7	118.85	0.6
(Lv et al., 2015)	CTAB intercalated oleate-Fe_3O_4	Octahedral	43-98	Agarose	358	63	2483-2629	-
(Sasikala et al., 2015)	HEDO-Fe_3O_4	Spherical	<15	Water	293	12.57	181.31	3.9

Tab. 2.4.2 Examples of different systems proposed in the literature as heat mediators for Magnetic Fluid Hyperthermia made up of chains of single nanoparticles (magnetosomes) or aggregates or exchange-coupled core@shell systems.

Reference	Shape	f (kHz)	H0 (kA/m)	SAR (W/g)
(Hergt et al., 2005)	Magnetosomes	410	10	960
(Lee et al., 2011)	Exchange-coupled spinel ferrite bimagnetic core@shell	500	37.3	3886
(Noh et al., 2012)	Exchange-coupled spinel ferrite bimagnetic core@shell	500	37.3	10600
(Alphandéry et al., 2011a)	Magnetosomes	108	70	864
(Alphandéry et al., 2011b)	Magnetosomes	183	31.8	380
(Hugounenq et al., 2012)	Nanoflowers	700	21.5	1992
(Blanco-Andujar et al., 2015)	Multi-core	950	10.5	430

Tab. 2.4.3 Single nanoparticles of cobalt ferrite or cobalt-doped iron oxides proposed in the literature as heat mediators for Magnetic Fluid Hyperthermia.

Reference	System	Shape	D (nm)	Solvent	f (kHz)	H0 (kA/m)	SAR (W/g)	ILP
(Pradhan et al., 2007)	Lauric acid-$MnFe_2O_4$	Spherical	10 (D_{TEM})	Water	300	15	145	2.2
(Lee et al., 2011)	$MnFe_2O_4$	Spherical	15 (D_{TEM})	Toluene	500	37.3	411	0.59
(Fortin et al., 2007)	Citrate-$CoFe_2O_4$	Spherical	9.7 (D_{TEM})	Water-glycerol	700	24.8	420	0.98
(Pradhan et al., 2007)	Lauric acid-$CoFe_2O_4$	Spherical	10 (D_{TEM})	Water	300	15	37	0.55
(Kim et al., 2008)	11-MUA-$CoFe_2O_4$	Spherical	5.6 (D_{TEM})	Water	266	30	-	-
(Joshi et al., 2009)	$CoFe_2O_4$	Spherical	15	Water	300	-	396.1	-
(Franchini et al., 2010)	BSA-$CoFe_2O_4$	Spherical	6.7 (D_{TEM})	Water	168	21	215	2.9
(Kita et al., 2010)	Silica coated Co-doped Fe_3O_4	Spherical	13 (D_{XRD})	Water	117	51	217	0.71
(Lee et al., 2011)	$CoFe_2O_4$	Spherical	9	Toluene	500	37.3	443	0.64
(Mazario et al., 2013)	Citrate-$CoFe_2O_4$	-	28	Water	101	40	133	0.82
(Fantechi et al., 2015)	$Co_{0.6}Fe_{2.4}O_4$	Spherical	8.4 (D_{TEM})	Toluene	183	12	40.4	1.5
(Nappini et al., 2015)	Citrate-$CoFe_2O_4$	Spherical	12	Water	183	17	105	1.99
(Nikam et al., 2014)	PEG-$Co_{0.5}Zn_{0.5}Fe_{2.4}O_4$	Spherical	10 (D_{TEM})	Phosphate buffer solution	267	27	193	0.99
(Bohara et al., 2015)	TEG-$Co_x Zn_{1-x}Fe_{2.4}O_4$	Spherical	15 (D_{TEM})	Water	267	27	132	0.68

3 Cubic ferrites nanoparticles

Abstract

Ferrimagnetism is a kind of magnetic order due to an antiparallel alignment of magnetic moments of different intensities (Coey, 2010). Iron oxides of general formula $M^{II}Fe_2O_4$ (M^{II}=Fe^{2+}, Co^{2+}, Mn^{2+}, Ni^{2+}, etc.), commonly referred as *cubic ferrites*, are the most important ferrimagnetic materials.(Cullity and Graham, 2009) They are ionic compounds arranged as in the spinel structure AB_2O_4 (Cullity and Graham, 2009). The chemical composition and the cationic distribution strongly affect the magnetism of such compounds.

In this chapter, the structural and magnetic properties of this class of materials are briefly discussed.

3.1   Introduction

Iron oxides of general formula $M^{II}Fe_2O_4$ (M^{II}=Fe^{2+}, Co^{2+}, Mn^{2+}, Ni^{2+}, etc.), commonly referred as *ferrites*, are the most important ferrimagnetic materials.(Cullity and Graham, 2009)

The term "*ferrites*" refers to all oxides with formula $M^{II}Fe_2O_4$ containing iron as major metallic component. In these compounds, the symbol *M* represents ions with ionic radius ranging between 0.6 and 1 Å. M^{II} can be a transition element as Mn, Fe, Co, Ni, Cu and Zn or Mg or Cd or, moreover, it can be a combination of different elements. In this latter case, we can consider the oxide as a "*mixed ferrite*", made of a solid solution of two ferrites. In addition, M can be also made of cations with an average valence of two, as in the lithium ferrite ($Li_{0.5}Fe_{2.5}O_4$) or can be a combination of vacant lattice sites and trivalent ions as in the maghemite structure, γ-Fe_2O_3, of formula $\square_{1/3}Fe_{8/3}O_4$. The trivalent iron cations can be replaced too by other ions, as Al^{III} or Cr^{III}, but in this case the solid solution is between ferrites and aluminates or chromites, respectively.(Smit and Wijn, 1959)

This class of materials has many application fields from magnetic storage media to energy, environmental issues and biomedicine, in particular when they are nanostructured, becoming responsible for particular phenomena as the superparamagnetism (see paragraph **1.2**). Their magnetic properties are strongly correlated to their structure as described in the following paragraphs.

3.2   Crystalline structure of spinel ferrites $M^{II}Fe^{III}_2O_4$

Magnetic ferrites crystallise mainly into two different crystalline structures:

1. *Cubic*. These have general formula $M^{II}Fe_2O_4$, where M^{II} is a divalent metal ion, like Fe^{II}, Mn^{II}, Ni^{II}, Co^{II}, or Mg^{II}.

2. *Hexagonal*. Also known as *hexaferrites*, the most important members of this group are barium and strontium ferrites, $BaO \cdot 6Fe_2O_3$ and $SrO \cdot 6Fe_2O_3$.(Cullity and Graham, 2009)

In this paragraph, only the crystalline structure of cubic ferrites that are of close interest in this thesis is described.

Cubic ferrites crystallise in the structure of the mineral $MgAl_2O_4$, called "*spinel*". The elementary cell with cubic symmetry of the spinel lattice contains eight formula units of $M^{II}Fe_2O_4$. The oxygen ions are close-packed in a face centred cubic structure (*fcc*), whereas metallic ions are accommodated within two types of interstitial sites, associated with two different coordination of metallic ions to oxygens: tetrahedral, referred as T_d sites, and octahedral, referred as O_h sites (**Fig. 3.2.1, Fig. 3.2.2**).(Smit and Wijn, 1959) Within the unit cell, 64 sites of 4-fold coordination and 32 sites of 6-fold coordination are available. However, only 8 tetrahedral and 16 octahedral sites are occupied by metallic cations.

Divalent cations in the zinc and cadmium ferrites occupy exclusively T_d sites. This is referred as a *direct spinel* and is described by the formula $\{[M^{II}]^{Td}[M^{III}]^{Oh}_2O_4\}$. On the other hand, other ferrites as magnetite (Fe_3O_4), maghemite (γ-Fe_2O_3), cobalt and nickel ferrites show an *inverse spinel* structure. In that case, tetrahedral sites are occupied by trivalent ions but both trivalent and divalent ions are accommodated in octahedral sites. The general formula of this type of structure is $\{[M^{III}]^{Td}[M^{II}, M^{III}]^{Oh}O_4\}$ (Cullity and Graham, 2009). In other words, if M^{II} ions occupy tetrahedral sites, the spinel is direct; if they occupy octahedral sites, the spinel is inverse (**Fig. 3.2.3**).(Hochepied et al., 2000)

Actually, several *partially inverse* structures do exist in agreement with the following general formula:

$$M^{II}_{\delta}Fe^{III}_{1-\delta}\left[M^{II}_{1-\delta}Fe^{III}_{1+\delta}\right]O_4$$

Eq. 3.2.1
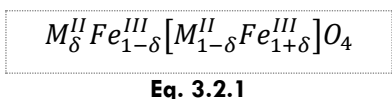
Where δ is a parameter related to the inversion degree ($i = 1 - \delta$) and it is equal to 1 for a normal spinel and 0 for an inverse one.

Tab. 3.2.1 lists the crystallographic data for some cubic ferrites.
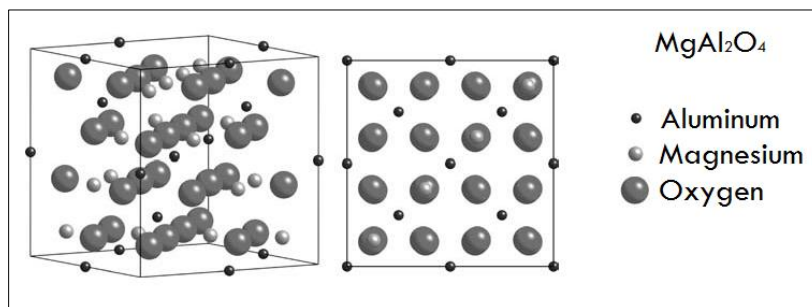
Fig. 3.2.1 Direct spinel structure.
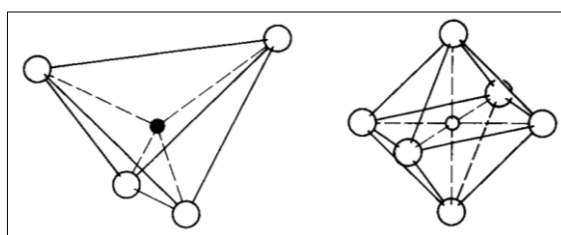
Fig. 3.2.2 Tetrahedral and octahedral sites in a spinel structure.
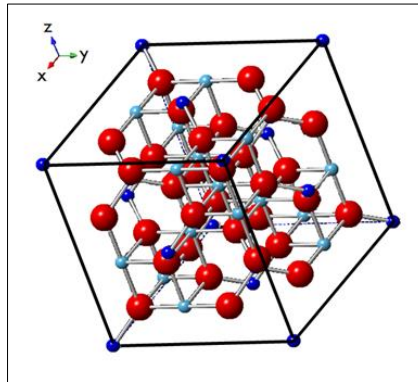
Fig. 3.2.3 Inverse spinel structure. Red spheres: oxygens, Dark blue spheres: tetrahedral sites, Light blue spheres: octahedral sites.

Tab. 3.2.1 Crystallographic data for some cubic ferrites (Murad and Johnston, 1985).

Formula	Mineral	Crystal system	Structure type	Unit cell dimensions (nm)
Fe_3O_4	magnetite	cubic	inverse spinel	a = 0.83960[a]
γ-Fe_2O_3	maghemite	cubic or tetragonal	defect spinel	a = 0.834 a = 0.8338; c = 2.501
$CoFe_2O_4$	cobalt ferrite	cubic	inverse spinel	a = 0.83919[b]
$MnFe_2O_4$	manganese ferrite	cubic	inverse spinel	-
$ZnFe_2O_4$	zinc ferrite	cubic	direct spinel	a = 0.84411[c]
[a] PDF card #: 19-0629; [b] PDF card #: 22-1086; [c] PDF card #: 22-1012				

3.3 Magnetic properties of bulk and nanostructured spinel ferrites ($M^{II}Fe^{III}_2O_4$)

The interest on cubic ferrites is well justified by their ferrimagnetism, an imperfect antiferromagnetic order with a spontaneous magnetisation below a certain temperature called Curie temperature (T_c).(Coey, 2010; Cullity and Graham, 2009)

According to Néel model, a ferrimagnetic cubic ferrite is made up by two independent magnetic sublattices corresponding to the interstitial sites of the crystalline structure, T_d and O_h. Because the magnetisation associated with the two sublattices are of different intensity, a net magnetisation exists giving rise to a ferrimagnetic order.

The magnetism of this class of materials arises not just from their crystalline structure but also from the nature of the cations. Indeed, spinel ferrites are ionic compounds where the metal cations (at least the Fe^{III}) are responsible for a magnetic moment. Indeed, a magnetic moment is associated with the motion of electrons, both orbital and spin. An atom has a total magnetic moment that is the sum of all the electronic moments but only semi-filled shells contributes to it. Completely filled shells have a zero magnetic moment because only pairs of electrons are present due to the Pauli exclusion principle. Therefore, Fe^{3+} and Fe^{2+} with five and four unpaired electrons in the 3d level, respectively, have magnetic moment of 5 and 4 μ_B (**Fig. 3.3.1**).
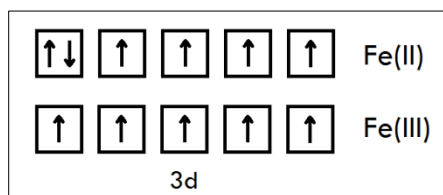
Fig. 3.3.1 Electronic configuration of Fe^{2+} and Fe^{3+}.

The nature of the divalent ion strongly affects the magnetic order and the magnetic properties of the cubic ferrite. Among spinel ferrites, $CoFe_2O_4$ is the only magnetically hard with a high magnetocrystalline anisotropy, high coercivity due to the presence of the Co^{II}, reasonable magnetisation, excellent chemical and thermal stabilities and good mechanical properties.(Cullity and Graham, 2009) It can be also easily prepared.(Cannas et al., 2015, 2010a, 2008, 2006, 2004)

Different strategies have been proposed in the literature for the tuning of the magnetic properties of cubic ferrites NPs.
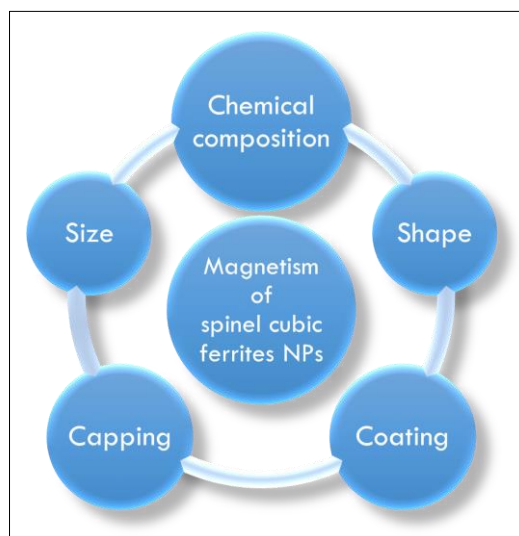
Fig. 3.3.2 General strategies for the tuning of cubic ferrites' magnetic properties.

For instance, different authors have studied the variations of the magnetic properties of ferrite NPs systems as a function of their size (Baldi et al., 2007; Jia et al., 2008; Joshi et al., 2009; López-Ortega et al., 2015b; Mohapatra et al., 2013; Roca et al., 2006, 2007; Song and Zhang, 2004), their shape (Bao et al., 2009; Joshi et al., 2009; López-Ortega et al., 2015b; Song and Zhang, 2004; Zhen et al., 2011) or the effect of different capping agent (Daou et al., 2008; Mohapatra et al., 2013; Vestal and Zhang, 2003).

The chemical composition itself affects the magnetic properties of the cubic ferrite.(Fantechi et al., 2012; Hu et al., 2012; Jia et al., 2008; Liu et al., 2000; Mohapatra et al., 2013; Muscas et al., 2015)

Finally, the cationic distribution and, consequently, the inversion degree of the spinel structure, is another key feature for modulating the magnetic behaviour due to the strict relation existing between the spinel structure

and the magnetism, as mentioned before.(Mohapatra et al., 2013; Peddis et al., 2011; Sharifi and Shokrollahi, 2012; Zi et al., 2009)

It is worth to mention that other phenomena, such as internal or surface disorder (i.e. spin canting) may also affect the magnetic properties of NPs systems.

Although many articles have been published so far in the field, due to the intrinsic inter-correlations of all these features (chemical composition, size, shape, surface ligands, etc.), often a single parameter cannot be tuned independently from the others, i. e. keeping unchanged the others, making the effect on the magnetic properties rarely ascribable to a unique parameter.

4   Zn-substituted cobalt ferrite nanoparticles ($Zn_xCo_{1-x}Fe_2O_4$): study of the magnetic properties and heating abilities beyond the particle and crystal size

Abstract

The possibility of finely tuning the magnetic properties opens to design suitable nanostructured spinel ferrites ($M^{II}Fe_2O_4$) for specific applications. However, the strict and complex interrelation among the chemical composition, size, polydispersity, shape and coating renders difficult the prediction of their effect on the magnetic properties. In this context, this chapter works toward the discussion of the magnetic properties and the heating abilities of Zn-substituted $CoFe_2O_4$ nanoparticles with different zinc content ($Zn_xCo_{1-x}Fe_2O_4$ with $0<x<0.6$), specifically synthesised with similar crystallite diameter (~6 nm), particle diameter (~7 nm), polydispersity and capping agent amount (15%).

All samples show high saturation magnetisation values at low temperature (> 100 emu/g). The insertion in the structure of zinc up to a content x of 0.46 per formula unit has resulted in an increase of the saturation magnetisation (M_s) at 5 K. On the other hand, both coercive field (H_c) and saturation field (H_{sat}) have similar values when $x > 0$, suggesting similar magnetic anisotropy for the zinc-substituted samples. The 5 K magnetic properties are discussed in the light of their cationic distribution.

Both $CoFe_2O_4$ and $Zn_{0.30}Co_{0.70}Fe_2O_4$ samples exhibit also high and similar saturation magnetisation values at 300 K (90 emu/g). Being the magnetic properties of the samples appealing for Magnetic Fluid Hyperthermia, their heating ability has been tested. Despite the similarities among the two samples, cobalt ferrite is responsible for a Specific Absorption Rate (SAR) value three times higher than the Zn-substituted one. DC magnetometry appears not sufficient to justify these data, being the experimental conditions of SAR and static measurements rather different. On the contrary, the synergic combination of DC magnetometry with AC magnetometry and [57]Fe Mossbauer spectroscopy represents a powerful tool to understand the observed heating abilities and in prospect to get new insights for the design of suitable heat mediators.
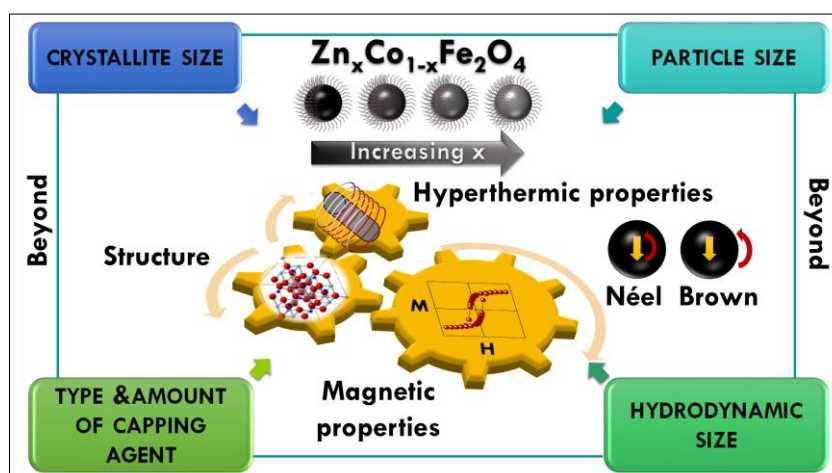
4.1   Introduction

The efficiency of MNPs as heat mediators is strictly related to their magnetic properties (saturation magnetisation, magnetic anisotropy and magnetic interactions). The most studied materials for MFH are SuperParamagnetic Iron Oxides (SPIOs), i.e. maghemite (γ-Fe$_2$O$_3$) and magnetite (Fe$_3$O$_4$), due to their biocompatibility (U.S. Food and Drug Administration approved(Krishnan, 2010)) and their low-cost.(Hervault and Thanh, 2014) However, researchers are still working on to reduce the NPs dose to be inserted in the human body by optimising their magnetic properties. Co-containing materials have been proposed as promising heat mediators due to its high anisotropy although their potential toxicity.(Alphandéry et al., 2011; Baaziz et al., 2014; Deatsch and Evans, 2014; Fantechi et al., 2015; Joshi et al., 2009; Kim et al., 2008; Kita et al., 2010; Mazarío et al., 2012; Nappini et al., 2015; Pichon et al., 2011; Thanh et al., 2015; Torres et al., 2010; Veverka et al., 2010) The partial substitution of Co^{2+} with less toxic divalent ions as Zn^{2+} (Zn$_x$Co$_{1-x}$Fe$_2$O$_4$) has been also proposed in order to increase the saturation magnetisation, to lower the toxicity(Bohara et al., 2015; Nikam et al., 2014) and the Curie temperature for auto-tuning systems.(Arulmurugan et al., 2006; Jadhav et al., 2010; Nikam et al., 2014; Sharifi and Shokrollahi, 2012; Veverka et al., 2010) Among the several studies on the Zn-substituted cobalt ferrites NPs only a few are devoted to the discussion of their heating ability.(Bohara et al., 2015; Nikam et al., 2014) In these works, Pawar *et al*. have studied the long-term colloidal stability in different media only for the composition Co$_{0.5}$Zn$_{0.5}$Fe$_2$O$_4$ NPs and stated that they can be considered as potential candidate for effective MFH treatment for cancer cell extinction. To the best of our knowledge, a systematic and fundamental study of the effect on the magnetic properties and heat release based only on the composition for Zn$_x$Co$_{1-x}$Fe$_2$O$_4$ NPs is still lacking. Indeed, the strict and complex interdependence among their chemical composition, size, polydispersity, shape, surface coating and interactions makes their correlation with the magnetic properties not trivial.

In this chapter, being the nature of divalent ions together with the cationic distribution in the ferrite structure crucial for tuning the magnetic properties, the substitution of cobalt ions by means of diamagnetic zinc ones in cobalt ferrite NPs (Zn$_x$Co$_{1-x}$Fe$_2$O$_4$) is explored as possible route to increase the saturation magnetisation and consequently to increase the efficiency as heat mediators. *Ad-hoc* Zn-substituted cobalt ferrites NPs with different zinc content but with the same crystallite and particle sizes, polydispersity, type and amount of capping agent, have been selected to systematically study their magnetic properties and heating ability exclusively on the basis of their different chemical composition and magnetic structure (i.e., cationic distribution and spin canting).

4.2   Synthesis

Four samples of $Zn_xCo_{1-x}Fe_2O_4$ nanoparticles with $0 \leq x \geq 0.53$ were synthesised[1] by the heating-up surfactants-assisted thermal decomposition method previously described by Sun *et al.*(Sun et al., 2004) This method has been widely used, among other chemical methods, because it allows to synthesise uniform nanocrystals of ferrites NPs with well-controlled features as crystalline phase and crystallinity, shape, size and polydispersity. This fine control of the microstructural and morphological properties can be reached by properly choosing the organometallic precursors, the surfactants, the high-boiling solvent and their relative amounts. In addition, fundamental parameters are also the reaction temperature, pressure and time. A critical drawback is the production of hydrophobic NPs that should be then properly post-synthesis functionalized (e.g. by exchange-ligand or intercalation processes) to make them hydrophilic. The formation process of the NPs occurs by four steps:

1. Thermal decomposition of the organometallic precursors;
2. Formation of monomers complexes made by clusters of the atomic or molecular species formed during the decomposition reaction surfactants molecules;
3. Self-assembly of monomers forming small nanocrystals (*nucleation*);
4. The surfactants molecules continuously adsorb and desorb from the nuclei surface in agreement with the relative bond strenght, allowing other monomers to come into contact with it and react and making the nanoparticle to grow (*growth*). Another important phenomen that may occur is the Ostwald ripening, i.e. the dissolution of smaller NPs that produces monomers growing bigger NPs.

La Mer and Dinegar, in their study dated back to the 1950, indicated that a single and rapid nucleation event and a slow growth are necessary conditions to produce monodisperse NPs with well-controlled properties based on the time dependence of the monomers concentration.(LaMer and Dinegar, 1950) This situation can be achieved by a rapid hot-injection of the organometallic precursors in the reaction mixture (solvent+surfactants) or by separating the nucleation and the growth steps through two thermal treatments.

In this work, $Fe^{III}(acac)_3$, $Co^{II}(acac)_2$, $Zn^{II}(acac)_2$, 1,2-hexadecanediol (10 mmol), oleic acid (6 mmol), oleylamine (6 mmol), dibenzylether (20 ml) were added in a 250 ml three-necks round bottom flask. The system was heated up to 200 °C for 2 h and to 280 °C for 1 h, under magnetic stirring and a blanket of nitrogen.

Particular attention was paid on the control of the temperature during the synthesis (**Fig. 4.2.1**) and, in order to render it repeatable, an auto-tuning Proportional-Integral-Derivative (PID) controller was used (**Fig. 4.2.2**).

---

[1] The candidate Valentina Mameli synthesised and partially characterised the samples during her research activity under the supervision of Prof. Nguyen T. K. Thanh at the UCL Healthcare Biomagneticnd Nanomaterials Laboratories located at the Royal Institution of Great Britain (London). The characterisation was then completed at the University of Cagliari.
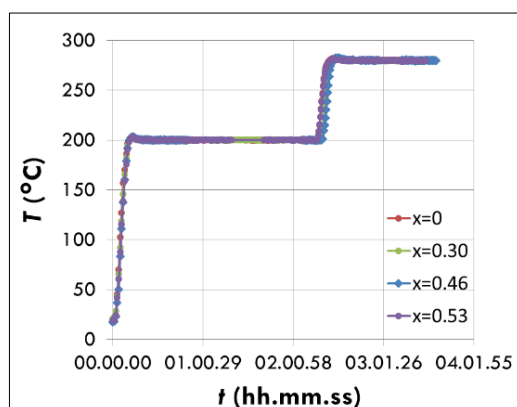
Fig. 4.2.1 Time profile of the temperature measured inside the flask during the syntheses of the ZnxCo1-xFe2O4 samples. x is the actual zinc content determined by ICP-AES (see 4.3).

Fig. 4.2.2 Heating mantle, magnetic stirrer and Proportional-Integral-Derivative (PID) temperature controller used during the synthesis of $Zn_xCo_{1-x}Fe_2O_4$ nanoparticles.

After the two heating steps, the system was left to cool down to room temperature. Then, 40 ml of absolute ethanol were added to precipitate the nanoparticles from the supernatant overnight. The supernatant was discarded after a centrifugation at 4500 rpm (for 15 min). The as-obtained nanoparticles were washed with ethanol and collected by centrifugation at 4500 rpm (for 15 min). This washing process was repeated six times and, then, the nanoparticles were dispersed in hexane.

Given the critical importance of the composition, structure and morphology (e.g., crystallite size, particles size, particle size distribution, type and amount of coating) on the magnetic and hyperthermic properties of the nanoparticles, an accurate characterisation is often required to understand them. Although there are no generally applicable methods to determine these features of the nanoparticles, a combination of traditional characterisation approaches such as elemental analysis by ICP, ThermoGravimetric Analysis (TGA), Infrared Spectroscopy (FT-IR), X-ray Diffraction (XRD), Conventional and High Resolution Transmission Electron Microscopy (TEM, HR-TEM), [57]Fe Mössbauer Spectroscopy with other sophisticated techniques are often needed

to fully elucidate the composition, the morphology and the structure of these systems. For this reason, particular attention has been paid on their characterisation by repeating the measurements twice or by using different instruments when possible.

4.3 Chemical composition

The samples chemical composition was studied by means of Inductively Coupled Plasma – Atomic Emission Spectrometry (ICP-AES). The samples were analysed two times on different portions and the chemical formulas were calculated by assuming the absence of anions vacancies (**Tab. 4.3.1**). Hereafter, the samples are labelled as CoFe_Znx where *x* is the actual Zn content equal to 0, 0.30, 0.46, 0.53. Moreover, each sample is identified by a different colour: red (CoFe_Zn0), green (CoFe_Zn0.30), blue (CoFe_Zn0.46) and purple (CoFe_Zn0.53).

Tab. 4.3.1 Chemical composition obtained by ICP-AES of the CoFe_Znx (with x=0, 0.30, 0.46, 0.53) samples.

Sample	Chemical formula
CoFe_Zn0	$Co_{0.94}Fe_{2.04}O_4$
CoFe_Zn0.30	$Zn_{0.30}Co_{0.70}Fe_{2.00}O_4$
CoFe_Zn0.46	$Zn_{0.46}Co_{0.54}Fe_{2.02}O_4$
CoFe_Zn0.53	$Zn_{0.53}Co_{0.47}Fe_{2.02}O_4$

4.4 Microstructure and Morphology

4.4.1 X-Ray Diffraction (XRD)

The four samples of $Zn_xCo_{1-x}Fe_2O_4$ NPs were analysed by XRD by using two different diffractometers located in the laboratories of the University of Cagliari (*copper* X-ray source, λ (Kα) = 1.54056 Å) and the University College London (*cobalt* X-ray source, λ (Kα) = 1.78901 Å). The patterns, shown in **Fig. 4.4.1**, indicate the presence of a unique spinel cubic phase ($CoFe_2O_4$, PDF card # 221086) for all the samples with a mean crystallite size of 6.2±0.4 nm obtained by the *copper* X-ray source equipped-diffractometer and 6.1±0.4 nm by the *cobalt* one (**Tab. 4.4.1**).
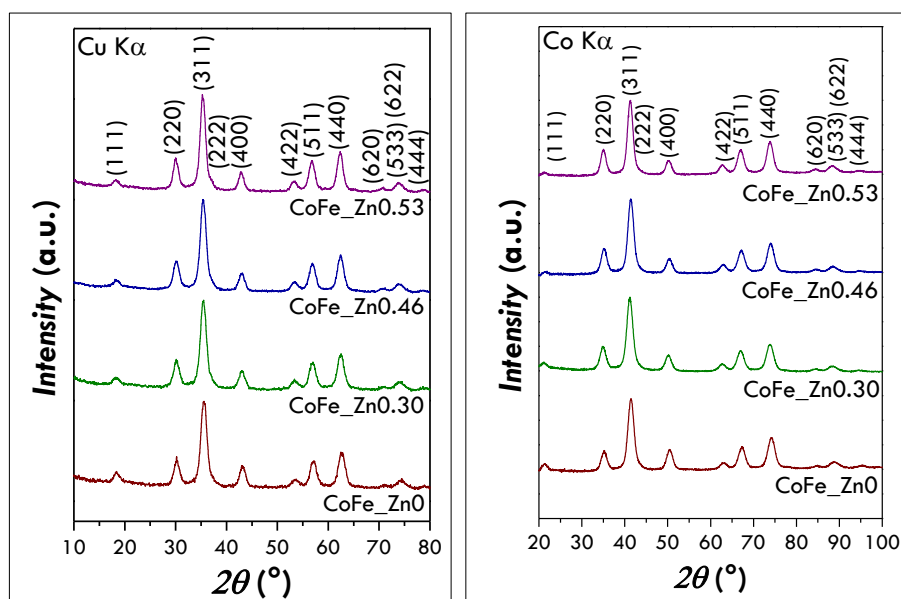
Fig. 4.4.1 XRD patterns of the CoFe_Znx (with x=0, 0.30, 0.46, 0.53) samples recorded by powder X-ray diffractometers equipped with Cu X-ray source (*left panel*) and a Co X-ray source (*right panel*).

Tab. 4.4.1 Crystallite size (diameters) of the CoFe_Znx (with x=0, 0.30, 0.46, 0.53) samples estimated by Scherrer's equation on the patterns recorded by powder X-ray diffractometers equipped with Cu X-ray source (University of Cagliari, *left panel*) and a Co X-ray source (University College London, *right panel*).

Sample	$<D_{XRD}>$ (nm) Cu Kα	$<D_{XRD}>$ (nm) Co Kα
CoFe_Zn0	6.1±0.3	6.0±0.1
CoFe_Zn0.30	5.9±0.2	5.8±0.1
CoFe_Zn0.46	6.0±0.3	6.0±0.2
CoFe_Zn0.53	6.7±0.4	6.6±0.2

Other information can be deduced by XRD.

For instance, the intensity of some reflections are considered to be sensitive to the cations occupancies of the tetrahedral sites(Ladgaonkar and Vaingankar, 1998; Varshney et al., 2011; Wolska et al., 1992) In our case, the intensity ratio between the (220) and the (400) reflections (**Fig. 4.4.2**) is found to linearly increases with increasing zinc content suggesting that probably the zinc ions substitute cobalt ones by occupying preferentially tetrahedral sites.
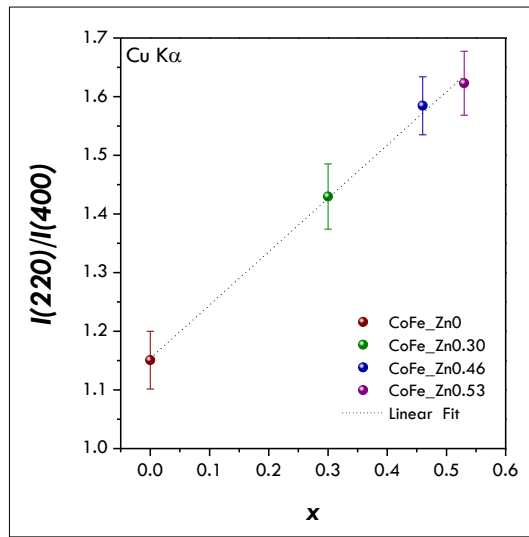
Fig. 4.4.2 Intensity ratio of the (220) and (400) XRD reflections for the CoFe_Znx (with x=0, 0.30, 0.46, 0.53) samples with the corresponding linear curve fitting (($y = 1.15 + 0.91x$; R^2=0.99637).

The XRD patterns were analysed by the Rietveld method. The as-obtained lattice parameters are listed in **Tab. 4.4.2**. Powder X-Ray Diffraction patterns of CoFe_Znx (with x=0, 0.30, 0.46, 0.53) samples (coloured spheres) and related curve fitting by Rietveld Refinement (**Fig. 4.4.3**).
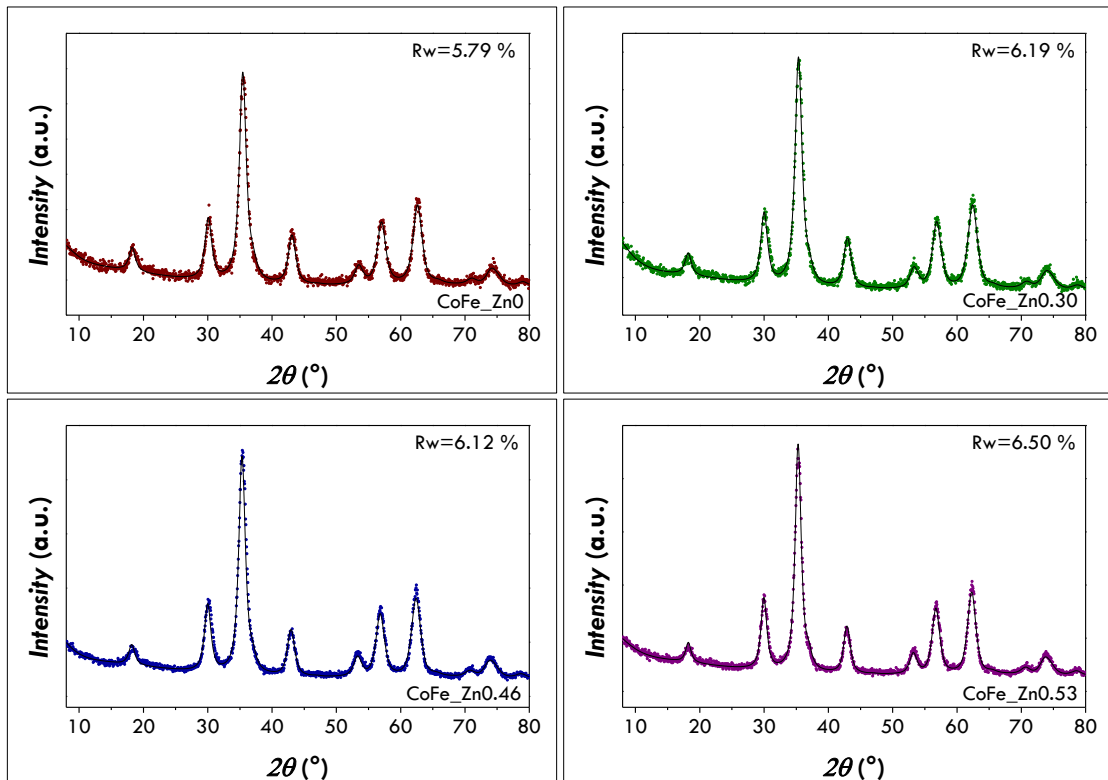
Fig. 4.4.3 Powder X-Ray Diffraction patterns of CoFe_Znx (with x=0, 0.30, 0.46, 0.53) samples (*coloured spheres*) and related curve fitting by Rietveld Refinement (*black curve*).

Tab. 4.4.2 Lattice parameter and cationic distributions obtained by Rietveld analysis (performed on the *Cu*-XRD patterns) for the CoFe_Znx (with x=0, 0.30, 0.46, 0.53) samples. The last column lists the weighted indexes of agreement.

Sample	a (Å)	Cationic distribution	Rw (%)
CoFe_Zn0	8.390(2)	$(Fe_{0.73}Co_{0.27})[Fe_{1.26}Co_{0.74}]O_4$	5.79
CoFe_Zn0.30	8.414(2)	$(Fe_{0.38}Co_{0.42}Zn_{0.20})[Fe_{1.62}Co_{0.28}Zn_{0.10}]O_4$	6.19
CoFe_Zn0.46	8.418(2)	$(Fe_{0.30}Co_{0.44}Zn_{0.26})[Fe_{1.70}Co_{0.10}Zn_{0.20}]O_4$	6.12
CoFe_Zn0.53	8.433(2)	$(Fe_{0.28}Co_{0.39}Zn_{0.33})[Fe_{1.72}Co_{0.08}Zn_{0.20}]O_4$	6.50

The lattice parameter has been found to linearly increase with increasing Zn content (**Fig. 4.4.4**) in agreement with the Vegard rule(Vegard, 1921) suggesting the insertion of the zinc in the spinel structure. Indeed, the lattice parameters of mixed ferrites are often a linear interpolation of the lattice constants of the extreme phases, i.e. $CoFe_2O_4$ (8.38 Å) and $ZnFe_2O_4$ (8.44 Å).(Smit and Wijn, 1959)
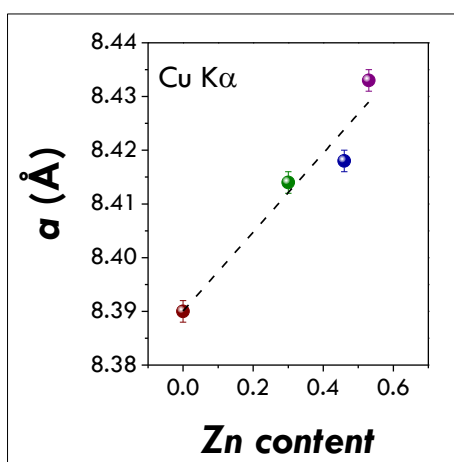
Fig. 4.4.4 Lattice parameter as a function of the Zn content for the CoFe_Znx (with x=0 (*red sphere*), 0.30 (*green sphere*), 0.46 (*blue sphere*), 0.53 (*purple sphere*)) samples with the corresponding linear curve fitting (*dashed line*, $y = 8.39 + 0.073x$; R^2=0.91512).

A raw estimation of the distribution of the metallic cations in the tetrahedral and octahedral sites has been attempted by the Rietveld method (**Fig. 4.4.3, Tab. 4.4.2**) but we can consider them just as general tendencies because iron, cobalt and zinc are characterised by similar X-ray crossing section values. Nevertheless, these data suggest that the samples are characterised by partially inverse structures. In particular, the cobalt ferrite sample seems to have an inversion degree of about 0.70, which is a value often reported in the literature for cobalt ferrite NPs.(Blanco-Gutiérrez et al., 2012; Carta et al., 2009; D Carta et al., 2013; Fantechi et al., 2012; Peddis et al., 2011) Moreover, the inversion degree further drops down when zinc ions replace cobalt ones within the structure. This can be explained by taking into account the general preference of Zn^{2+} for tetrahedral coordination rather than octahedral one, which probably forces Fe^{3+} to occupy octahedral sites.

4.4.2 Transmission Electron Microscopy (TEM, HR-TEM)

The morphological features of the $Zn_xCo_{1-x}Fe_2O_4$ NPs, such as the shape, size and size distribution, were studied by means of two different transmission electron microscopes located in the laboratories of the University of Cagliari (200 kV-JEM 2010 UHR, **Fig. 4.4.5**) and the University College London (120 kV-JEOL JEM-200 EX II, **Fig. 4.4.6**). TEM images show *pseudo*-spheroidal *log normal*-distributed NPs with similar sizes for all the samples. A mean diameter and a polidispersity index of 7.5$\pm$0.4 nm and 22$\pm$2 %, respectively, were obtained by the 200 kV microscope, (**Fig. 4.4.7**, *left panel*). These values have been confirmed by the analyses with the 120 kV microscope resulting in a mean diameter of 7.4$\pm$0.4 nm and a polidispersity index of 20$\pm$2 % (**Fig. 4.4.7**, *right panel*).
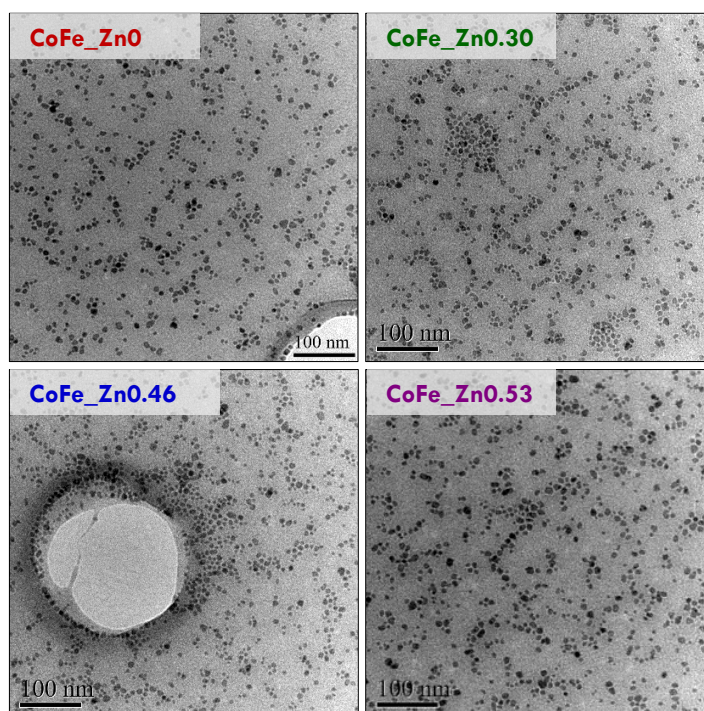
Fig. 4.4.5 TEM images for the CoFe_Znx (with x=0, 0.30, 0.46, 0.53) samples obtained by the microscope located at the University of Cagliari (200 kV-JEM 2010 UHR).
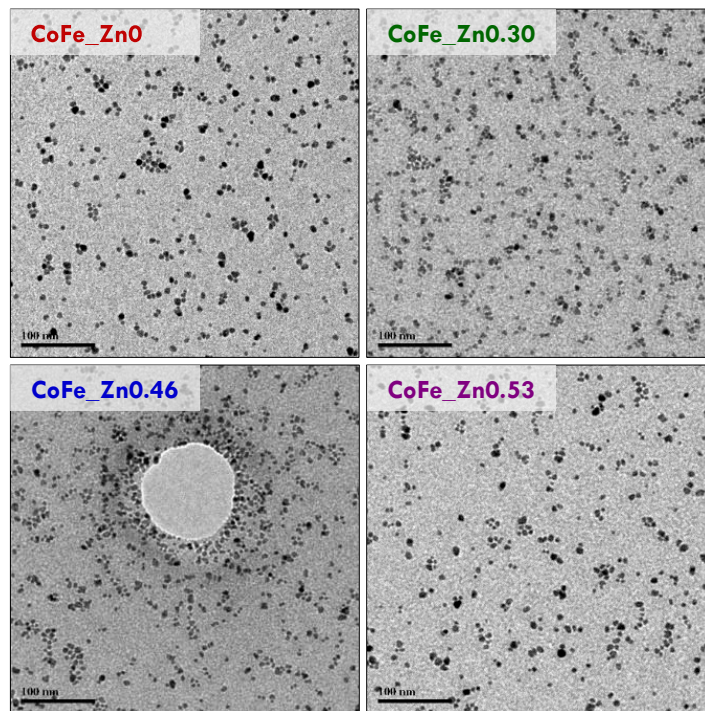
Fig. 4.4.6 TEM images for the CoFe_Znx (with x=0, 0.30, 0.46, 0.53) samples obtained by the microscope located at the University College London (120 kV-JEOL JEM-200 EX II).
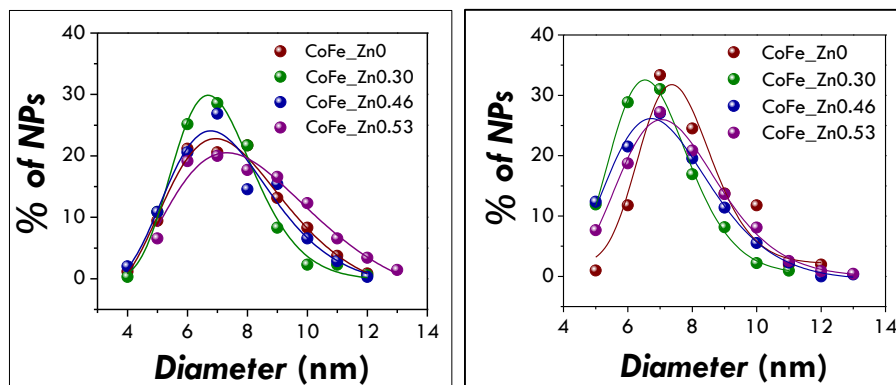
Fig. 4.4.7 Particle size distributions of the CoFe_Znx (with x=0, 0.30, 0.46, 0.53) samples estimated by means of two different transmission electron microscopes located at the University of Cagliari (200 kV-JEM 2010 UHR, *left panel*) and at University College London (120 kV-JEOL JEM-200 EX II, *right panel*).

Tab. 4.4.3 Crystallite sizes, particle sizes and polydispersity indexes (σ_{TEM}) of the CoFe_Znx (with x=0, 0.30, 0.46, 0.53) samples obtained by different diffractometers (_XRD1_: Cu X-ray source, University of Cagliari; _XRD2_: Co X-ray source, University College London) and different microscopes (_TEM1_: 200 kV-JEM 2010 UHR, University of Cagliari; _TEM2_: 120 kV-JEOL JEM-200 EX II, University College London).

Sample	$<D_{XRD1}>$ (nm) *Cu Kα*	$<D_{XRD2}>$ (nm) *Co Kα*	$<D_{TEM1}>$ (nm)	σ_{TEM1} (%)	$<D_{TEM2}>$ (nm)	σ_{TEM2} (%)
CoFe_Zn0	6.1±0.3	6.0±0.1	7.5	22	7.7	18
CoFe_Zn0.30	5.9±0.2	5.8±0.1	7.1	19	6.9	18
CoFe_Zn0.46	6.0±0.3	6.0±0.2	7.3	22	7.3	22
CoFe_Zn0.53	6.7±0.4	6.6±0.2	8.0	24	7.6	21

All the TEM images allow us to exclude the presence of aggregates suggesting that the NPs are well-capped and separated by organic molecules, as expected due to the stability of their colloidal dispersions in organic solvents. Moreover, the agreement between the crystallite (~6 nm) and particle (~7.5 nm) sizes (**Tab. 4.4.3**) suggests that highly crystalline NPs were obtained. This aspect is also confirmed by HR-TEM images (**Fig. 4.4.8**) showing continuous atomic lattice fringes all over the particle and the absence of evident structural defects.
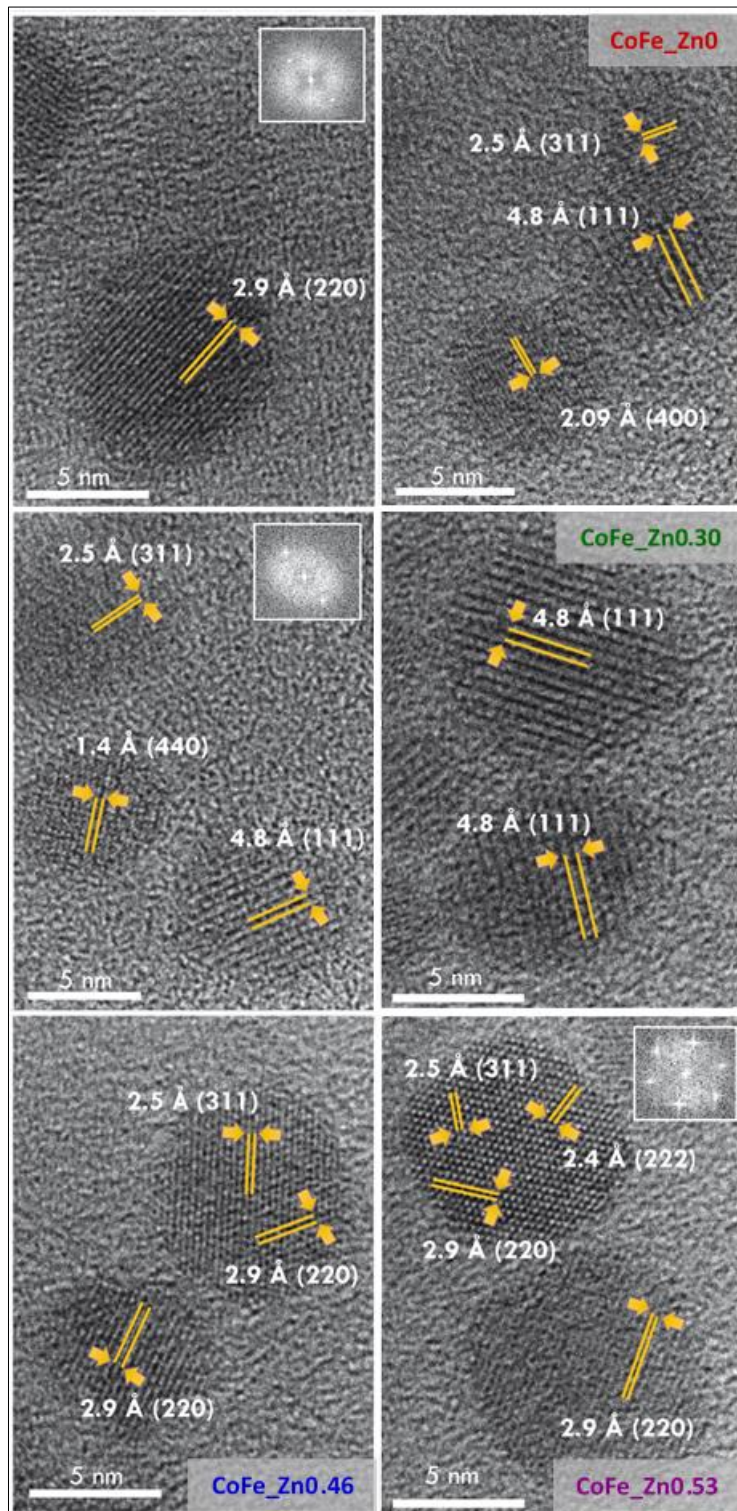
Fig. 4.4.8 High Resolution TEM images of the CoFe_Znx (with x=0, 0.30, 0.46, 0.53) samples obtained by the transmission electron microscope located at the University of Cagliari (200 kV-JEM 2010 UHR). Note that two HRTEM images are shown for the samples CoFe_Zn0 and CoFe_Zn0.30.

4.5 Capping agent

4.5.1 Fourier Transform - Infrared Spectroscopy (FT-IR)

The presence of capping agent molecules surrounding the NPs and their characterisation was conducted by FT-IR analysis. Indeed, the $Zn_xCo_{1-x}Fe_2O_4$ NPs where purified and separated from possible by-products by means of several washing steps that could in principle remove completely also the capping shell. All the FT-IR spectra show as principal vibrational modes the ones typical for the hydrocarbon chain (asymmetric and symmetric CH stretching of CH_2 and CH_3 groups) and the carboxylate groups (asymmetric and symmetric COO^- stretching) (**Fig. 4.5.1, Tab. 4.5.1**). This suggest that the NPs are capped by oleate groups(Cannas et al., 2010b). In addition, vibrational modes typical for the neutral amine groups (NH stretching, NH_2 bending)(Cannas et al., 2010b) have been identified, despite their low-intensity signals, indicating the presence of a few oleylamine molecules probably intercalated among the oleate ones.

The M-O (M = Co, Fe, Zn) stretching modes of spinel ferrites has been studied by a second spectrophotometer that permits to record the spectra up to 350 cm^{-1}. **Fig. 4.5.1** shows for all the samples the fingerprint range 700-400 cm^{-1}. In this spectral region two metal-oxygen stretching modes are visible. The first one, associated with the octahedral and tetrahedral sites, is found to move towards lower values with increasing zinc content, from 588 cm^{-1} for the $CoFe_2O_4$ to 572 cm^{-1} for $Zn_{0.53}Co_{0.47}Fe_{2.0}O_4$. Taking into account the values reported in the literature for cobalt (575 cm^{-1}) and zinc (555 cm^{-1}) ferrites(White and DeAngelis, 1967), this trend can be interpreted in the light of a gradual substitution of cobalt ions by zinc ones within the spinel structure. Also the second stretching mode, related only to the octahedral sites, undergoes a shift but in the opposite direction (i.e. higher wavenumber values with increasing zinc content) suggesting that the insertion of the zinc in the structure strongly affects the cationic distribution.
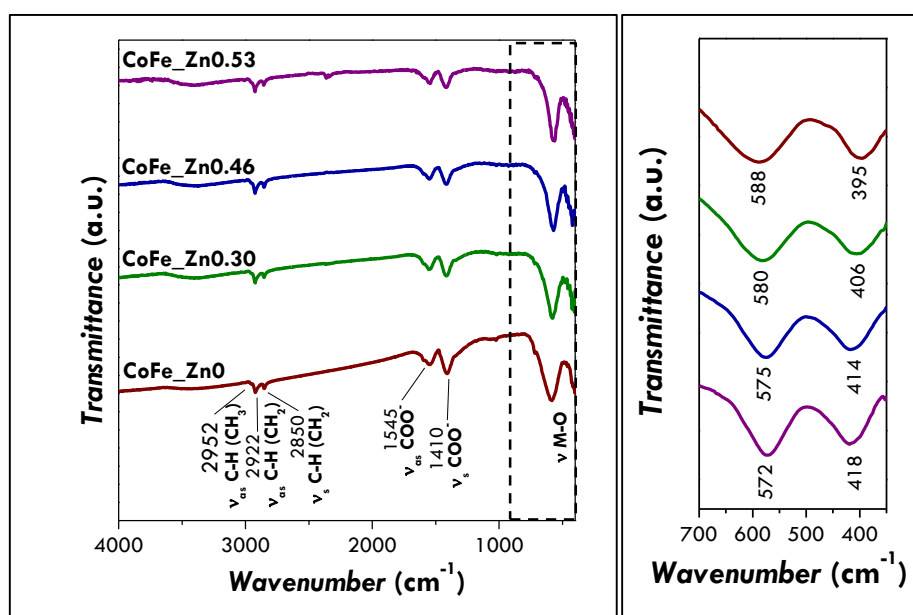
Fig. 4.5.1 Infrared spectra of the CoFe_Znx (with x=0, 0.30, 0.46, 0.53) samples recorded in the region (4000-400 cm^{-1}) (*left panel*). Infrared spectral region between 700 and 350 cm-1 with the typical metal-oxygen stretching modes (*right panel*).

Tab. 4.5.1 Assignments of the vibrational modes revealed in the FTIR spectra of the CoFe_Znx (with x=0, 0.30, 0.46, 0.53) samples.

Wavenumber (cm^{-1})				Vibrational mode
CoFe_Zn0	CoFe_Zn0.30	CoFe_Zn0.46	CoFe_Zn0.53	
3433	3400	3371	3408	N-H stretching
2952	2954	2952	2950	C-H asymmetric stretching (CH_3)
2922	2924	2924	2925	C-H asymmetric stretching (CH_2)
2850	2873	2852	2854	C-H symmetric stretching (CH_2)
1593	1595	1593	1592	NH_2 bending
1545	1550	1548	1541	COO^- asymmetric stretching
1410	1415	1414	1415	COO^- symmetric stretching
1342	1340	1346	1340	CH_3 bending
717	719	717	-	CH_2 wagging
582	577	571	569	Metal-O stretching

4.5.2 ThermoGravimetric Analysis (TGA)

TGA analyses (**Fig. 4.5.2**) have been carried out for the $Zn_xCo_{1-x}Fe_2O_4$ NPs under an inert atmosphere (50 ml/min of Ar). The curves show for all the samples two weight losses occurring between 300 and 400 °C and between 550 and 650 °C. The first one can be associated with the decomposition of the capping molecules whereas the second one to a reduction process undergone by the inorganic core under argon atmosphere as already observed by other authors for oleic acid-capped ferrite nanoparticles.(Ayyappan et al., 2011, 2008) In order to confirm this interpretation, a TGA curve has been recorded under an oxidative atmosphere (50 ml/min of O_2) on the CoFe_Zn0.53 sample (**Fig. 4.5.2**). In this case, the decomposition of the capping agent shifts towards lower temperature (between 200 and 300 °C) but produces the same weight loss as the first weight loss of the Ar-measurement. From the first weight loss in the Ar-TGA curves, the percentage of capping agent has been calculated (**Tab. 4.5.2**). Similar values have been obtained for all the samples with a mean percentage of (15±2) %.
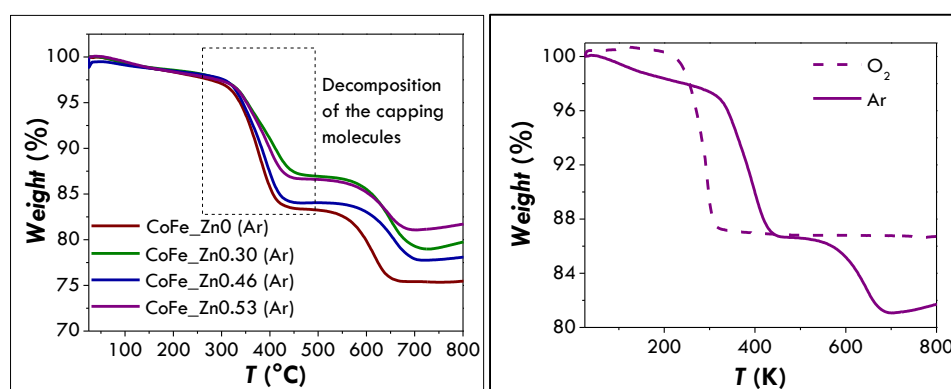
Fig. 4.5.2 TGA curves of the CoFe_Znx (with x=0, 0.30, 0.46, 0.53) samples performed under inert atmosphere (50 ml/min of Ar) (*left panel*). TGA curves collected on the CoFe_Zn0.53 sample under an inert atmosphere (50 ml/min of Ar) and an oxidative atmosphere (50 ml/min O_2) (*right panel*).

Tab. 4.5.2 Summary of the chemical composition, microstructural and morphological properties of CoFe_Znx (with x=0, 0.30, 0.46, 0.53) samples.

Sample	Chemical composition	$<D_{XRD}>$ (nm) *Cu Kα*	$<D_{XRD}>$ (nm) *Co Kα*	$<D_{TEM1}>$ (nm)	σ_{TEM1} (%)	$<D_{TEM2}>$ (nm)	σ_{TEM2} (%)	% of organic phase
CoFe_Zn0	$CoFe_2O_4$	6.1±0.3	6.0±0.1	7.5	22	7.7	18	17
CoFe_Zn0.30	$Zn_{0.30}Co_{0.70}Fe_{2.00}O_4$	5.9±0.2	5.8±0.1	7.1	19	6.9	18	13
CoFe_Zn0.46	$Zn_{0.46}Co_{0.54}Fe_{2.02}O_4$	6.0±0.3	6.0±0.2	7.3	22	7.3	22	16
CoFe_Zn0.53	$Zn_{0.53}Co_{0.47}Fe_{2.02}O_4$	6.7±0.4	6.6±0.2	8.0	24	7.6	21	13

It can be easily demonstrated that this amount of capping agent corresponds to a low-dense packing of a monolayer of oleate molecules surrounding the surface of the nanoparticles (**Fig. 4.5.3**). Indeed, other authors have indicated that for a close-packed monolayer of oleate molecules, each molecule has 20-30 Å^2 as available area on the particle surface.(Ayyappan et al., 2008; Gnanaprakash et al., 2007; van Ewijk et al., 1999) For the CoFe_Znx sample, considering a mean diameter of 7.5±0.4 nm and a spheroidal shape for the NPs, a surface area of 177 nm^2 is obtained. A 15±2 % of organic capping corresponds to ~3.2·10^{20} oleate molecules. Taking into account the *bulk*-CoFe$_2$O$_4$ density of 5.3 g/cm^3 and the volume of a single spheroidal NP with a diameter of 7.5 nm, an 85% of inorganic phase corresponds to a number of spinel ferrite NPs of 7.3·10^{17}. The number of capping molecules per particle, obtained as the ratio between the number of oleate molecules and the number of NPs should, is about 440 molecules/nanoparticle. Finally, the nanoparticle surface area (177 nm^2) over the number of molecules provides a surface area occupied by each oleate molecule of 40 Å^2. This may suggests a low-dense packing of the molecules on the NPs' surface. The complete calculation, considering the dispersion on the inorganic core diameter and on the capping agent amount, is reported in **Tab. 4.5.3**.
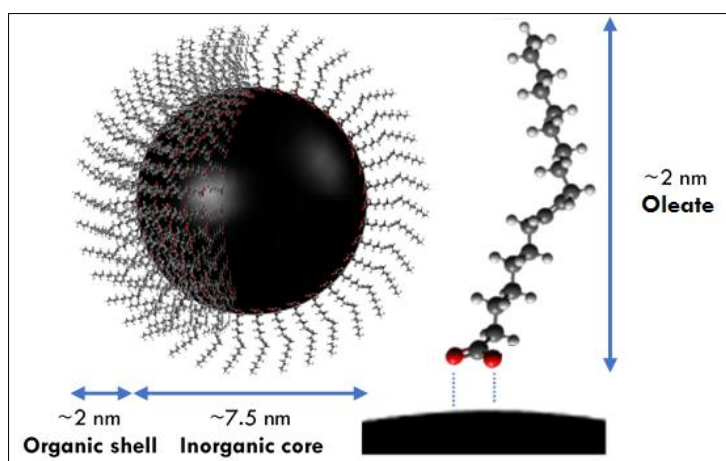
Fig. 4.5.3 Sketch based on the FTIR/TGA data of the hybrid nanostructures forming the CoFe_Znx (with x=0, 0.30, 0.46, 0.53) samples. The inorganic core is surrounded by a monolayer of oleate molecules.

Tab. 4.5.3 Computation of the available area for each oleate (OA) molecule on the nanoparticle (NP) surface. The results are given in the last column (A per OA molecule). D_{TEM} is the particle diameter estimated by TEM analyses. A_{NP} is the particle surface area. V_{NP} is the volume of a nanoparticle. The mass of a single nanoparticle (calculated considering a density of 5.3 g/cm^3) is indicated as *m of a single NP*; the number of nanoparticles in one gram of sample, calculated from TGA data, is given as *# NPs per g of sample*; *mOA per g of sample* is the percentage of capping agent obtained from TGA; n_{OA} and *# OA molec. per g of sample* are the corresponding number of moles and number molecules of oleate, respectively; *# OA molec. per single NP* is the number of oleate molecules surrounding each nanoparticle.

D_{TEM} (nm)	A_{NP} (nm^2)	V_{NP} (nm^3)	m of a single NP (g)	# NPs per g of sample	m_{OA} per g of sample	n_{OA} (mmol)	# OA molec. per g of sample	# OA molec. per single NP	A per OA molecule (Å^2)
7.5	177	221	1.17E-18	7.3E+17	**0.15**	0.53	3.2E+20	440	40
7.5	177	221	1.17E-18	7.4E+17	**0.13**	0.46	2.8E+20	373	47
7.5	177	221	1.17E-18	7.1E+17	**0.17**	0.60	3.6E+20	511	35
7.1	158	187	9.93E-19	8.6E+17	0.15	0.53	3.2E+20	374	42
7.9	196	258	1.37E-18	6.2E+17	0.15	0.53	3.2E+20	515	38

Moreover, the first derivative of the thermogravimetric curve (DTG) points out that the weight loss is made up by two steps in the case of the zinc-substituted samples (**Fig. 4.5.4**). This can be probably related to different interactions between the capping molecules and the inorganic cores that occur exclusively when the zinc is present in the structure. For instance, it can be related to different bond strengths between the oleate group and the different surface metal ions.
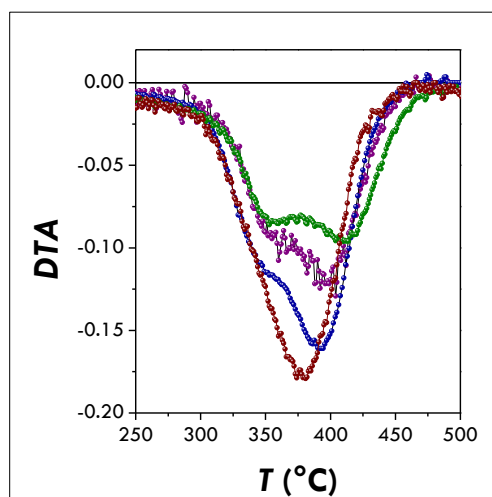
Fig. 4.5.4 First derivative of the TGA curves (DTG) of the CoFe_Znx (with x=0 (*red sphere*), 0.30 (*green sphere*), 0.46 (*blue sphere*), 0.53 (*purple sphere*)) samples.

In conclusion, the results of the FT-IR and TGA analyses indicate that all the samples are hybrid organic-inorganic nanostructures made of inorganic core of about 7.5 nm capped by a single layer of oleic acid molecules (~2 nm in length), giving raise to not-aggregated NPs with similar interparticles distances as observed by TEM analyses.

4.6 Magnetic properties and heating abilities

The similarities, highlighted by the careful and multi-technique characterisation, on the particle size, particle size distribution, crystallite size and capping agent amount, establish an ideal context to discuss the magnetic properties and the heating abilities of these samples exclusively as a function of the chemical composition effect caused by different zinc content.

4.6.1 Low temperature magnetic properties and cationic distribution.

M vs H curves have been measured at 5 K (**Fig. 4.6.1**) and the values of the main magnetic quantities have been estimated (**Tab. 4.6.1**).
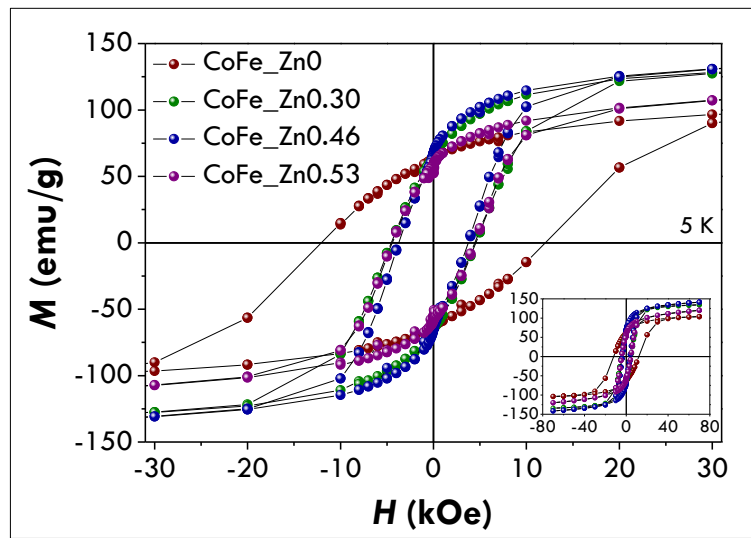
Fig. 4.6.1 Field dependence of the magnetisation at 5 K for the CoFe_Znx (with x=0, 0.30, 0.46, 0.53) samples.

Tab. 4.6.1 5 K Magnetic properties of CoFe_Znx (with x=0, 0.30, 0.46, 0.53) samples. H_c, H_{sat} and M_{7T} are the coercivity, the saturation field and the magnetisation at 7 T. M_{s1} and M_{s2} are saturation magnetisation values estimated by the equations $M = M_{s1} + b\frac{1}{H}$ and $M = M_{s2} \cdot \left(1 - \frac{a}{H} - \frac{b}{H^2}\right)$, respectively.(Morrish, 1965) In addition, the corresponding magnetic remanence values are listed in the last two columns.

Sample	Hc (kOe)	Hsat (kOe)	M7T (emu/g)	Ms1 (emu/g)	Ms2 (emu/g)	Mr/Ms1	Mr/Ms2
CoFe_Zn0	12±1	36±4	104±2	110±2	109±3	0.58±0.03	0.58±0.03
CoFe_Zn0.30	4.6±0.5	22±2	134±3	139±3	142±3	0.46±0.02	0.45±0.02
CoFe_Zn0.46	3.7±0.4	21±4	141±3	150±3	157±3	0.43±0.02	0.42±0.02
CoFe_Zn0.53	4.4±0.4	17±2	120±2	131±3	140±3	0.44±0.02	0.41±0.02

All the curves show a hysteretic behaviour without any anomalous shape associated with mixtures of hard/soft isostructural spinel phases.(Song and Zhang, 2012) This is consistent with the presence of a unique spinel cubic phase. In order to furtherly, verify the presence of a single spinel phase, the field dependence of the remanent magnetisation has been studied by means of the DCD protocol. The first derivative of the DCD

curve (**Fig. 4.6.2**) can be useful to study the distribution of the particle coercive fields, known also as the switching field distribution.
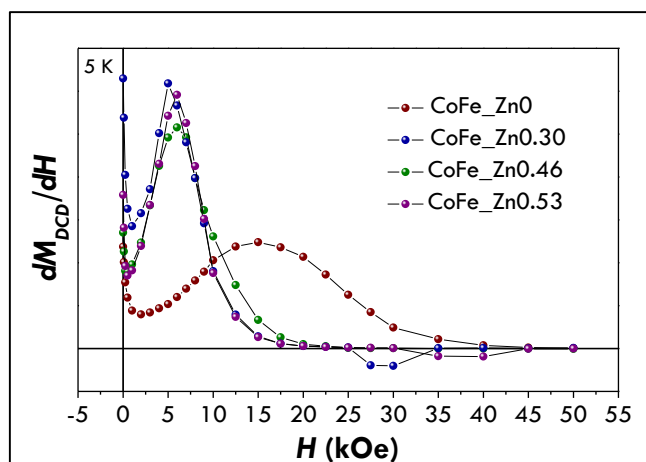
Fig. 4.6.2 First derivative of the DCD curves of the CoFe_Znx (with x=0, 0.30, 0.46, 0.53) samples.

A single peak is shown for all the samples, confirming the presence of a unique spinel phase.(Muscas et al., 2015) Furthermore, the cobalt ferrite nanoparticles exhibit a field distribution centred at higher magnetic field ($H_{DCD} \approx 15.5$ kOe) with respect to the zinc-substituted ones (between 5 and 6 kOe).

The hysteresis loop for the cobalt ferrite is characterised by a high coercive field, H_c, (12 ± 1 kOe) near the values previously reported for nanoparticles of similar size(Duong et al., 2006; Fantechi et al., 2012; Peddis et al., 2013; Song and Zhang, 2006). The coercive fields for the Zn-doped samples were found to be equal to 4.6 ± 0.5 kOe (x=0.30), 3.7 ± 0.4 kOe (x=0.46) and 4.4 ± 0.4 kOe (x=0.53). The reduced values of coercive field for the Zn-containing samples with respect to the unsubstituted one is probably due to a decrease of the magnetocrystalline anisotropy occurring when Zn^{2+} replaces Co^{2+}. It is interesting to note that an increase of x between 0.3 and 0.53 does not change significantly the coercivity. The same trend has been recorded for the saturation field (H_{sat}), which represents the field necessary to reverse the magnetisation of all the nanoparticles. The saturation magnetisation (M_s) for the cobalt ferrite is about 110 emu/g, higher than the value usually reported for bulk-$CoFe_2O_4$ (80-90 emu/g)(Cullity and Graham, 2009; Smit and Wijn, 1959). This may suggest a partially inverse structure.(Peddis et al., 2011) As Zn^{2+} enters the structure, M_s increases up to about 150-160 emu/g for a Zn content of 0.46 and decreases for higher Zn concentration ($\sim$130-140 emu/g). The reduced remnant magnetisation (M_r/M_s) has been found to be equal to 0.58 for the pure cobalt ferrite and lower than 0.5 for the Zn-doped samples. Although the value of 0.58 is not very close to the theoretical one (being equal to 0.83(Walker et al., 1993)), it suggests that $CoFe_2O_4$ nanoparticles tend to cubic anisotropy whereas substitution by Zn^{2+} leads to uniaxial anisotropy nanoparticles.

From these data, it seems that the increase of Zn^{2+} in the zinc-substituted samples produces a selective tuning of the saturation magnetisation without any changes in the anisotropy, contrarily to what already reported in the literature.(Singhal et al., 2010; Topkaya et al., 2012) This effect could be probably explained by taking into account the cationic distribution and the inversion degree (i). In particular, it can be hypothesized that the

samples are characterised by a partially inverse spinel structure (i.e. $i<1$) and that the Zn^{2+} ions occupy preferentially tetrahedral sites (**Fig. 4.6.3**, **Fig. 4.6.4**).
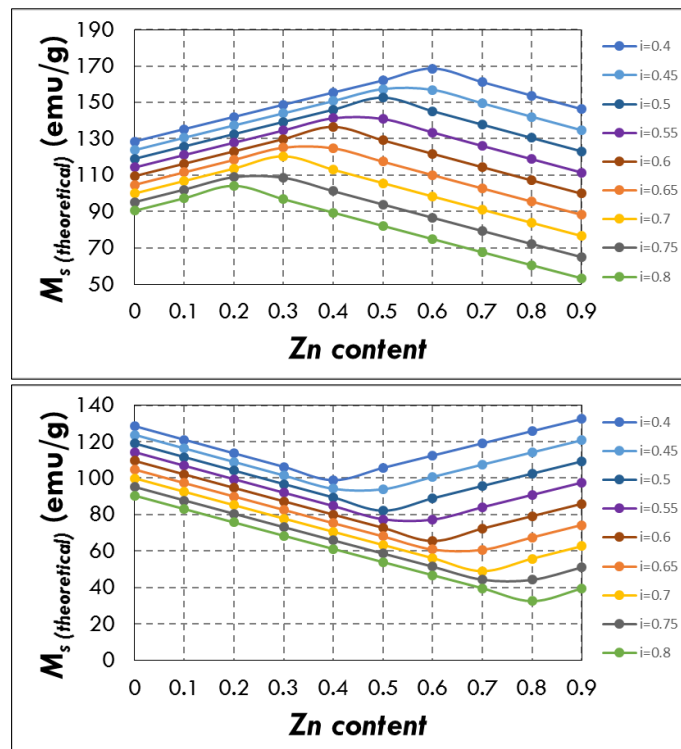
Fig. 4.6.3 Theoretical saturation magnetisation (Ms) based on the Néel model (i.e. independent magnetic sublattices of the spinel ferrite magnetic structure) for different inversion degree values ($0.4 \leq i \geq 0.8$, different coloured curves) assuming that the Zn^{2+} occupy preferentially T_d sites (upper panel) or O_h sites (bottom panel). The values have been calculated by means of the formula: $M_s = \dfrac{\mu \cdot \mu_B \cdot N_A}{MM}$, where μ is the total magnetic moment, μ_B is the Bohr magneton, N_A is the Avogadro number and MM is the molar mass.
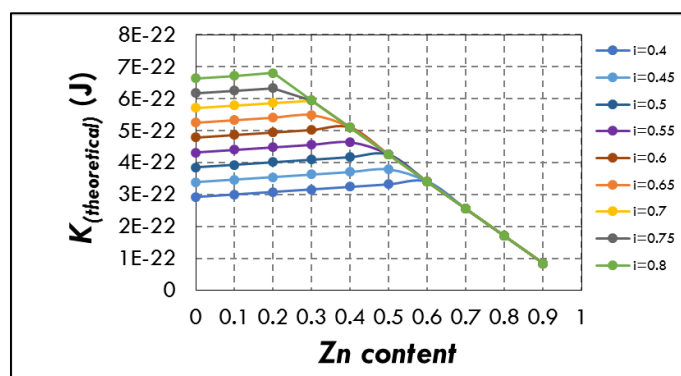
Fig. 4.6.4 Theoretical anisotropy constant for $Zn_xCo_{1-x}Fe_2O_4$ as a function of the zinc content and for different inversion degree values ($0.4 \leq i \geq 0.8$, *different coloured curves*). The anisotropy constant is calculated as sum of the single ion anisotropy of the Co^{2+} (Co^{2+} in T_d sites has a $K = -79 \cdot 10^{-24}$ J/ion; Co^{2+} in O_h sites has a $K = +850 \cdot 10^{-24}$ J/ion). The curves are obtained by assuming that the Zn^{2+} occupy preferentially T_d sites.

In order to confirm this hypothesised scenario, ^{57}Fe Mössbauer Spectroscopy measurements have been carried out at 4.2 K in the absence (**Fig. 4.6.5, Fig. 4.6.6, Tab. 4.6.2**) and in the presence (**Fig. 4.6.7, Fig. 4.6.8, Tab. 4.6.3, Tab. 4.6.4**) of an intense magnetic field (6 T). These measurements allow to obtain information on the iron occupancies and on the presence of spin-canting phenomena, i.e. internal or surface disorder.
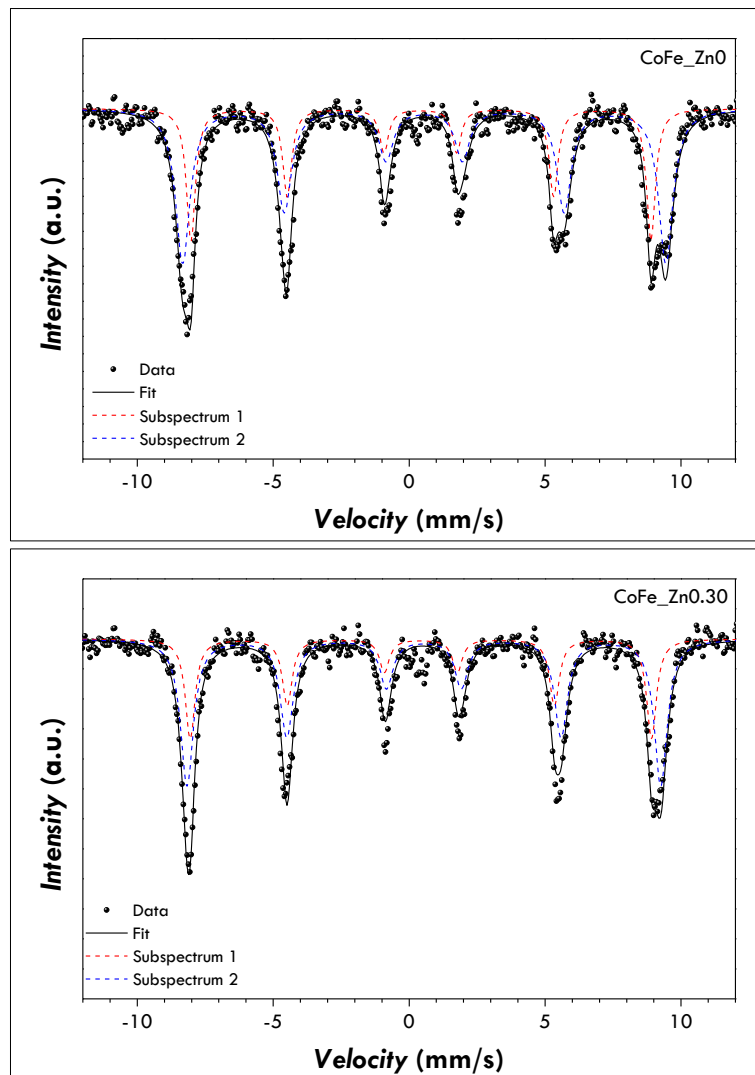
Fig. 4.6.5 4.2 K Mössbauer spectra of the CoFe_Zn0 (*upper panel*) and CoFeZn_0.30 (*bottom panel*) samples recorded in the absence of an external magnetic field. Note that the doublet in the centre of the spectra is related to the metallic iron dissolved in the aluminium foil used as sample holder.
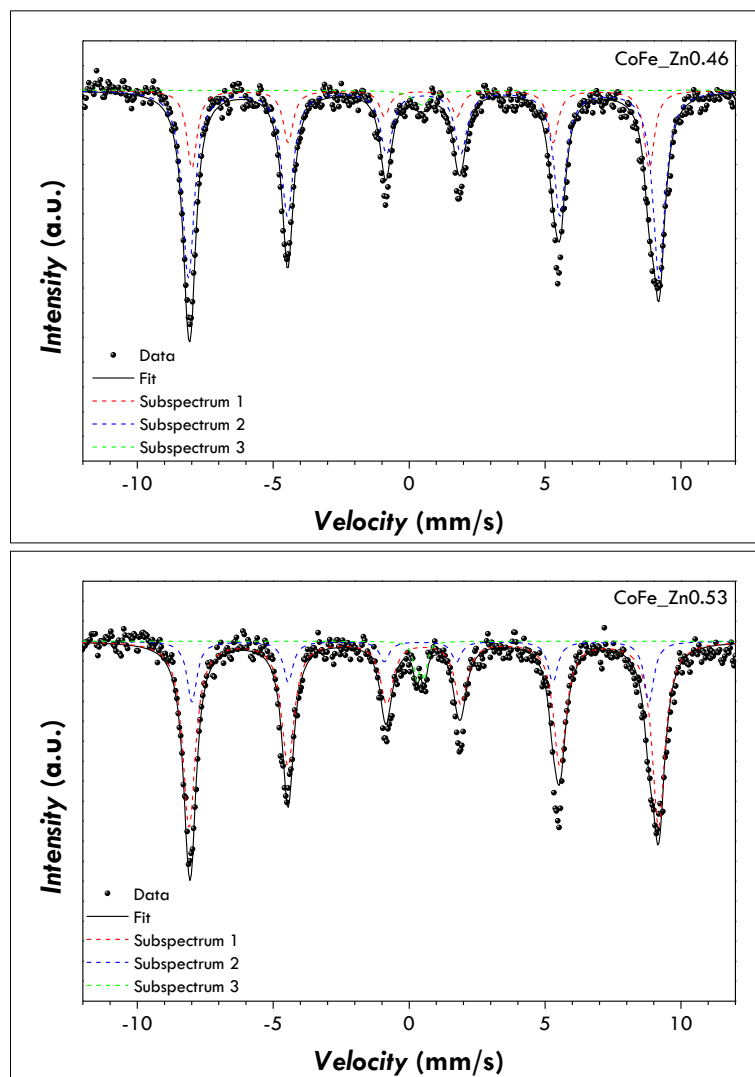
Fig. 4.6.6 4.2 K Mössbauer spectra of the CoFe_Zn0.46 (*upper panel*) and CoFeZn_0.53 (*bottom panel*) samples recorded in the absence of an external magnetic field. Note that the doublet in the centre of the spectra is related to the metallic iron dissolved in the aluminium foil used as sample holder.
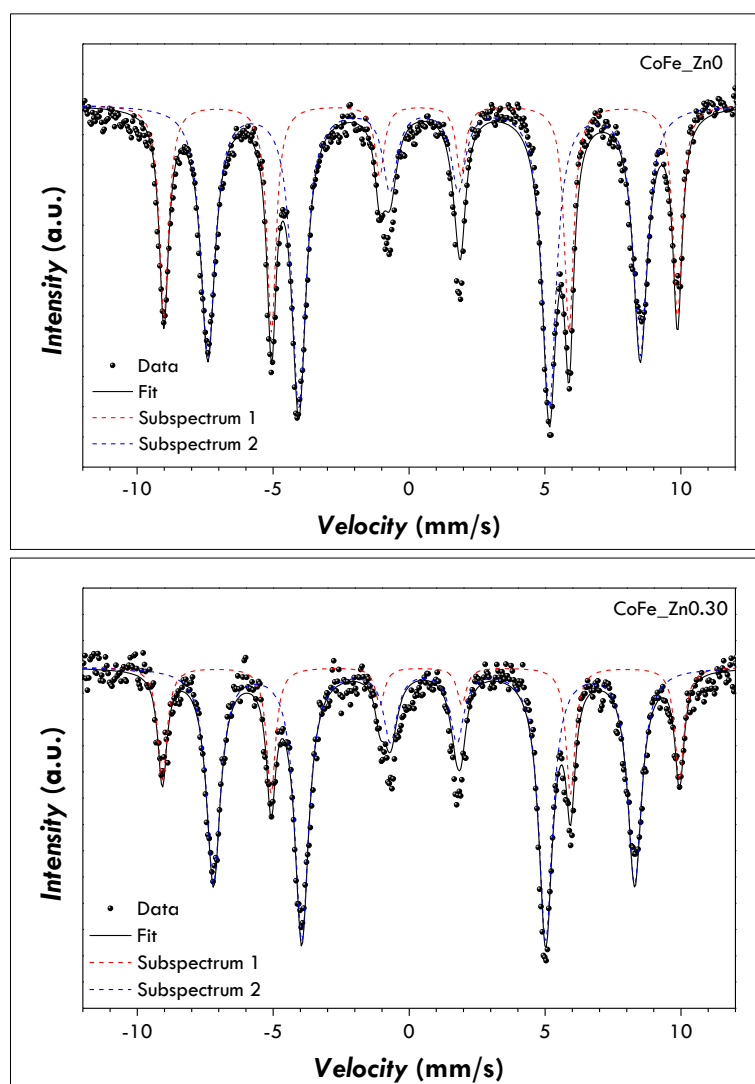
Fig. 4.6.7 4.2 K Mössbauer spectra of the CoFe_Zn0 (*upper panel*) and CoFeZn_0.30 (*bottom panel*) samples recorded in the presence of an intense external magnetic field (6 T).
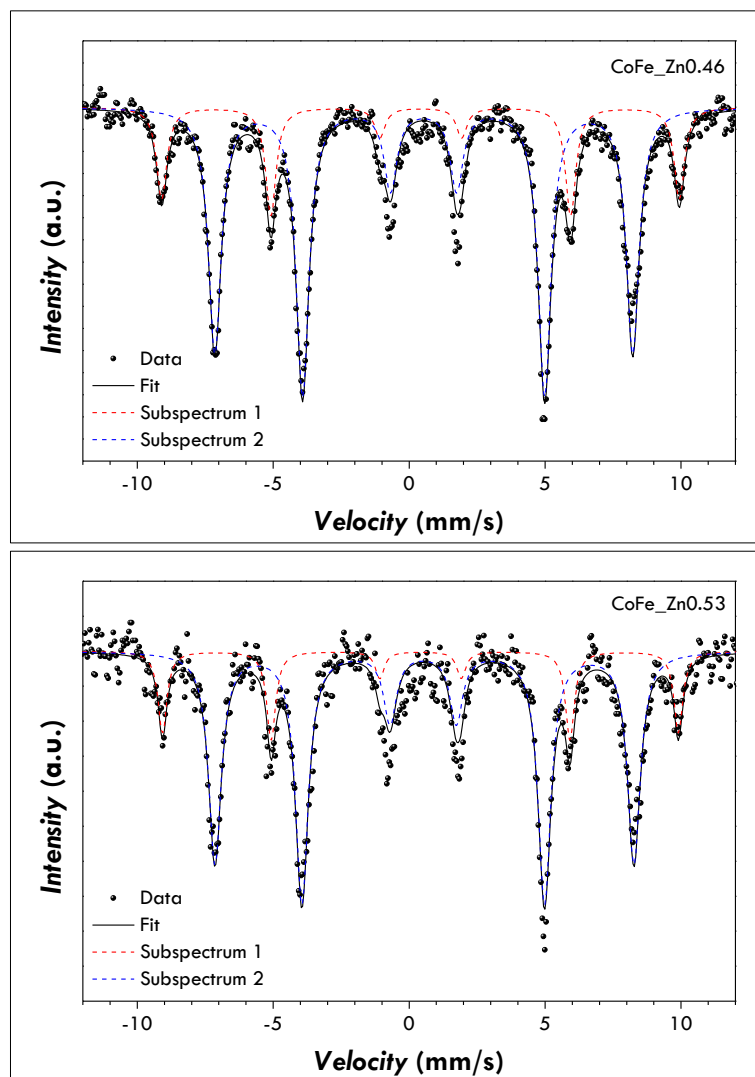
Fig. 4.6.8 4.2 K Mössbauer spectra of the CoFe_Zn0.46 (*upper panel*) and CoFeZn_0.53 (*bottom panel*) samples recorded in the presence of an intense external magnetic field (6 T).

Tab. 4.6.2 Mössbauer parameters of the CoFe_Znx (with x=0, 0.30, 0.46, 0.53) samples spectra recorded at 4.2 K in the absence of an external magnetic field (0 T): isomer shift (δ), quadrupole splitting (ΔE_Q), hyperfine field (B_{Hf}) and Full-Width at Half-Maximum (FWHM). Last column lists the interpretation for each subspectrum.

Sample	Subsp.	δ (mm/s)	ΔE_Q (mm/s)	B_{Hf} (T)	FWHM (mm/s)	Interpretation
CoFe_Zn0	1	0.42	0.02	52.6(3)	0.40	tetrahedral sites of a spinel
	2	0.56	0.00	55.2(3)	0.64	octahedral sites of a spinel
CoFe_Zn0.30	1	0.43	0.00	52.7(3)	0.43	tetrahedral sites of a spinel
	2	0.54	0.00	54.1(3)	0.58	octahedral sites of a spinel
CoFe_Zn0.46	1	0.42	0.00	52.3(3)	0.45	tetrahedral sites of a spinel
	2	0.54	0.00	53.8(3)	0.54	octahedral sites of a spinel
CoFe_Zn0.53	1	0.42	0.00	52.2(3)	0.43	tetrahedral sites of a spinel
	2	0.54	0.00	53.6(3)	0.56	octahedral sites of a spinel

Tab. 4.6.3 Mössbauer parameters of the CoFe_Znx (with x=0, 0.30, 0.46, 0.53) samples spectra recorded at 4.2 K under an intense magnetic field (6 T): isomer shift (δ), quadrupole splitting (ΔE_Q), effective magnetic field (B_{Hf}), Full-Width at Half-Maximum (FWHM) and relative area (A) of the components. Last column lists the interpretation for each subspectrum.

Sample	Subsp.	δ (mm/s)	ΔE_Q (mm/s)	B_{eff} (T)	FWHM (mm/s)	A (%)	Interpretation
CoFe_Zn0	1	0.42	0.02	58.7(1)	0.41	35	Fe^{III} in tetrahedral sites of a spinel
	2	0.56	0.00	49.4(1)	0.63	65	Fe^{III} in octahedral sites of a spinel
CoFe_Zn0.30	1	0.43	0.00	59.1(1)	0.41	25	Fe^{III} in tetrahedral sites of a spinel
	2	0.54	0.01	48.1(1)	0.61	75	Fe^{III} in octahedral sites of a spinel
CoFe_Zn0.46	1	0.42	-0.01	59.1(1)	0.46	23	Fe^{III} in tetrahedral sites of a spinel
	2	0.54	0.01	47.7(1)	0.57	77	Fe^{III} in octahedral sites of a spinel
CoFe_Zn0.53	1	0.42	0.00	58.9(1)	0.40	21	Fe^{III} in tetrahedral sites of a spinel
	2	0.54	0.05	47.8(1)	0.57	79	Fe^{III} in octahedral sites of a spinel

Tab. 4.6.4 Cationic distribution of the CoFe_Znx (with x=0, 0.30, 0.46, 0.53) samples obtained by in-field low temperature Mössbauer Spectroscopy.

Sample	Cationic distribution
CoFe_Zn0	$(Co_{0.30(1)}Fe_{0.70(1)})[Co_{0.70(1)}Fe_{1.30(3)}]O_4$
CoFe_Zn0.30	$(M^{II}_{0.50(3)}Fe_{0.50(2)})[M^{II}_{0.50(1)}Fe_{1.50(3)}]O_4$
CoFe_Zn0.46	$(M^{II}_{0.54(2)}Fe_{0.46(2)})[M^{II}_{0.46(1)}Fe_{1.54(3)}]O_4$
CoFe_Zn0.53	$(M^{II}_{0.58(5)}Fe_{0.42(3)})[M^{II}_{0.42(1)}Fe_{1.58(5)}]O_4$

All the spectra can be fitted by two well separated sextets related to ferric ions located in the tetrahedral and octahedral sites of a spinel structure. The values of isomer shift have been found to be higher than the

values typical for ferric ions at room temperature (~0.33 mm/s). This is something expected as the isomer shift usually increases with decreasing temperature. The distribution of iron ions in the octahedral and tetrahedral sites of the spinel structure can be obtained by means of the in-field measurements carried out at low temperature (**Tab. 4.6.4**). The cationic distribution for the pure cobalt ferrite has been found to be $(Co_{0.30}Fe_{0.70})[Co_{0.70}Fe_{1.30}]O_4$ with an inversion degree of 0.70, in agreement with previous works on $CoFe_2O_4$ nanoparticles synthesized by different methods.(Blanco-Gutiérrez et al., 2012; Carta et al., 2009; D. Carta et al., 2013; Fantechi et al., 2012; Peddis et al., 2011) The substitution of cobalt ions with zinc ones leads to a spinel structure with reduced inversion degree, which has been found equal to 0.50, 0.46, 0.42 for the samples CoFe_Zn0.30, CoFe_Zn0.46 and CoFe_Zn0.53, respectively. This decrease in the inversion degree can be justified by taking into account the affinity of Zn^{2+} for tetrahedral sites(Sharifi and Shokrollahi, 2012; Sickafus et al., 2004; Topkaya et al., 2012; Veverka et al., 2010), which probably force the Fe^{3+} to occupy octahedral ones. Moreover, the effective field values (B_{eff}) are similar in all the samples for T_d sites (about 59 T) whereas the B_{eff} values for O_h sites are lower in the case of the zinc-substituted samples (48 T) with respect to the cobalt ferrite (49 T). This means that the hyperfine field experienced by ferric ions with octahedral coordination is lower, as confirmed by the analysis of the 4 K Mössbauer spectra recorded under zero field (**Tab. 4.6.5**). Now, we should take into account that the first neighbouring sites for an octahedral one are the tetrahedral interstices and that the exchange interactions between octahedral and tetrahedral atoms (J_{AB}) are stronger than the ones between two tetrahedral atoms (J_{AA}) or two octahedral ones (J_{BB}). As a consequence, the effective field of the octahedral sublattice will be more affected than the effective field of tetrahedral sublattice when the diamagnetic Zn atoms will be in tetrahedral positions. Therefore, with the increasing of Zn substitution, the B_{eff} values of octahedral sublattice decreases while the B_{eff} values for tetrahedral sublattice remain almost constant. These data suggest again that the insertion of zinc in the structure involves preferentially 4-fold coordination sites in agreement with the hypothesised interpretation.

The Mössbauer measurements on the $CoFe_2O_4$ provides the complete cationic distribution for this sample. The theoretical M_s value for this cationic distribution can be calculated on the basis of the Néel model which accounts for the existence of two magnetic sublattices in the spinel structure. This value has been found equal to 100 emu/g, which is slightly lower than the observed experimental M_s value (~110 emu/g). The discrepancy between the theoretical value and the experimental one can be explained by taking into account that this model does not consider the orbital contribute to the magnetic moment, which is actually not-negligible in the case of cobalt ions-containing ferrites, or to the presence of canted spins.(Smit and Wijn, 1959) Between these two explanations, the second one can be excluded because the canting angle have been found to be around zero for all the samples (**Tab. 4.6.5**).

The in-field measurements were done in a perpendicular arrangement (**Fig. 4.6.9**) of the external magnetic field with respect to the γ-beam and are useful to get information about the cationic distribution and the canting phenomena in the spinel structure. Generally, two arrangements are used for the in field Mössbauer measurements. In the parallel arrangement the magnetic field is parallel to the γ-beam whereas in the perpendicular one the magnetic field is applied perpendicularly to it. Effective magnetic field ($\overrightarrow{B_{eff}}$) which

causes the splitting of Mössbauer spectra into sextets is sum of two vectors: the hyperfine field ($\overrightarrow{B_{Hf}}$) and external field ($\overrightarrow{B_{app}}$):

$$\overrightarrow{B_{eff}} = \overrightarrow{B_{Hf}} + \overrightarrow{B_{app}}$$

Eq. 4.6.1

Canting angles can be directly calculated from sextets' lines area for a parallel γ-beam − $\overrightarrow{B_{app}}$ arrangement because when canting angle is zero the intensity of the 2nd and 5th lines is zero. Therefore, all the deviations from this conditions can be easily detected. On the contrary, in the case of perpendicular γ-beam − $\overrightarrow{B_{app}}$ arrangement, the 2nd or 5th lines of Mössbauer spectra's sextets have intensity different from zero rendering the computation of the canting angles from the intensity not trivial.

Nevertheless, for a perpendicular arrangement the angle θ between the magnetic moment ($\vec{\mu}$) and the applied magnetic field can be estimated thanks to the following cosine equation:

$$B_{eff}^2 = B_{hf}^2 + B_{app}^2 - 2B_{hf}B_{app}cos\theta$$

Eq. 4.6.2

Where B_{hf} is the hyperfine field, B_{eff} the effective magnetic field and B_{app} the external applied magnetic field.
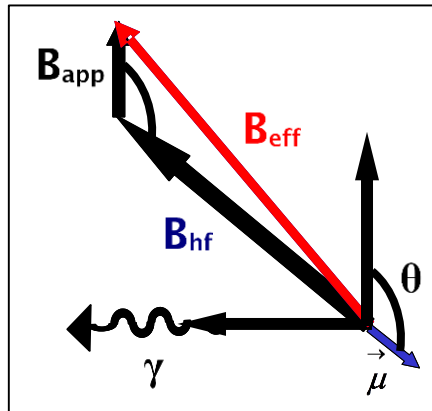
Fig. 4.6.9 Sketch of the perpendicular arrangement used in in field Mössbauer measurements. B_{hf} is the hyperfine field, B_{eff} the effective magnetic field, B_{app} the external applied magnetic field and θ is the angle between the magnetic moments in the structure and B_{app}.

The angle θ corresponds to the canting angle for the octahedral sites whereas for the tetrahedral ones, the canting angle is equal to π-θ. This is caused by the relative arrangement of the hyperfine and applied fields vectors that are parallel or antiparallel aligned for tetrahedral or octahedral sites, respectively.

Tab. 4.6.5 Computation of spin canting angle by means of the cosine equation (Eq. 4.6.2). B_{hf} is the hyperfine field, B_{eff} the effective magnetic field, B_{app} the external applied magnetic field and θ is the angle between the magnetic moments in the structure and B_{app}.

Sample	Sites	B_{app} (T)	B_{Hf} (T)	B_{eff} (T)	B_{Hf}^2 (T)	B_{eff}^2 (T)	B_{app}^2 (T)	cosθ
CoFe_Zn0	Fe T_d	6	52.6	58.7	2767	3446	36	1.02(9)
	Fe O_h	6	55.2	49.4	3047	2440	36	0.97(8)
CoFe_Zn0.30	Fe T_d	6	52.7	59.1	2777	3493	36	1.07(9)
	Fe O_h	6	54.1	48.1	2927	2314	36	1.00(8)
CoFe_Zn0.46	Fe T_d	6	52.3	59.1	2735	3493	36	1.15(9)
	Fe O_h	6	53.8	47.7	2894	2275	36	1.01(8)
CoFe_Zn0.53	Fe T_d	6	52.2	58.9	2725	3469	36	1.13(9)
	Fe O_h	6	53.6	47.8	2873	2285	36	0.97(8)

Néel model, which accounts for the existence of two independent magnetic sublattices in spinel ferrites, can be applied also to calculate the theoretical M_s values for the zinc-substituted samples by considering the cationic distribution obtained by the Mössbauer data and assuming that the zinc ions occupy tetrahedral sites. The theoretical values are 139 emu/g, 154 emu/g and 162 emu/g for zinc contents of 0.30, 0.46 and 0.53. The values are near the experimental ones with the exception for the sample with the highest zinc content, in which probably part of the zinc is in the octahedral sites. Thanks to the multitechnique approach used to characterise the sample, it is possible to reconstruct the cationic distribution in the CoFe_Zn0.53 sample by means of the experimental M_s values obtained by DC magnetometry, the iron ions occupancies found by Mössbauer Spectroscopy and the total content of cobalt measured by ICP-OES (**Tab. 4.6.6**). The obtained cationic distribution indicates the necessity for a 30-40% of zinc ions to occupy octahedral sites in order to justify the observed saturation magnetisation values.

Tab. 4.6.6 Cationic distribution obtained for the CoFe_Zn0.53 sample by means of the experimental M_s values obtained by DC magnetometry, the iron ions occupancies found by Mössbauer Spectroscopy and the total content of cobalt measured by ICP-OES. The first raw refers to M_{s1} value whereas the second raw refers to M_{s2} value, obtained by means of the equations $M = M_{s1} + b\frac{1}{H}$ and $M = M_{s2} \cdot \left(1 - \frac{a}{H} - \frac{b}{H^2}\right)$, respectively.(Morrish, 1965).

Tetrahedral sites			Octahedral sites			M_s emu/g)
Zn	Co	Fe	Zn	Co	Fe	
0.30	0.28	0.42	**0.23**	0.19	1.58	131
0.36	0.22	0.42	**0.17**	0.25	1.58	140

4.6.2   Room Temperature magnetic properties and SAR measurements.

Since an increase of Ms with zinc substitution (within a certain zinc content range) has been observed at 5 K, we studied the magnetic behaviour at 300 K in order to verify the suitability of these samples for biomedical applications, in particular for Magnetic Fluid Hyperthermia.

M vs H curves (**Fig. 4.6.10**) display a superparamagnetic behaviour at 300 K (i.e. zero remnant magnetisation and zero coercivity) with high M_s values for all the samples. Values near the one reported in the literature for bulk-CoFe$_2$O$_4$ (90÷80 emu/g) (Cullity and Graham, 2009; Smit and Wijn, 1959) but higher than the values reported in the literature for nanoparticles of similar sizes (Joshi et al., 2009; Peddis et al., 2011; Song and Zhang, 2004) have been obtained for the cobalt ferrite (CoFe_Zn0) and the sample with the lowest zinc content (CoFe_Zn0.30) (**Tab. 4.6.7**). This induces to believe that surface disorder phenomena (i.e spin-canting) can be considered negligible in these samples in agreement with the Mössbauer results and as already observed in literature(Batlle et al., 2011; Roca et al., 2009). Higher content of zinc produces a decrease of the saturation magnetisation at room temperature. In the case of ordered magnetic systems, the thermal behaviour of the magnetization is related to the presence of low energy collective excitations (i.e. spin waves or magnons)(Hasegawa and Ray, 2014), depending on particle size and on the chemical composition of the materials(Demortière et al., 2011; Lo et al., 2011). In the samples under investigation, the increasing of diamagnetic ion content leads to a different temperature dependence of magnetization, justifying the different M_s *vs zinc content* at 300 K and 5 K.
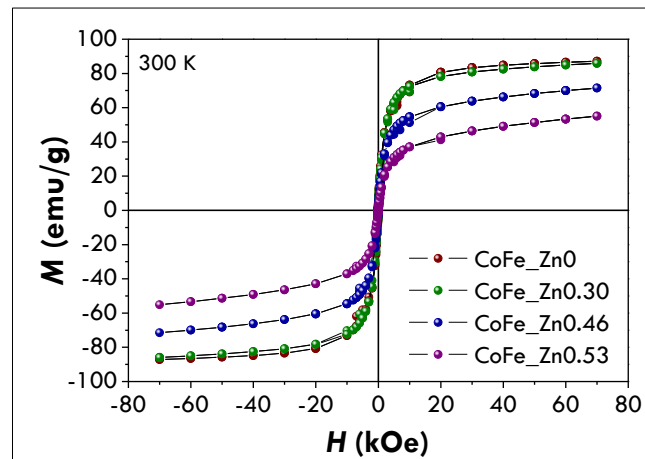
Fig. 4.6.10 Field dependence of the magnetisation at 300 K for CoFe_Znx (with x=0, 0.30, 0.46, 0.53) samples.

Tab. 4.6.7 Room temperature properties of CoFe_Znx (with x=0, 0.30, 0.46, 0.53) samples: M_{7T} is the value of the magnetisation extracted at 7 T; M_{s1} and M_{s2} are saturation magnetisation values estimated by the equations $M = M_{s1} + b\frac{1}{H}$ and $M = M_{s2} \cdot \left(1 - \frac{a}{H} - \frac{b}{H^2}\right)$, respectively.(Morrish, 1965)

Sample	M_{7T} (emu/g)	M_{s1} (emu/g)	M_{s2} (emu/g)
CoFe_Zn0	87±2	90±2	92±2
CoFe_Zn0.30	86±2	90±2	94±2
CoFe_Zn0.46	72±2	78±2	84±2
CoFe_Zn0.53	55±1	63±1	70±2

Due to the high saturation magnetisation values and also driven by the idea of a possible suitability of Zn-substituted cobalt ferrite as less toxic heat mediators, we tested the hyperthermal efficiency of all the

samples by recording heating curves (**Fig. 4.6.11**) under a magnetic field of 183 kHz and 17 kA/m. Indeed, the hydrophobic nanoparticles were converted in hydrophilic by intercalation process with cetyltrimethylammonium bromide (CTAB, $(C_{16}H_{33})N(CH_3)_3Br$). The concentration of the colloidal dispersion was 3.4 mg/ml for all the samples.
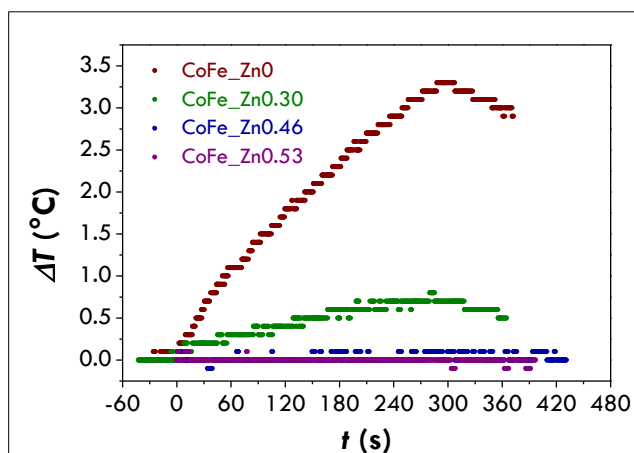
Fig. 4.6.11 Heating curves obtained on water colloidal dispersions of the CoFe_Znx (with x=0, 0.30, 0.46, 0.53) samples at 25 °C and under a magnetic field of f=183 kHz and H_0=17 kA/m.

Only the samples CoFe_Zn0 and CoFe_Zn0.30 characterised by the highest saturation magnetisation values are responsible for a heat release but not in the same extent. In order to quantify the amount of heat released, the SAR has been calculated by the initial slope method and values equal to 19±3 and 6±2 W/g_{ox}, respectively, have been obtained (**Tab. 4.6.8**).

Tab. 4.6.8 Specific Adsorpion Rate (SAR) and Intrinsic Loss Power (ILP) values for the samples CoFe_Zn0 and CoFe_Zn0.30 (25 °C, 183 kHz, 17 kA/m) together with the saturation magnetisation values (M_{s1}, M_{s2}). SAR and ILP values are normalised for the total mass of ferrite (W/g_{ox}, $nH \cdot m^2/kg_{ox}$) or for the metal mass (W/g_{Me}, $nH \cdot m^2/kg_{ox}$).

Sample	M_{s1} (emu/g)	M_{s2} (emu/g)	SAR (W/g_{ox})	SAR (W/g_{Me})	ILP_{ox} ($nH \cdot m^2/kg_{ox}$)	ILP_{Me} ($nH \cdot m^2/kg_{ox}$)
CoFe_Zn0	90±2	92±2	19±3	26±4	0.36±0.05	0.49±0.07
CoFe_Zn0.30	90±2	94±2	6±2	8±2	0.11±0.03	0.15±0.05

A comparison with the literature data is not trivial because of the different procedures adopted to measure the heating curves, as, for instance, different frequencies and amplitudes of the external magnetic field. With this regard, in order to compare heating abilities obtained by different frequencies and amplitudes, Pankhurst *et al.* proposed to use a parameter named Intrinsic Loss Power (ILP)(Kallumadil et al., 2009) expressed in $[nH \cdot m^2/kg]$, defined as follows:

$$ILP = \frac{SAR}{f \cdot H_0{}^2}$$

Eq. 4.6.3

where SAR is expressed in W/kg, f in kHz and H_0 in kA/m.

The ILP value calculated for CoFe_Zn0 sample is 0.36 ± 0.05 nH·m²/kg. This value is comparable with those obtained by other authors for cobalt ferrite of similar particle size(Lee et al., 2011) or similar crystallite size(Fantechi et al., 2015). Higher ILP values have been reported in the literature for bigger particles(Lee et al., 2011; Mazario et al., 2013; Nappini et al., 2015), for cobalt substituted iron oxide particles(Fantechi et al., 2015; Kita et al., 2010) or for cobalt doped magnetosomes chains(Alphandéry et al., 2011). Unfortunately, ILP is not a sufficient tool to overcome all the difficulties in the comparison of SAR values obtained by different groups. First, its application is restricted to the linear response theory, i.e. to superparamagnetic nanoparticles, and the validity field is limited to frequency values of up to several MHz. Secondly, the comparison should concern SAR values obtained by similar experimental set-up with similar environmental thermodynamic losses. However, this is a quite challenging condition to achieve. Indeed, the difficulty in the comparison among the SAR values concerns other aspects that ILP parameter does not deal with, as differences in the experimental set-up adopted to measure the heating curve (adiabatic or non-adiabatic), in the solvents and in the analytical models adopted to determine the SAR values (initial slope method, Box-Lucas method, etc...). In addition, the comparison among literature data becomes even more difficult if we consider that often a complete chemical-physical characterisation of the systems in terms of crystallite size, crystallinity degree, particle size and size distribution, type and amount of capping agent, etc. is lacking.

In this context, to demonstrate the complexity of the SAR estimation, the samples have been characterised also by another experimental setup, the 'MACH' system (Resonant Circuits Ltd, UK) located at the UCL Healthcare Biomagnetic and Nanomaterials Laboratories. This discussion is addressed in the paragraph 4.6.3.

The difference in the efficiency between CoFe_Zn0 and CoFe_Zn0.30 is considerable despite of the similarities in terms of saturation magnetisation, particle size, particle size distribution, crystallite size, and capping agent amount. It thus can be explained with the different anisotropy. Indeed, the 5 K magnetic measurements have shown for the cobalt ferrite sample higher coercivity and saturation fields than the Zn-substituted one. To confirm this idea further measurements have been carried out.

To further investigate the magnetic behaviour of these two samples, the temperature dependence of the magnetisation has been studied by means of the Zero Field Cooled and Field Cooled protocols (ZFC-FC) (**Fig. 4.6.12**). The values of T_{max}, T_{irr} and T_b have been calculated and are listed in The values of T_{max}, T_{irr} and T_b have been calculated and are listed in **Tab. 4.6.9**. Both T_{max} and T_b have been found to decrease when the zinc ions replace the cobalt ones in the spinel structure suggesting a decrease in the anisotropy or a decrease in the magnetic interactions extent, being the volume of the particles similar. In addition, the energy barrier distributions are found to become less and less broad with increasing zinc content, suggesting a higher homogeneity of the nanoparticles in the sample, probably in terms of cationic distribution due to the strong preference of zinc for tetrahedral coordination.

Tab. 4.6.9. ZFC curves exhibit a maximum at a temperature (T_{max}) that, for non-interacting particles, is directly proportional to the average blocking temperature, with a proportionality constant of β=1-2,(Gittleman et al., 1974) depending on the type of particle size distribution. An irreversible magnetic behavior is observed below a given temperature (T_{irr}) that is related to the blocking of the biggest particles(Peddis et al., 2013). T_{irr} was calculated by considering a 3% of difference between the M_{FC} and the M_{ZFC}
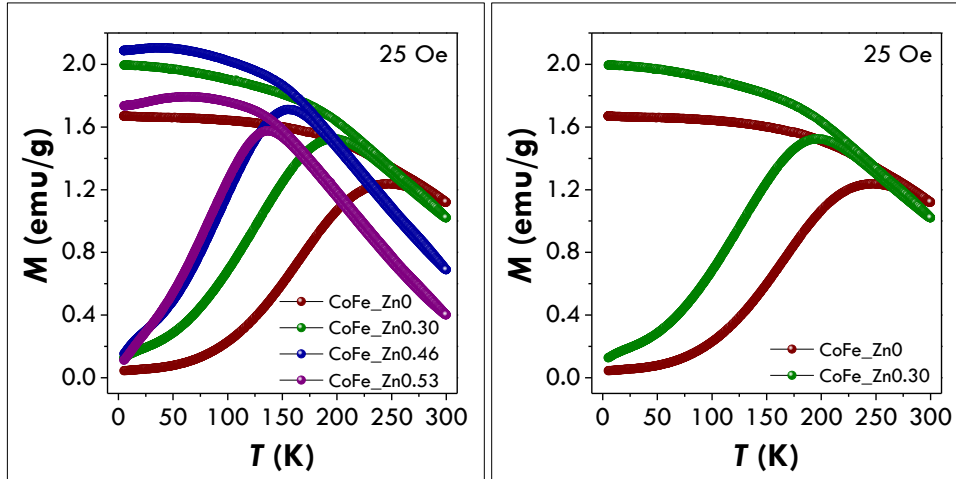
Fig. 4.6.12 Temperature dependence of the magnetisation obtained under 25 Oe by Zero Field Cooled – Field Cooled protocols for the CoFe_Znx (with x=0, 0.30, 0.46, 0.53) samples.

The difference ($M_{FC} - M_{ZFC}$), can be considered as a good approximation of M_{TRM}(R.W. Chantrell et al., 1991; Del Bianco et al., 2002), being M_{IRM} negligible in nanoparticle systems

$$MTRM\ (H,T,t)\ =\ MFC\ (H,T,t)\ -\ MZFC\ (H,T,t)\ +\ MIRM\ (\ H,T,t)$$

Eq. 4.6.4

The first derivative $d(M_{FC} - M_{ZFC})/dT$ gives an estimate of the anisotropy energy barrier distribution:

$$f(\Delta Ea) \propto -\frac{dM_{ZFC-ZFC}}{dT}$$

Eq. 4.6.5

T_b is the blocking temperature calculated by means of the first derivative of the difference curve (M_{FC}-M_{ZFC}) as the temperature at which the 50% of the nanoparticles are in the superparamagnetic state.(Peddis et al., 2013, 2012) We can obtain an estimate of the blocking temperature from the distribution of the magnetic anisotropy energy barriers by evaluating the temperature at which 50% of the particles overcome their anisotropy energy barriers.

The anisotropy energy barrier distributions for the CoFe_Znx samples are shown in **Fig. 4.6.13**.
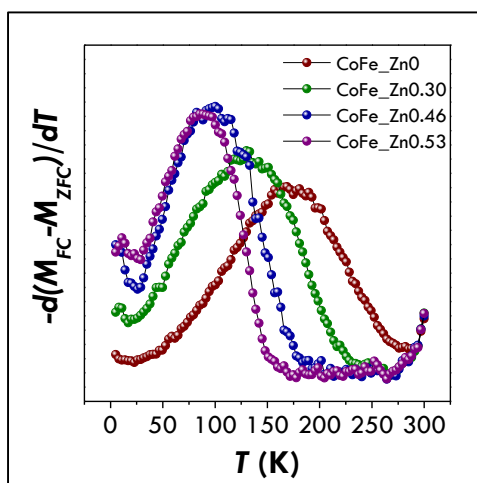
Fig. 4.6.13 Anisotropy energy barrier distributions for the CoFe_Znx (with x=0, 0.30, 0.46, 0.53) samples estimated by the first derivative $d(M_{FC} - M_{ZFC})/dT$.

The values of T_{max}, T_{irr} and T_b have been calculated and are listed in **Tab. 4.6.9**. Both T_{max} and T_b have been found to decrease when the zinc ions replace the cobalt ones in the spinel structure suggesting a decrease in the anisotropy or a decrease in the magnetic interactions extent, being the volume of the particles similar. In addition, the energy barrier distributions are found to become less and less broad with increasing zinc content, suggesting a higher homogeneity of the nanoparticles in the sample, probably in terms of cationic distribution due to the strong preference of zinc for tetrahedral coordination.

Tab. 4.6.9 Values of T_{max}, T_{irr} and T_b for the CoFe_Znx (with x=0, 0.30, 0.46, 0.53) samples.

Sample	T$_{max}$ (K)	T$_{irr}$ (K)	T$_b$ (K)
CoFe_Zn0	247±12	272±14	174±9
CoFe_Zn0.30	197±10	219±26	120±6
CoFe_Zn0.46	156±8	175±26	92±5
CoFe_Zn0.53	137±7	147±27	86±4

The results of DC magnetometry show that the samples CoFe_Zn0 and CoFe_Zn0.30 are characterised by different anisotropy. However, this technique appear to be not sufficient to explain the different heating ability of the samples. Indeed, we should consider that (i) the DC magnetometry is characterised by a time scale in the range 10-100 seconds; (ii) the relative extent of the measurement and relaxation time scales is critical to make the particles exhibit superparamagnetism rather than quasi-static properties.

Therefore, one may hypothesise that the magnetic characterisation by techniques with other timescales, as [57]Fe Mössbauer Spectroscopy and AC magnetometry, can be useful to understand the physical reasons of the different hyperthermal efficiency in different samples.

In order to confirm this idea, Mössbauer spectra at room temperature have been recorded (**Fig. 4.6.14, Fig. 4.6.15, Tab. 4.6.10**).
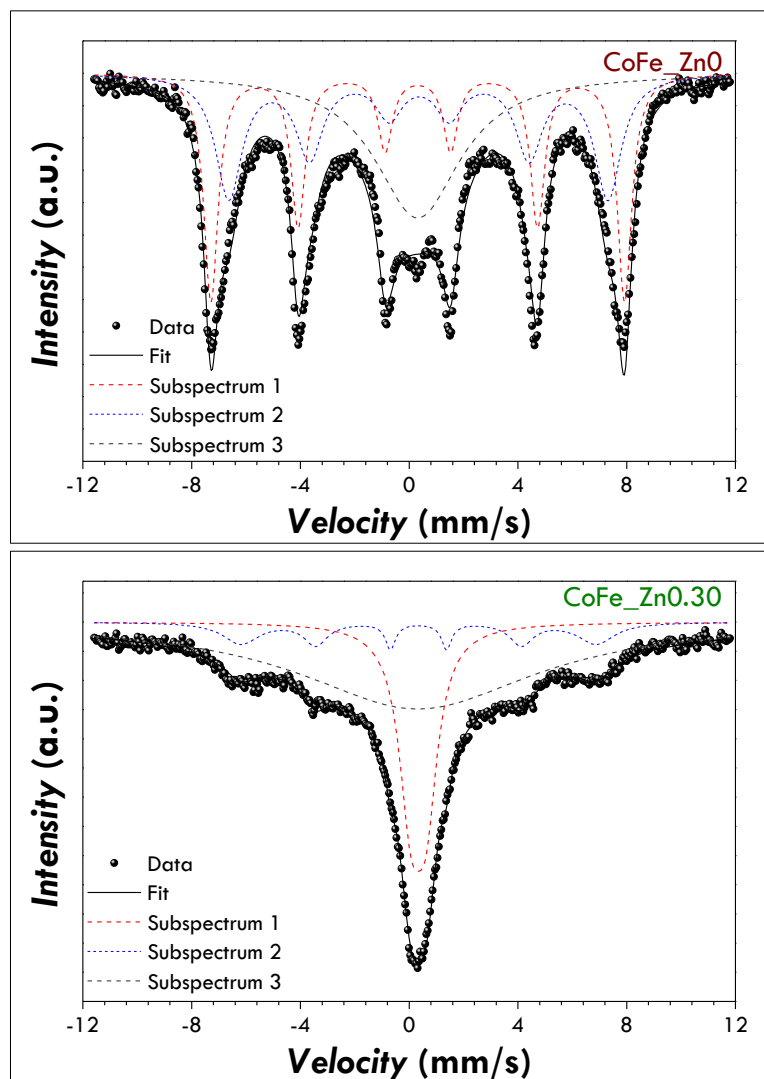
Fig. 4.6.14 Room Temperature Mössbauer spectra of the CoFe_Zn0 (*upper panel*) and CoFeZn_0.30 (*bottom panel*) samples.
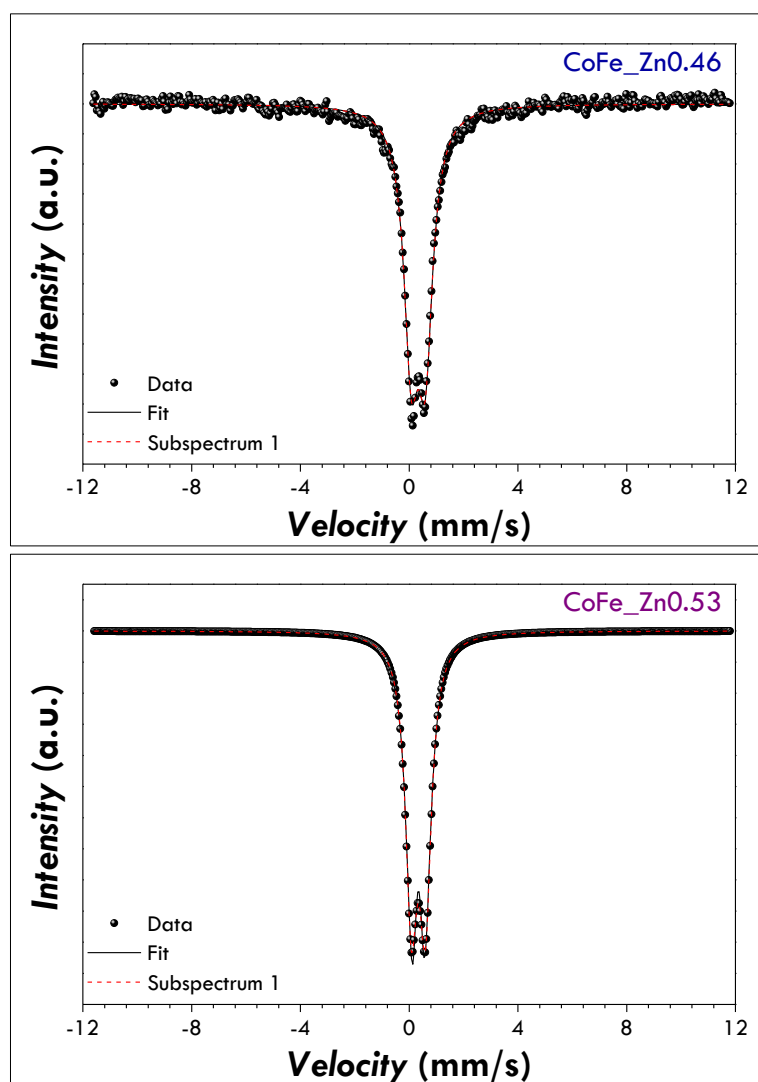
Fig. 4.6.15 Room Temperature Mössbauer spectra of the CoFe_Zn0.46 (*upper panel*) and CoFeZn_0.53 (*bottom panel*) samples.

Tab. 4.6.10 Room Temperature Mössbauer parameters of the CoFe_Znx (with x=0, 0.30, 0.46, 0.53) samples: isomer shift (δ), quadrupole splitting (ΔE_Q), hyperfine field (B_Hf) and Full-Width at Half-Maximum (FWHM). Last column lists the interpretation for each subspectrum.

Sample	Subsp.	δ (mm/s)	ΔE_Q (mm/s)	B_Hf (T)	FWHM (mm/s)	Interpretation
CoFe_Zn0	1	0.36	-0.03	43.3	1.19	Fe in the blocked state
	2	0.32	0.00	47.2	0.64	Fe in the blocked state
	3	0.32	0.00	-	3.84	Fe in the unblocked state
CoFe_Zn0.30	1	0.34	-0.56	-	1.05	Fe in the unblocked state
	2	0.34	0	40.6	0.23	Fe in the blocked state
	3	0.33	-	-	10.61	Fe in the unblocked state
CoFe_Zn0.46	1	0.34	0.52	-	0.66	Fe in the unblocked state
CoFe_Zn0.53	1	0.34	0.51	-	0.52	Fe in the unblocked state

Both the spectra of CoFe_Zn0 and CoFe_Zn0.30 can be fitted by means of a superposition of sextet and singlet. The isomer shift values suggest only the presence of Fe^{3+} (**Tab. 4.6.10**). The sextets account for the blocked spinel ferrite nanoparticles, the broad singlet (subspectrum 3 in the CoFe_Zn0 spectrum) for the particles characterised by a relaxation time close to the measurement time scale and the sharper singlet (e.g. subspectrum 1 in the CoFe_Zn0.30 spectrum) for superparamagnetic nanoparticles. In agreement with the hypothesised scenario, the cobalt ferrite sample shows a higher area of the sextets than the Zn-substituted sample suggesting that it contains a higher percentage of blocked nanoparticles.

In this view, AC magnetometry has been used to measure the temperature dependence of the in-phase (χ') and out-of-phase (χ'') components of the magnetic susceptibility at different frequencies (1-1000 Hz) for both the samples (**Fig. 4.6.16**). From these data, the Néel relaxation time, τ_N, has been estimated at 300 K for both the samples by using the Vogel-Fulcher model (**Fig. 4.6.17**):

$$\tau_N = \tau_0 exp\left(\frac{E_b}{T - T_0}\right)$$

Eq. 4.6.6

where τ_0 is the characteristic relaxation time, E_b is the energy barrier against the magnetisation reversal, T is the absolute temperature and T_0 is the temperature value accounting for the strength of magnetic interactions. Values of τ_N of $3.8 \ 10^{-6}$ s and $2.8 \ 10^{-9}$ s have been obtained for the CoFe_Zn0 and CoFe_Zn0.30 samples, respectively (**Tab. 4.6.11**).
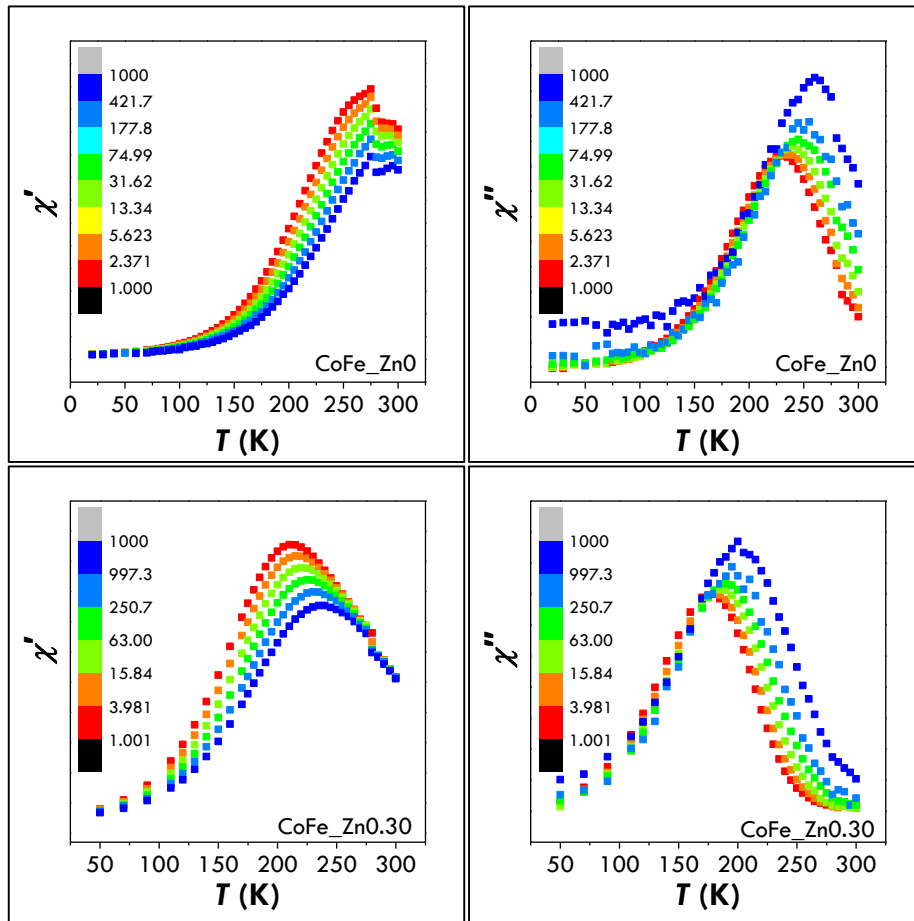
Fig. 4.6.16 AC susceptibility measurements. In phase (χ') and out of phase (χ") components measured at 1 (red curve), 4, 16, 63, 251 and 997 Hz (blue curve) as a function of temperature for the samples CoFe_Zn0 (upper panels) and CoFe_Zn0.30 (bottom panels).
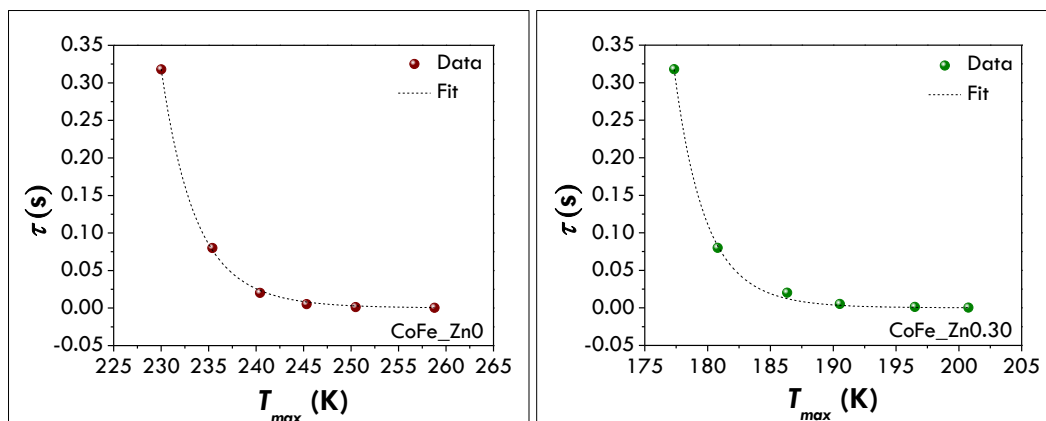
Fig. 4.6.17 Curve fitting for the estimate Néel relaxation time at 300 K, τ$_N$, by the Vogel-Fulcher model $\tau_N = \tau_0 exp\left(\frac{E_b}{T-T_0}\right)$, where τ_0 is the characteristic relaxation time, E_b is the energy barrier against the magnetisation reversal, T is the absolute temperature and T_0 is the temperature value accounting for the strength of magnetic interactions.

Tab. 4.6.11 Parameters obtained from the curve fitting by the Vogel-Fulcher model $\tau_N = \tau_0 exp\left(\frac{E_b}{T-T_0}\right)$, for T=300 K. τ_0 is the characteristic relaxation time, E_b is the energy barrier against the magnetisation reversal, T_0 is the temperature value accounting for the strength of magnetic interactions.

Sample	τ_0 (s)	E_b(K)	T_0 (K)	τ_N (s)
CoFe_Zn0	$4.8\ 10^{-13}$	2672.2	131.8	$3.8\ 10^{-6}$
CoFe_Zn0.30	$4.8\ 10^{-14}$	2142.0	104.8	$2.8\ 10^{-9}$

Beside Néel relaxation, also Brownian motion may concur to the heat release of superparamagnetic nanoparticles. Therefore, in order to verify the aggregation extent in the conditions used to measure hyperthermic properties and to determine the Brown relaxation time, τ_B, Dynamic Light Scattering (DLS) analyses have been carried out on water colloidal dispersions of CoFe_Zn0 and CoFe_Zn30 at 25°C. **Fig. 4.6.18** reports the distribution curves related to the number of entities (percentage) as a function of their diameter, expressed in nm. The distributions have been fitted using a *Log Normal* function. The two curves appear very similar, being almost overlapping. These results exclude the possibility that the different hyperthermal abilities of the two samples are related to different aggregation extent. In **Tab. 4.6.12** the mean values and the standard deviations are listed for both samples. In both the cases, the minimum in the curve is around 15 nm, which is the diameter that can be associated to a single magnetic nanoparticle capped by a monolayer of oleate molecules intercalated with CTAB. This value is in agreement with the literature data about oleate-capped nanoparticles of similar size and with the theoretical value expected for nanoparticles with an inorganic core of ~7.5 nm, an oleate shell thickness of ~2 nm and a second shell of CTAB intercalated among the hydrophobhic chains of the oleate molecules (2-3 nm) (Lim et al., 2013). The predominant species for both the samples are the ones with an hydrodynamic diameter of about 30 nm, which could be probably ascribed to small aggregates of 2-3 particles.
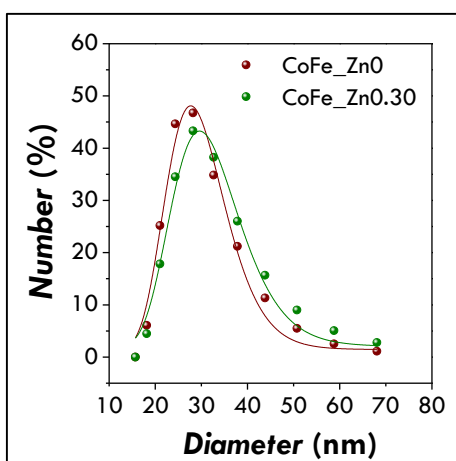
Fig. 4.6.18 Distribution of the hydrodynamic diameter obtained by Dynamic Light Scattering analyses for CoFe_Zn0 and CoFe_Zn30 water colloidal dispersions (~3.4 mg/mL) at 25°C.

Tab. 4.6.12 Mean <D_H> values and corresponding standard deviations obtained by Dynamic Light Scattering analyses for CoFe_Zn0 and CoFe_Zn30 sample.

Sample	<D_H> (nm)	Stand. Deviation (nm)	Stand. Deviation (%)
CoFe_Zn0	29.2	7.0	24
CoFe_Zn30	31.5	8.2	26

The mean hydrodynamic diameters, 29.2 and 31.5 nm, result in τ_B values of $8.5 \cdot 10^{-6}$ s and $1.1 \cdot 10^{-5}$ s for CoFe_Zn0 and CoFe_Zn0.30 samples, respectively. It arises that τ_N and τ_B for CoFe_Zn0 are of the same magnitude order, suggesting that both the mechanisms contribute to the effective relaxation time (**Tab. 4.6.13**). These estimates are nicely confirmed by the behaviour of the ac susceptibility at the melting point of the solutions (**Fig. 4.6.16**) where the Brownian mechanism begins. It should be also highlighted that Hergt *et al.*(Hergt et al., 2010) indicated 7 nm as the critical diameter at which $\tau_N = \tau_B$ for cobalt ferrite nanoparticles dispersed in water, indeed a size similar to that of the sample CoFe_Zn0 (~7.5 nm). On the contrary, in the case of CoFe_Zn0.30, τ_B is four orders of magnitude slower than τ_N, and thus its contribution is negligible. The maximum heating efficiency will be reached when the time of the faster relaxation process matches the characteristic time of the SAR measurement, $\tau_{SAR} = 1/2\pi f = 8.7 \cdot 10 - 7$ s. Therefore, cobalt ferrite nanoparticles (CoFe_Zn0), with $\tau_{eff} = (1/\tau_N + 1/\tau_B)^{-1} = 2.6 \cdot 10^{-6}$ s, must be more efficient than the Zn-substituted sample ($\tau_{eff} = 2.8 \cdot 10^{-9}$ s).

Tab. 4.6.13 Néel and Brown relaxation times characteristic fot the CoFe_Zn0 and CoFe_Zn0.30 samples.

Sample	SAR (W/g_{ox})	SAR (W/g_{Me})	τ_N (s)	τ_B (s)
CoFe_Zn0	19±3	26±4	$3.8 \ 10^{-6}$	$9.2 \cdot 10^{-6}$
CoFe_Zn0.30	6±2	8±2	$2.8 \ 10^{-9}$	$5.3 \cdot 10^{-6}$

4.6.3 Limits in the evaluation of the heating ability

As mentioned in the paragraph 4.6.2, the heating ability of the CoFe_Znx have been studied by a second experimental apparatus, the 'MACH' system (Resonant Circuits Ltd, UK) located at the UCL Healthcare Biomagnetic and Nanomaterials Laboratories in London.

In order to point out how different experimental conditions may affect the final SAR values, the curves (**Fig. 4.6.19**) have been recorded directly on hexane colloidal dispersions and under an external magnetic field of H_0=14 kA/m and f=925 kHz.
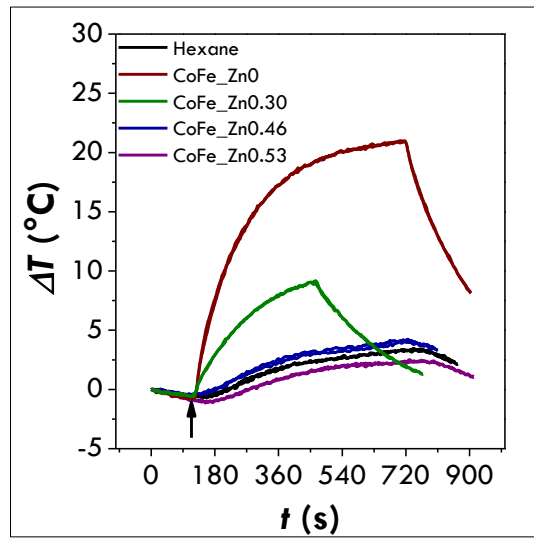
Fig. 4.6.19 Heating curves obtained on hexane colloidal dispersions of the CoFe_Znx (with x=0, 0.30, 0.46, 0.53) samples at 25 °C and under a magnetic field of f=925 kHz and H_0=14 kA/m.

The curves qualitatively show the same trend observed by means of the LA.M.M. setup (paragraph 4.6.2): the samples CoFe_Zn0.46 and CoFe_Zn0.53 are not responsible for a heat release whereas the other two samples exhibit a certain heating ability. First, it can be noted that the samples CoFe_Zn0.46 and CoFe_Zn0.53 as well as the blank sample of hexane are not characterised by a flat curve suggesting that the system is not well isolated from the environment. For the samples CoFe_Zn0 and CoFe_Zn0.30, the SAR values and the ILP values have been estimated by means of the initial slope method and are listed in **Tab. 4.6.14** and **Tab. 4.6.15**, respectively.

Tab. 4.6.14 Comparison of the SAR values obtained with two different experimental setups (LA.M.M, University of Florence; MACH Resonant Circuits Ltd, UK) on the CoFe_Zn0 and CoFe_Zn0.30 samples.

Sample	LA.M.M.		MACH	
	SAR (W/g_{ox})	SAR (W/g_{Me})	SAR (W/g_{ox})	SAR (W/g_{Me})
CoFe_Zn0	21±3	29±4	146±6	201±8
CoFe_Zn0.30	6±2	9±3	57	79

Tab. 4.6.15 Comparison of the ILP values obtained with two different experimental setups (LA.M.M, University of Florence; MACH Resonant Circuits Ltd, UK) on the CoFe_Zn0 and CoFe_Zn0.30 samples.

Sample	LA.M.M.		MACH	
	ILP_{ox} ($nH \cdot m^2/kg_{ox}$)	ILP_{Me} ($nH \cdot m^2/kg_{Me}$)	ILP_{ox} ($nH \cdot m^2/kg_{ox}$)	ILP_{Me} ($nH \cdot m^2/kg_{Me}$)
CoFe_Zn0	0.40±0.06	0.55±0.08	0.78±0.03	1.08±0.04
CoFe_Zn0.30	0.12±0.04	0.16±0.05	0.39±0.02	0.21±0.01

SAR values obtained with the MACH system are about doubled with respect to the LA.M.M. ones. This can be ascribed to the very high frequency of the magnetic field but also to the lower thermal capacity of hexane with respect to the water used with the MACH system.

4.7   Conclusions and perspectives

Four Zn-substituted $CoFe_2O_4$ samples with different zinc content, the same crystallite size, particle size and particle size distribution, and capping agent weight percentage have been *ad-hoc* prepared. This ideal premise has allowed the discussion of the magnetic properties and the heating abilities exclusively on the basis of the different chemical composition, being the other material features unchanged.

High saturation magnetisation values from 109 emu/g to 157 emu/g have been obtained at 5 K by increasing the Zn content up to 0.46. A further increase of the Zn content have resulted in a decrease of the saturation magnetisation to a value of 140 emu/g. The cationic distribution with the preferential 4-fold coordination of zinc ions has been found to justify the observed 5 K M_s *versus Zn content* trend. Two samples, $CoFe_2O_4$ and $Zn_{0.30}Co_{0.70}Fe_2O_4$, have shown also at room temperature high and similar saturation magnetisation values (~90 emu/g). Although the similarities of the samples, $CoFe_2O_4$ have shown a triple SAR value of 19 W/g. This different behaviour has been justified by studying on one hand the relaxation dynamics by combining AC magnetometry and ^{57}Fe Mössbauer Spectroscopy and on the other hand by investigating the hydrodynamic properties of the samples. It has been found that the cobalt ferrite sample has both the Néel and Brown relaxation times that matches the characteristic time of the hyperthermic measurement whereas $Zn_{0.30}Co_{0.70}Fe_2O_4$ has a faster effective relaxation time. This in the light of the linear response theory gives rise to the higher efficiency of the cobalt ferrite samples.

The study here presented demonstrates the power of a multi-technique approach on the comprehension of both the magnetic properties and the heating abilities. Moreover, the fundamental condition for such an in-depth comprehension remains the systematic study of the effect produced by only one parameter at the time and keeping the other parameters unchanged (in this case the chemical composition). This must be reached by the synthesis of ad-hoc prepared samples. Finally, this kind of studies is needed also for a proper design of the material based on a critical choice of the features to tune.

4.8   Materials and methods

4.8.1   Chemicals

Fe(III) acetylacetonate (97%),   1,2-hexadecanediol (90%),   oleic acid (90%),   dibenzylether (98%), absolute ethanol have been purchased by Sigma Aldrich.   Co(II) acetylacetonate (99%), Zn(II) acetylacetonate (99%), oleylamine (80-90%) have been purchased by Acros Organics.

4.8.2   ICP-AES

The samples were prepared for the ICP-AES analyses as follows. NPs powders were digested by using aqua regia (3:1 HCl/HNO$_3$). The digested sample solutions were heated up to ~90 °C for 1 h under magnetic stirring, then to ~200 °C for 10 minutes. The solutions were left to cool down, filtered and diluted by using 1%$_{v/v}$ HNO$_3$ solution. The ICP measurements were made by means of a Liberty 200 ICP Varian spectrometer under the following conditions: Fe line: 259.940 nm, Co line: 228.616 nm, Zn line: 213.856 nm; Fe concentration range: (0÷1.5) ppm, Co concentration range: (0÷2) ppm, Zn concentration range: (0÷1) ppm; Fe detection range: (0.015÷750) ppm, Co detection range: (0.050÷2500) ppm, Zn detection range: (0.009÷450) ppm.

4.8.3   X-Ray Diffraction (XRD)

X-Ray Diffraction (XRD) patterns were collected by using two different instrument setups. The first one is a θ-θ Bragg–Brentano focalizing geometry Seifert X 3000 diffraction system equipped with a Cu Kα source (λ=1.54056 Å), a graphite monochromator on the diffracted beam and a scintillation counter. Crystalline phases were identified by means of Analyze software. The second one is a PANalytical X'Pert PRO powder X-ray diffraction system equipped with a Co Kα source (λ=1.78901 Å) and an X'Celerator detector. Phase identification was carried out by means of the X'Pert accompanying software program PANalytical High Score Plus. The mean crystallite size,

$< D_{XRD} >$, was obtained by Scherrer's equation:

$$< D_{XRD} >= \frac{K \cdot \lambda}{\beta \cdot cos\theta}$$

where, K is a constant related both to the crystallite shape and to the definition of both β and $< D_{XRD} >$, λ is the wavelength of the X-rays, β is the half-maximum line breadth of the peak occurring at 2θ. Here, K is assumed equal to 0.9, whereas β is defined by the Warren's correction, $\beta = \sqrt{\beta_{exp}^2 - \beta_{std}^2}$, where β_{exp} is the experimental breadth of the peak and β_{std} is the instrumental one estimated by means of the pattern of a standard obtained under the same experimental conditions.

$< D_{XRD} >$ was calculated as a mean value by fitting, through Origin Software, the most intense X-ray peaks ((220), (311), (400), (422), (511), (440)) with the *PseudoVoigt* function, by using a 1:1 gaussian:lorentzian ratio ($m_u = 0.5$):

$$y = y_0 + A \left[m_u \frac{2}{\pi} \frac{w}{4(x - x_c)^2 + w^2} + (1 - m_u) \frac{\sqrt{4 \, ln \, 2}}{\sqrt{\pi} w} e^{-\frac{4 \, ln \, 2}{w^2}(x - x_c)^2} \right]$$

Refinement of the structural parameters was performed by the Rietveld method using the MAUD software(Lutterotti and Scardi, 1990) adopting recommended fitting procedures(Young and Wiles, 1982). Structural models of the identified phases were obtained by Inorganic Crystal Structure Database (ICSD, Karlsruhe, Germany).

4.8.4 Transmission Electron Microscopy (TEM)

The samples were prepared for the TEM analysis as follows. The hexane colloidal dispersion was submitted to an ultrasonic bath. Then, a quote was sampled and diluted with hexane. The diluted dispersion was then dropped on a carbon-coated copper grid and left to dry for the TEM observations. The nanoparticles were observed in electron micrographs obtained with two different instruments. The first one is a TEM (JEOL JEM-1200 EX II) operating at 120 kV. The second microscope is a JEM 2010 UHR equipped with a Gatan imaging filter (GIF) with a 15 eV window and a 794 slow scan CCD camera. The mean particle size, $< D_{TEM} >$, was obtained by measuring the average diameter of 350 particles using images collected in different parts of the grid. The polydispersity index (σ_{TEM} (%)) has been evaluated as the ratio between the standard deviation and the average particle size. The images were analysed by PEBBLES software(Mondini et al., 2012) in a semi-automatic mode combined with a manual mode (in order to add, to the population, those particles not directly recognised by the software) and by adopting ellipsoidal shape. The nanoparticles size distribution were fitted through Origin Software using the *LogNormal* function:

$$y = y_0 + \frac{A}{\sqrt{2\pi}wx} e^{\frac{-\left[ln\frac{x}{x_c}\right]^2}{2w^2}}$$

4.8.5 Fourier Transform – Infrared Spectroscopy (FT-IR)

FT-IR spectra were recorded in the region from 400 to 4000 cm^{-1} by using a Bruker Equinox 55 spectrophotometer on KBr-dispersed sample pellets.

4.8.6 ThermoGravimetric Analysis (TGA)

TGA curves were obtained on powders by using a Mettler-Toledo TGA/SDTA 851 in the (25÷1000) °C range, with a heating rate of 10 °C/min under 50 mL/min argon flow. In addition, another TGA curve was recorded on the CoFe_Zn0.53 sample under 50 mL/min oxygen flow.

4.8.7 DC magnetometry

Magnetic properties were studied by means of a Quantum Design MPMS SQUID VSM (H_{max} = 70 kOe). Different kind of magnetic measurements were carried out. Magnetisation versus magnetic field curves were measured at 5 K and 300 K between -70 kOe and +70 kOe. The saturation magnetisation (M_s) was estimated by using two different approaches and the corresponding values were denoted as M_{s1} and M_{s2}. M_{s1} was obtained by fitting the M vs 1/H curve by the equation

$$M = \boldsymbol{M_{s1}} + b\frac{1}{H}$$

for 1/H tending to 0.

M_{s2} was obtained by the equation

$$M = \boldsymbol{M_{s2}} \cdot \left(1 - \frac{a}{H} - \frac{b}{H^2}\right)$$

for H tending to ∞.(Morrish, 1965)

Magnetisation versus temperature measurements were performed using Zero-Field-Cooled (ZFC), Field-Cooled (FC). ZFC and FC magnetisation measurements were carried out by cooling the sample from room temperature to 5 K in zero magnetic field; then, a static magnetic field of 25 Oe was applied. M_{ZFC} was measured during the warmup from 5 K to 300 K, whereas M_{FC} was recorded during the subsequent cooling. The difference $(M_{FC} - M_{ZFC})$, being a good approximation of the ThermoRemanent Magnetisation M_{TRM}(R.W. Chantrell et al., 1991; Del Bianco et al., 2002) can be used to describe the energy profile on the basis of the relation:

$$f(\Delta E_a) \propto \frac{dM_{TRM}}{dT}$$

From these data, the characteristics temperatures T_{max}, T_{irr} and T_b were obtained as follows. T_{max} is the temperature of the maximum in the Zero Field Cooled curve. T_{irr} was calculated by considering a 3% of difference between the M_{FC} and the M_{ZFC}. T_b is the blocking temperature, i.e. the temperature at which the 50% of the nanoparticles are in the superparamagnetic state and was calculated by means of the first derivative of the difference curve (M_{FC}-M_{ZFC}) as the temperature at which 50% of the particles overcome their anisotropy energy barriers.

4.8.8   AC magnetometry

AC susceptibility measurements were performed on the water colloidal dispersion of the nanoparticles (used for the measurements of the heating curves, described in 4.8.10) by a Quantum Design MPMS SQUID dedicated insert, at 5 log-spaced exciting frequencies (1, 4, 16, 63, 251 and 997 Hz) and in the temperature range 10-300K, in the absence of a static magnetic field.

4.8.9   [57]Fe Mössbauer Spectroscopy

The [57]Fe Mössbauer spectra were measured in the transmission mode with [57]Co diffused into a Rh matrix as the source moving with constant acceleration. The spectrometer (Wissel) was calibrated by means of a standard α–Fe foil and the isomer shift was expressed with respect to this standard at 293 K. The samples were measured at 4 K under zero magnetic field. In order to get information on the distribution of the iron ions between the tetrahedral and octahedral sites of the spinel structure, in field-spectra has been recorded at 4 K under 6 T in the perpendicular arrangement of the magnetic field vector with respect to the γ-beam. The fitting of the spectra was performed with the help of the NORMOS program using Lorentzian profiles.

The [57]Fe Mössbauer spectra were measured in the transmission mode with [57]Co diffused into a Rh matrix as the source moving with constant acceleration. The spectrometer (Wissel) was calibrated by means of a standard α–Fe foil and the isomer shift was expressed with respect to this standard at 293 K. The samples were measured

at 293 K under zero magnetic field. The fitting of the spectra was performed with the help of the NORMOS program using Lorentzian profiles.

4.8.10 Specific Absorption Rate (SAR) measurements

Calorimetric measurements of Specific Absorption Rate (SAR) were performed by means of a non-adiabatic experimental set-up built at the LAboratorio di Magnetismo Molecolare (LA.M.M) by means of a power supply CELESs MP6/400 (FIVES CELES), a water-cooled heating station connected to the power supply and an induction coil. Heating curves were recorded under a magnetic field of 17 kA/m and 183 kHz for 300 s on water colloidal dispersions of the magnetic nanoparticles. Indeed, the hydrophobic nanoparticles have been converted in hydrophilic ones by intercalation process with cetyltrimethylammonium bromide (CTAB, $(C_{16}H_{33})N(CH_3)_3Br$). The concentration of the colloidal dispersion was 3.5-4.0 mg/ml for all the samples. During the measurements, the sample was surrounded by polystyrene and hosted in a glass Dewar, equipped by an ethylene glycol thermostat, to ensure the proper thermal isolation. The temperature of the sample was monitored by an optical fiber probe (OPTOCON-FOTEMP) dipped into the solution by whereas a second probe was used to monitor the temperature of the internal wall of the glass dewar. The SAR values were estimated by a linear curve fitting in the first 20 s (initial slope method) of at least three heating curves for each sample.

4.8.11 Dynamic Light Scattering (DLS)

Dynamic light scattering (DLS) measurements were performed with a Malvern Instrument Zeta Zetasizer Ver 7.03 equipped with a He-Ne laser (λ= 633 nm, max 5mW) and operated at a scattering angle of 173°. All measurements were realized using a value of Material RI=2.4.2 and Dispersant RI=1.330. In all analyses, 1mL of particle suspensions was placed in a 12 mm X 12 mm polystyrene cuvette.

5   CoFe₂O₄@MⁱⁱFe₂O₄ core@shell architectures: synthesis, microstructure and hyperthermic properties

Abstract

The studies of cobalt ferrite nanoparticles as heat mediators often suffer of a strong critic related to its toxicity. However, the source of anisotropy that the cobalt ions bring can be useful to suitably modulate the Néel relaxation time of the systems. Moreover, recently two papers have highlighted the possibility to improve the hyperthermal efficiency by exploiting the coupling phenomena between hard and soft phases.

In this view, this chapter is dedicated to the study of CoFe₂O₄@MⁱⁱFe₂O₄ architectures, where MⁱⁱFe₂O₄ is magnetite/maghemite or manganese ferrite. In principle, these coating shells could on one hand confine the toxic core and on the other hand induce magnetic coupling phenomena. Two different cobalt ferrite nanoparticles of different sizes have been synthesised by hydrothermal hydrolysis of mixed cobalt-iron oleates. Two core@shell samples were produced by a seed-mediated growth process on each core. All the characterisation techniques used (XRD, TEM & HRTEM, FTIR, Mössbauer Spectroscopy) suggest the effective production of core@shell systems. The calorimetric measurements conducted to estimate the SAR revealed an improved efficiency for all the core@shell samples with respect to the corresponding core. Preliminary magnetic measurements conducted on two samples can be interpreted coherently in the light of the hypothesised scenario, suggesting the production of spring magnet systems, due to the high soft-phase volume fraction.

Core:
$CoFe_2O_4$

Biocompatible shell:
- $Fe_3O_4/\gamma\text{-}Fe_2O_3$
- $MnFe_2O_4$

Coating of the core (core@shell structures)
- Reducing the toxicity of the core
- Exploiting exchange coupling phenomena between ferrimagnetic phases
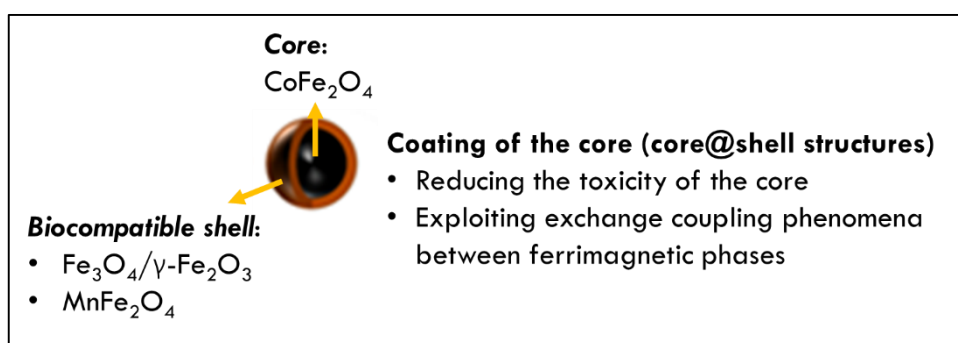
5.1 Introduction

A great variety of synthetic strategies has been proposed in the literature to create magnetic inorganic core@shell nanoparticles. Most of them are chemical approaches, due to their greater versatility in modulating sizes, particle size distributions and shapes if compared with the physical ones. Among them the simplest one is based on a surface treatment (e.g., oxidation, reduction) of the nanoparticle (core) to induce the formation of a shell of a different phase, while the others are based on a seed mediated growth approach.

This method is extremely appealing since it allows to create diverse heteroarchitectures depending of the composition, the structure and cell parameters of the two phases. Preformed nanoparticles are used as seeds for the controlled heterogeneous nucleation of the shell. In comparison with the surface treatment approach, this method allows a better control of the shell during the synthesis in terms of thickness, homogeneity and crystallinity. Co-precipitation, high temperature thermal decomposition of metallorganic precursors, microemulsions and sol- gel routes have been proposed in the literature to exploit the versatility of the seed-mediated approach.

However, some other methods that uses sonochemical and microwave irradiation processes, can also be found in the literature even if specific for a given system.(López-Ortega et al., 2015a)

In this chapter, an alternative synthetic strategy based on solvothermal processes is proposed for the creation of spinel ferrite-spinel ferrite core-shell architectures. Solvothermal syntheses can be commonly defined as all those strategies based on chemical processes performed in a closed vessel (autoclave) above ambient temperature and pressure.[1,2] Under specific pressure (typically between 1 and 10,000 atm) and temperature (typically between 100 °C and 1000 °C) the interaction of precursors during the synthesis is highly facilitated.[3] If water is used as the solvent, the method is called "hydrothermal synthesis". The nature of the reagents and solvents, as well as temperature and pressure, are key parameters for the synthesis of inorganic materials. For a long time used for bulk materials, solvothermal and hydrothermal approaches have recently become more and more appealing due to the possibility to synthetize nanosized materials with well-defined size and morphology by means of suitable surfactants in non-aqueous(D'Arienzo et al., 2011; Dinh et al., 2009; Tian et al., 2011) or in water-alcohol media.(Repko et al., 2013, 2011; Wang et al., 2005) The growing interest for these strategies derives from the lower toxicity and the lower cost of the solvents that can be employed, when compared to those commonly used in widely diffused surfactant-assisted non-aqueous hot injection(de Mello Donegá et al., 2005; Hessel et al., 2011; Kwon and Hyeon, 2008a; Murray et al., 1993; Pan et al., 2008; Riha et al., 2009) and heating-up processes.(Hyeon et al., 2001; Kwon and Hyeon, 2008b; Park et al., 2007, 2000; Sun et al., 2004) Other advantages include the possibility to use moderate reaction temperatures, the low boiling point of the solvents and the high repeatability of the synthesis. These advantages render solvothermal processes promising low cost, eco-friendly and reliable strategies for the synthesis of inorganic nanostructures.(Cara et al., 2015)

5.2 Core: hydrothermal preparation of colloidal CoFe$_2$O$_4$ nanoparticles.

Two samples of CoFe$_2$O$_4$ nanoparticles of different sizes, labelled as Co1, Co2, were prepared by hydrothermal hydrolysis of mixed cobalt-iron oleates in a mixture of water and organic solvents with different polarities. The first step of the preparation is the synthesis of metal oleates through a Liquid Solid Solution (LSS) process (**Fig. 5.2.1**).(Wang et al., 2005)
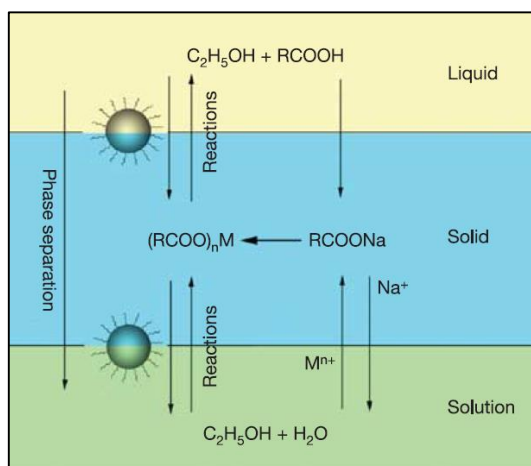
Fig. 5.2.1 Scheme of liquid-solid-solution (LSS) phase transfer synthetic strategy.(Wang et al., 2005)

5.2.1 First step: synthesis of Me^{II}-Fe^{III} oleate in 1-pentanol.

The mixed Me^{II}-Fe^{III} oleates (Me^{II}= Co^{2+}, Mn^{2+}) and the Fe^{II}-oleate were used as metal precursors for the synthesis of CoFe$_2$O$_4$ or MnFe$_2$O$_4$ and γ-Fe$_2$O$_3$, respectively. They were synthetized and isolated following the procedure set up by A. Repko *et al.*(Repko et al., 2015) The molar ratios among the reactants are given in **Tab. 5.2.1** for the different metal oleates. First, a pale yellow sodium oleate solution was prepared in a 250 mL round-bottom flask dissolving sodium hydroxide in 10 mL of distilled water and adding 20 mL of ethanol together with the oleic acid. Secondly, the iron(III) nitrate and Me(II) nitrate (Me^{II}= Co^{2+}, Mn^{2+}) or only iron(II) chloride were dissolved in 10 mL of distilled water producing an orange solution and added to the sodium oleate one and stirred in order to obtain the Me^{II}-Fe^{III} oleate or the Fe^{II}-oleate. After the addition, the formation of the metals oleate complexes made the solution black and viscous. The successive addition of 20 mL of hexane led to a liquid biphasic system, the upper one is the metals oleate containing organic phase while the lower is the water phase. This mixture was boiled under reflux for 60 min to complete the formation of metals oleate. The as-described procedure was carried out under an inert atmosphere in the case of the Fe^{II} oleate synthesis. Then, the system was left to cool down to room temperature. The water phase was removed by Pasteur pipette, while 20 mL of water, 5 mL of ethanol and 5 mL of hexane were added to the organic phase and stirred in order to wash it from the inorganic residuals. The mixture was boiled under reflux for 30 min. This washing step was done twice. Finally, the water phase was completely removed and 15 mL of 1-pentanol were added to the flask. The mixture was heated for about 30 min to induce the complete evaporation of hexane. The obtained product as a viscous black liquid (Me^{II}-Fe^{III} oleate or Fe^{II} oleate in pentanol) was moved to a 40 mL glass vial

with Teflon cup with the help of 5 mL of 1-pentanol. The composition of the product, i.e. the final amount of pentanol and consequently the concentration of metals oleate was estimated from its weight, assuming quantitative yield from metals salts:

$$3Na(oleate) + Fe(NO_3)_3 \rightarrow Fe(oleate)_3 + 3NaNO_3$$

$$2Na(oleate) + Co(NO_3)_2 \rightarrow Co(oleate)_2 + 2NaNO_3$$

$$2Na(oleate) + Mn(NO_3)_2 \rightarrow Mn(oleate)_2 + 2NaNO_3$$

$$2Na(oleate) + FeCl_2 \rightarrow Fe(oleate)_2 + 2NaCl$$
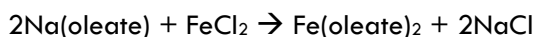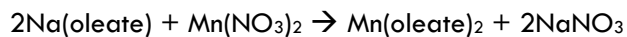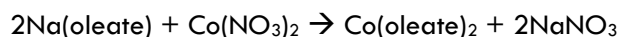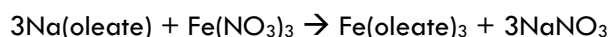
Tab. 5.2.1 Summary of the experimental conditions used for the synthesis of the metals-oleates.

Metals Oleate	Inorganic salts	Oleic acid	NaOH	Ethanol	Water	Hexane
Co^{II}-Fe^{III}	$Fe(NO_3)_3$: 16 mmol	65 mmol	66 mmol	20 mL	20 mL	20 mL
	$Co(NO_3)_2$: 8 mmol					
Mn^{II}-Fe^{III}	$Fe(NO_3)_3$: 16 mmol	65 mmol	66 mmol	20 mL	20 mL	20 mL
	$Mn(NO_3)_2$: 8 mmol					
Fe^{II}	$FeCl_2$: 24 mmol	60 mmol	54 mmol	20 mL	20 mL	20 mL

5.2.2 Second step: synthesis of $CoFe_2O_4$ nanoparticles (core)

The appropriate amount of the fresh metal oleates are added to a suitable mixture of water and organic solvents. In hydrothermal condition (**Fig. 5.2.2**), water causes the hydrolysis of the oleate and the formation of nanoparticles takes place after nucleation and growth in the organic phase until they reach a critical diameter, which bring them to precipitate. (Repko et al., 2015, 2013, 2011) At the end of the treatment, in fact, a black precipitate is found at the bottom of the Teflon liner, while two liquid phases are present above, an aqueous and an organic one. The water phase is always colourless indicating, as expected, that no particles are present in it. On the contrary, the colour of the organic phase becomes darker with decreasing solvent polarity due to the presence of hydrophobic oleate-capped nanoparticles with a size below the critical diameter necessary to precipitate. TEM analysis indicates that the nanoparticles in the organic phase are smaller with respect to the precipitated ones. In addition, un-reacted metal oleates have not been detected by FTIR in both the organic and water phases, suggesting that metal oleates completely react to produce the spinel ferrite.

The Co/Fe molar ratio, calculated by ICP measurements, have been found equal to 0.48 and 0.55 for Co1 and Co2 samples, respectively. These results demonstrate the production of almost stoichiometric cobalt ferrite nanoparticles by means of this hydrothermal method, in agreement with previous results from Repko *et al.*(Repko et al., 2015).

Fig. 5.2.2 Steel autoclave and teflon liner used for hydrothermal synthesis.

The appropriate amount of Co-Fe oleates (in a 1:2 Co:Fe ratio to produce $CoFe_2O_4$) in 1-pentanol was moved into a 50 mL Teflon liner and a further amount of a mixture of other solvents was added to reach a total volume of 20 mL, as described in **Tab. 5.2.2**. Then, 10 or 5 mL of water, depending on the reaction temperature, was added. The solvents and their relative ratios have been chosen according to the study by Repko *et al.*(Repko et al., 2015) in order to prepare particles of different sizes. The liner free space was flushed with nitrogen and was enclosed in a stainless steel autoclave (Berghof DAB-2), briefly shaken and put vertically into a pre-heated (180° or 220 °C) oven. The reaction time was 10 hours. After the heat treatment, the autoclave was left to cool down to room temperature, and the as-prepared magnetic nanoparticles were magnetically separated from the supernatant that was discarded. A purification process was conducted twice as follows. First, the particles were dispersed in 10 mL of hexane (with the help of sonication), then 10 mL of ethanol were used in order to wash and precipitate the nanoparticles that were finally separated by magnet. At the end of this step, the nanoparticles were dispersed in 5 mL of hexane and centrifuged at 3000 rpm for 5 min. In this case the supernatant, which is the desired product, was recovered and the precipitate was discarded. The nanoparticles concentration was estimated by sampling an aliquot of the colloidal dispersion, drying it and weighing it out. A summary of the synthesis conditions for each sample is reported in **Tab. 5.2.2**. It is worthy of note that both the solvent polarity (by using 1-octanol or toluene together with 1-pentanol) and the reaction temperature (180 °C or 220 °C) play the role in the nanoparticles growth and their final size. The hexane dispersions were stable for several months.

Tab. 5.2.2 Summary of the experimental conditions used for the synthesis of cobalt ferrite nanoparticles (Co1, Co2, Co_R) and manganese ferrite nanoparticles (Mn_R). The solvents are indicated by the following labels: P for 1-pentanol, O for 1-octanol, T for toluene and W for distilled water.

Sample	n Oleate (mmol)[a]	P (mL)	O (mL)	T (mL)	W (mL)	Temperature	Reaction time
Co1	6	20	-	-	10	180 °C	10h
Co2	6	10	10	-	5	220 °C	10h
Co_R	3	10	10	-	5	220 °C	10h
Mn_R	6	10	-	10	5	220 °C	10h

[a]referred to Co^{II}-Fe^{III} oleates

5.2.3 Reference sample: physical mixture.

A reference sample (CoMn_R) made up of $CoFe_2O_4$-$MnFe_2O_4$ physical mixture (weight ratio 1:1) was prepared. Both the phases were synthesised as described in the previous paragraph about the cores and the synthesis conditions are shown in **Tab. 5.2.2**. Specifically, a proper amount of hexane $CoFe_2O_4$ nanoparticles (Co_R) dispersion was added to the $MnFe_2O_4$ (Mn_R) suspension, dried and characterized.

5.3 Preparation of core-shell nanoparticles.

The Co1 and Co2 nanoparticles were used as seeds to produce core@shell nanostructures by means of a second hydrothermal treatment (seed-mediated growth). In particular, for both Co1 and Co2 two core@shell samples were prepared with a shell of maghemite/magnetite and manganese ferrite, labelled as Cox@Fe and Cox@Mn (where x=1, 2), respectively.

Different attempts have been carried out in order to achieve the best experimental conditions, in terms of ratio seeds/shell precursor, solvent, concentration of the precursors, allowing the production of bigger nanoparticles with a narrow size distribution. For example, we found out that 1-octanol is not a suitable solvent because it leads to a high polydispersity index of the product. This can be probably ascribed to the low colloidal stability of the seed nanoparticles dispersion. Being toluene a good solvent to disperse nanoparticles, it has been chosen instead of 1-octanol.

The amount of hexane dispersion containing the appropriate quantity of particles (seeds) was added in a Teflon liner. The particles were precipitated by adding ethanol in a 1:1 volume ratio with respect to the hexane dispersion, held by a magnet and the liquid was discharged. Then, the particles were dissolved in 10 mL of toluene (with the help of sonication) and 10 mL of a 1-pentanol solution of metals oleate was added. Finally, after the addition of 5 mL of distilled water, the liner was enclosed into the autoclave and treated at 220°C for 10 hours. After the heat treatment, the purification steps were the same as for the seeds. **Tab. 5.3.1**summarises the synthesis conditions for the core@shell nanostructures.

Tab. 5.3.1 Summary of the experimental conditions used for the synthesis of core@shell (Co1@Mn, Co1@Fe, Co2@Mn, Co2@Fe).

Sample	Seeds (mg)	n Oleate (mmol)^a	1-pentanol (mL)	Toluene (mL)	Distilled water (mL)	Temperature	Reaction time
Co1@Mn	105	1.34	10	10	5	220 °C	10h
Co1@Fe	50	2.5	10	10	5	220 °C	10h
Co2@Mn	50	1.5	10	10	5	220 °C	10h
Co2@Fe	50	2	10	10	5	220 °C	10h

^{a}referred to Mn^{II}-Fe^{III} oleates (Co1@Mn; Co2@Mn) or Fe^{II} oleate (Co1@Fe; Co2@Fe)

5.4 Composition, microstructure and morphology

5.4.1 X-Ray Diffraction (XRD)

XRD patterns of the cores as well as the core@shell systems (**Fig. 5.4.1**) show the typical reflections of a spinel oxide phase.
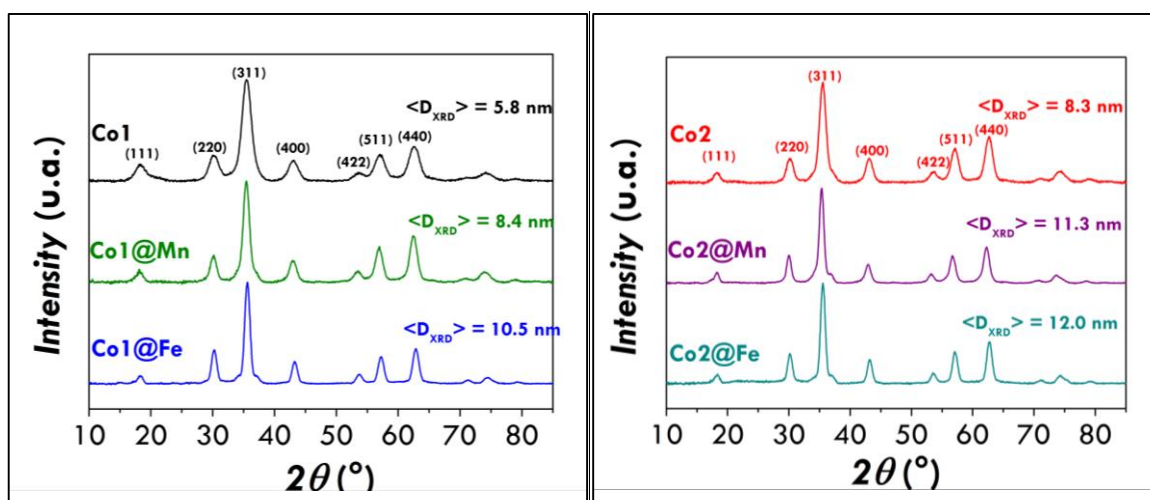
Fig. 5.4.1 XRD patterns of the Co1 (*left panel*) and Co2 (*right panel*) samples and the corresponding core@shell systems.

The cell parameters, *a*, for the Co1 and Co2 have been found equal to 8.405±0.001 Å and 8.397±0.001 Å respectively (**Tab. 5.4.1**), in good agreement with the value for the $CoFe_2O_4$ (8.3919 Å, PDF Card: 022-1086). From the profile analysis, the crystallite sizes have been estimated and are reported in **Tab. 5.4.1**. The crystallite sizes of the samples Co1 and Co2 are equal to 5.8±0.2 nm and 8.3±0.1 nm.

A slight variation of the lattice parameter has been observed for all core@shell systems. An increase of the lattice parameter is observed in the case of Co1@Mn and Co2@Mn, according to the higher cell parameter for manganese ferrite (8.4990 Å, PDF Card: 010-0319). Inversely, a decrease of the lattice parameter is detected when the shell is made of maghemite (8.3515 Å, PDF Card: 391346) or magnetite (8.3960 Å, PDF

Card: 19-0629) that are isostructural. The core@shell samples of both Co1 and Co2 are characterised by an increased crystallite size (see **Tab. 5.4.1**), suggesting that a growth process took place.

Tab. 5.4.1 Summary of the microstructural (lattice parameter, crystallite size) morphological (particle size) properties and percentage of the inorganic phase obtained by ThermoGravimetric Analysis of the Co1 and Co2 samples and the corresponding core@shell systems. In addition, the lattice parameters and the crystallite sizes for the samples Co_R and Mn_R used to prepare the physical mixture CoMn_R are listed.

Sample	a (Å)	$<D_{XRD}>$ (nm)	$<D_{TEM}>$ (nm)	σ_{TEM} (%)	Inorganic phase
Co1	8.405±0.001	5.8±0.2	5.4±0.9	16.7	73%
Co1@Mn	8.417±0.001	8.4±0.3	9.4±1.0	10.6	84%
Co1@Fe	8.375±0.001	10.8±0.3	10.5±1.3	12.3	88%
Co2	8.397±0.001	8.3±0.3	8.5±1.2	14.1	80%
Co2@Mn	8.440±0.001	11.3±0.8	14.3±1.6	11.2	92%
Co2@Fe	8.388±0.001	12.0±0.4	12.1±1.6	13.2	90%
Co_R	8.394±0.001	8.7±0.3	-	-	-
Mn_R	8.499±0.001	8.7±0.5	-	-	-
CoMn_R	8.438±0.001	8.0±0.4	-	-	-

5.4.2 Transmission Electron Microscopy (TEM, HRTEM)

The TEM Bright Field images show well-separated spheroidal nanoparticles with particle size similar to the crystallite size, suggesting a high crystallinity of the particles (**Tab. 5.4.1**). TEM images of the core@shell samples, reported in **Fig. 5.4.2**, show spherical particles with the presence of a monomodal particle size distribution, with higher mean particle size values and lower polydispersity index (σ_{TEM}%) with respect to the original core (**Fig. 5.4.3**). The absence of a bimodal distribution and the occurrence of a size-regularization process with the increase of the crystallite and particle sizes suggest that the second ferritic phase did not grow up separately or along one specific face of the core but around the pre-formed seeds, forming a core-shell architecture.
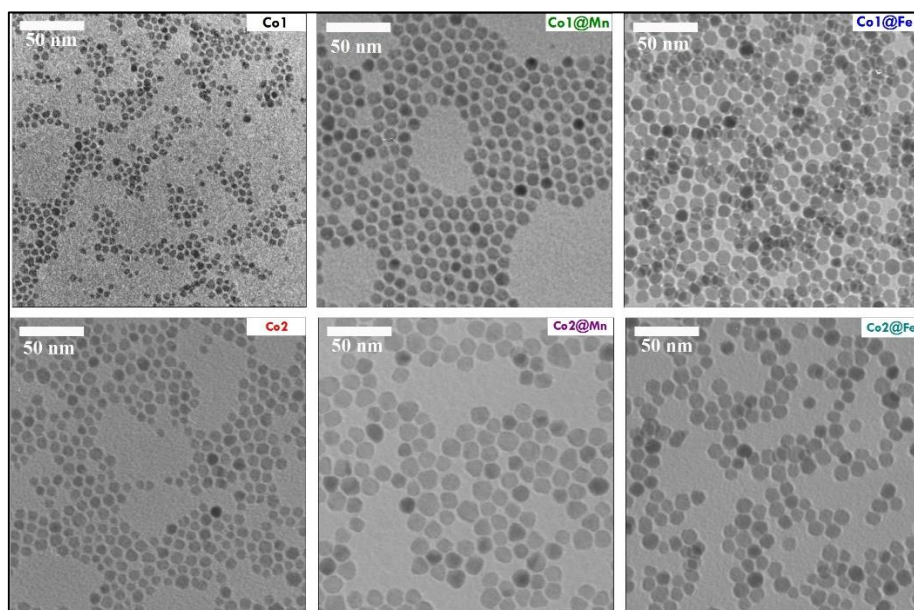
Fig. 5.4.2 TEM images of the Co1 and Co2 samples and the corresponding core@shell systems.
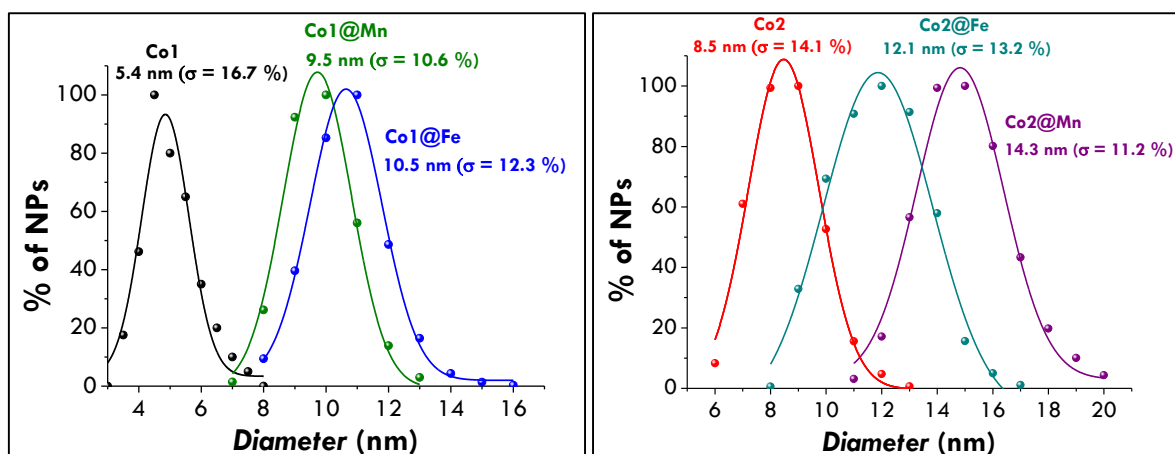
Fig. 5.4.3 Particle size distribution of the Co1 and Co2 samples and the corresponding core@shell systems.

HRTEM analysis (**Fig. 5.4.4**) on the core-shell particles allows to confirm this picture showing for all the core-shell systems, as for the cores, continuous atomic lattice fringes in the entire spherical particle which indicate a homogeneous coating of the core being the lattice parameters of the two ferrites very similar.

No difference between the particle and crystallite sizes have been detected for both Co1@Fe and Co2@Fe samples whereas a discrepancy of 1 and 3 nm has been found for Co1@Mn and Co2@Mn, respectively. This is confirmed by the images at high resolution that show the formation of a thin disordered layer at the surface of the Co@Mn core-shell systems.
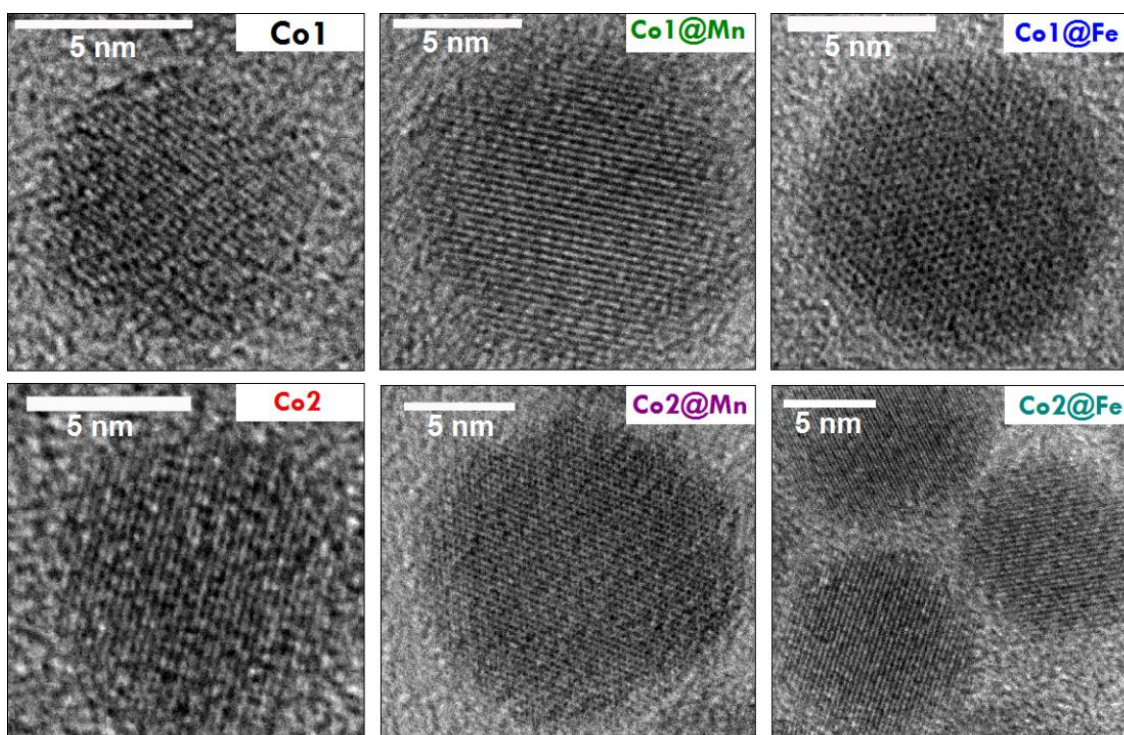
Fig. 5.4.4 HRTEM images of the Co1 and Co2 samples and the corresponding core@shell systems.

5.4.3 Inductively Coupled Plasma – Atomic Emission Spectrometry (ICP-AES)

ICP analyses have been carried out on both the pure cobalt ferrite nanoparticles and core@shell systems. The Co/Fe molar ratio for Co1 and Co2 samples have been found equal to 0.48 and 0.55, respectively, suggesting the formation of almost stoichiometric cobalt ferrite.

Taking into account the Co/Fe molar ratio found in the cores, it has been possible to calculate the amount of iron or iron and manganese in the shell. The molar ratio between the iron in the shell and the iron in the core (Fe_{shell}/Fe_{core}) is 8.91 for the sample Co1@Fe. This value corresponds to the theoretical one (8.61) calculated from the experimental particle size ($<D_{TEM}>$) considering a shell of maghemite. In the Co2@Mn sample, the Fe_{shell}/Fe_{core} molar ratio is 3.69 that matches with the theoretical one (3.61). For this coating, a ratio Mn/Fe equal to 0.45 has been obtained, which indicates an almost stoichiometric manganese ferrite.

5.4.4 Fourier Transform – Infrared Spectroscopy (FT-IR)

The capping by oleate molecules has been demonstrated by FTIR and TGA. FTIR spectra (**Fig. 5.4.5**) show the main vibrational modes associated with the oleate molecule, as the COO$^-$ vibrational modes (v_{as} (COO$^-$), v_s (COO$^-$)) and those ones related to the hydrocarbon chain. The complete assignment for all the samples is reported in **Tab. 5.4.2**. Moreover, the band at about 590 cm^{-1} can be ascribed to the Me-O stretching mode of the tetrahedral and octahedral sites of the spinel structure(Cannas et al., 2010a; White and DeAngelis, 1967) while the one at 400 cm^{-1} corresponds to the Me-O stretching only in the octahedral sites. These bands are shifted at lower wavenumbers when cobalt ferrite nanoparticles are covered with a shell of manganese

ferrite or magnetite/maghemite. Indeed, as reported in table 5, Co1@Mn and Co1@Fe present the Me-O stretching band at 580 and 586 cm^{-1} respectively, whereas Co2@Mn and Co2@Fe at 573 and 585 cm^{-1}. The shift is according with the theoretical values for manganese ferrite (550 cm^{-1}) and magnetite/maghemite (580 cm^{-1}).(Taylor, 1974; White and DeAngelis, 1967) The samples Co1@Fe and Co2@Fe show, in the region between 700-350 cm^{-1}, typical bands of maghemite, which suggest that an oxidation of Fe^{II} into Fe^{III} occurred.
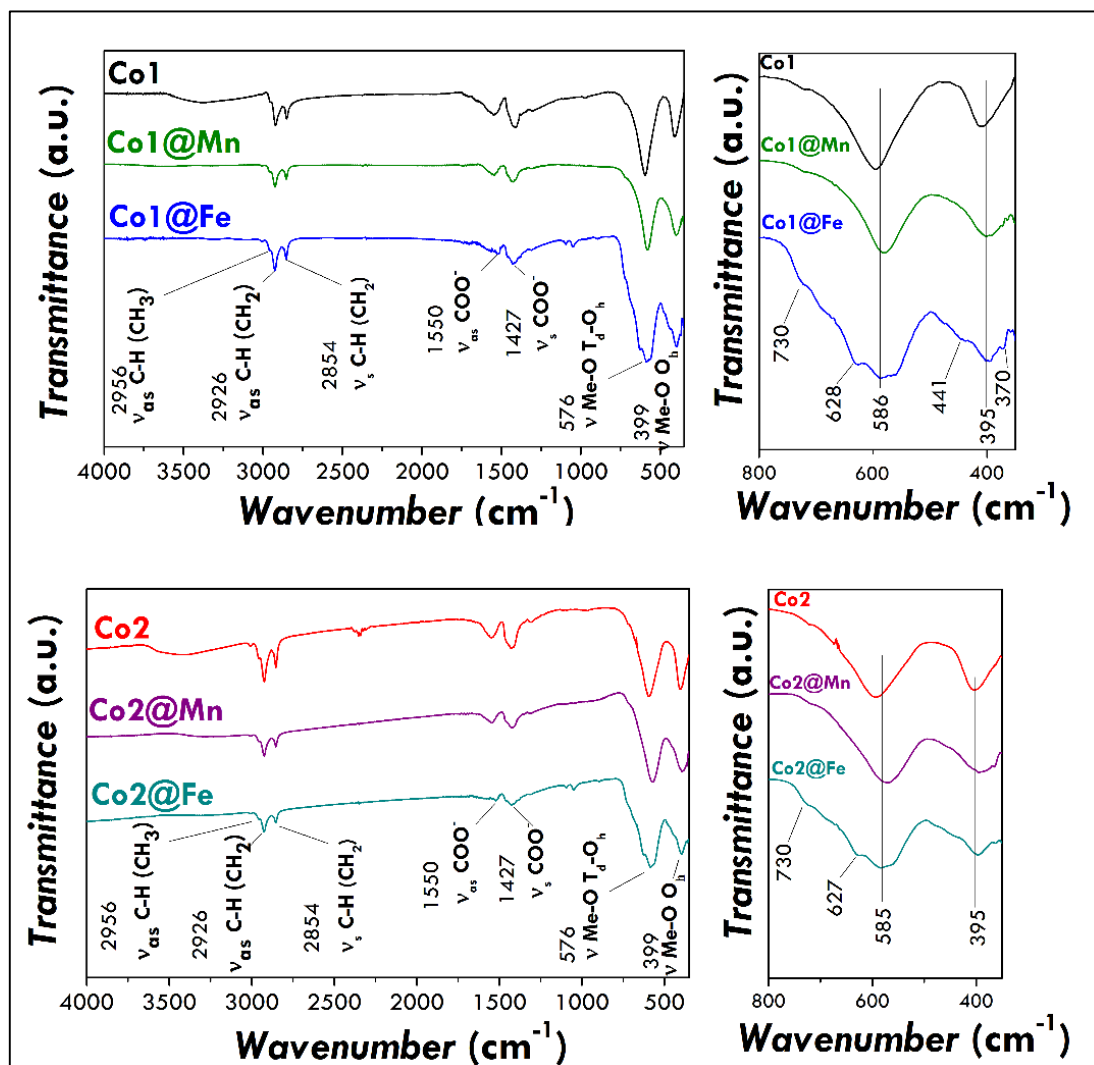
Fig. 5.4.5 Infrared spectra of the Co1 and Co2 samples and the corresponding core@shell systems recorded in the region (4000-350 cm^{-1}) (*left panel*). Infrared spectral region between 800 and 350 cm^{-1} (*right panel*).

Tab. 5.4.2 Assignments of the principal vibrational modes revealed in the FTIR spectra of the Co1 and Co2 samples and the corresponding core@shell systems.

Wavenumber (cm^{-1})						Vibration mode
Co1	Co1@Mn	Co1@Fe	Co2	Co2@Mn	Co2@Fe	
3006	3007	3008	3007	3006	3008	CH=CH stretching
2954	2957	2956	2957	2958	2958	C-H asymmetric stretching (CH$_3$)
2922	2924	2926	2924	2925	2926	C-H asymmetric stretching (CH$_2$)
2850	2854	2854	2854	2854	2854	C-H symmetric stretching (CH$_2$)
1550	1550	1550	1550	1545	1550	COO$^-$ asymmetric stretching
1417	1429	1427	1427	1425	1427	COO$^-$ symmetric stretching
-	-	1093	-	-	1095	C-O asymmetric stretching (EtOH)
-	-	1049	-	-	1051	C-O symmetric stretching (EtOH)
721	721	721	721	721		CH$_2$ wagging
-	-	688	-	-	730	Fe-O stretching
-	-	628	-	-	627	Fe-O stretching
596	580	586	594	573	585	Metal-O stretching of T$_d$ and O$_h$ sites
409	401	399	404	393	395	Metal-O stretching of O$_h$ sites

5.4.5 ThermoGravimetric Analysis (TGA)

TGA curves, recorded under an oxygen atmosphere are shown in **Fig. 5.4.6**. The weight losses percentages obtained for the samples are reported in **Tab. 5.4.1**. These weight percentages correspond to a monolayer of oleate molecules surrounding the nanoparticle surface. Indeed, for the sample Co1, considering a particle diameter of 5.4 nm (D$_{TEM}$) and a spheroidal shape for the NPs, a surface area of 92 nm^2 is obtained. A 27 % of organic capping corresponds to ~$5.8 \cdot 10^{20}$ oleate molecules. Taking into account the *bulk*-CoFe$_2$O$_4$ density of 5.3 g/cm^3 and the volume of a single spheroidal nanoparticle (82 nm^3), a 73 % of inorganic phase corresponds to a number of spinel ferrite nanoparticles of $1.7 \cdot 10^{18}$. The number of capping molecules per particle, obtained as the ratio between the number of oleate molecules and the total number of nanoparticles, is about 346 molecules/nanoparticle. Finally, the nanoparticle surface area (92 nm^2) over the number of molecules provides a surface area occupied by each oleic acid molecules of 26 Å^2/molecule. The same computation gives close values of 25 Å^2 for the sample Co2 (**Tab. 5.4.3**). These values are also really close to those ones reported by other authors for oleic acid-coated spinel iron oxides nanoparticles and suggest the presence of a close-packed monolayer of the capping agent.(Ayyappan et al., 2008; Gnanaprakash et al., 2007; van Ewijk et al., 1999)
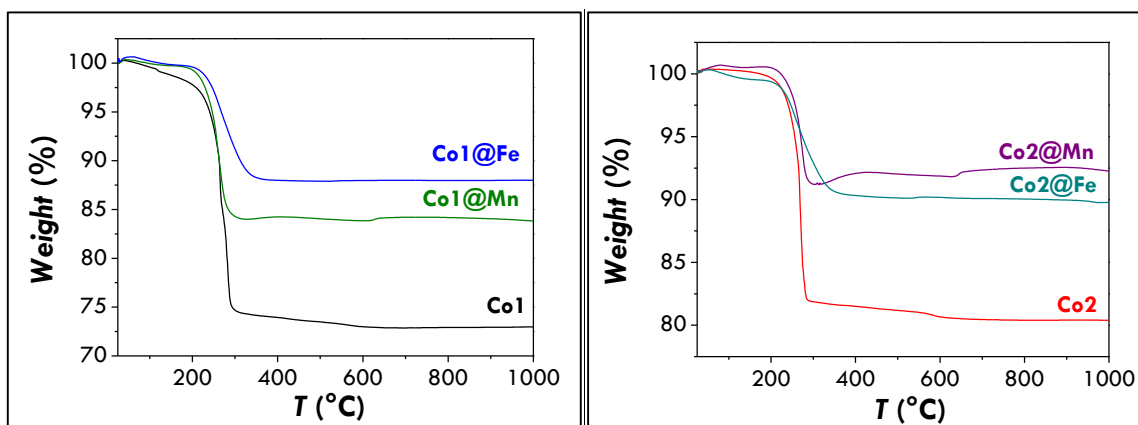
Fig. 5.4.6 TGA curves of the Co1 and Co2 samples and the corresponding core@shell systems performed under oxidative atmosphere (50 ml/min of O_2).

Tab. 5.4.3 Computation of the available area for each oleate (OA) molecule on the nanoparticle (NP) surface. The results are given in the last column (A per OA molecule). D_{TEM} is the particle diameter estimated by TEM analyses. A_{NP} is the particle surface area. V_{NP} is the volume of a nanoparticle. The mass of a single nanoparticle (calculated considering a density of 5.3 g/cm^3) is indicated as *m of a single NP*; the number of nanoparticles in one gram of sample, calculated from TGA data, is given as *# NPs per g of sample*; *mOA per g of sample* is the percentage of capping agent obtained from TGA; n_{OA} and *# OA molec. per g of sample* are the corresponding number of moles and number molecules of oleate, respectively; *# OA molec. per single NP* is the number of oleate molecules surrounding each nanoparticle.

D_{TEM} (nm)	A_{NP} (nm^2)	V_{NP} (nm^3)	m of a single NP (g)	# NPs per g of sample	mOA per g of sample	n_{OA} (mmol)	# OA molec. per g of sample	# OA molec. per single NP	A per OA molec. (Å^2)
5.4	92	82	$4.4 \cdot 10^{-19}$	$1.7 \cdot 10^{18}$	0.27	0.96	$5.8 \cdot 10^{20}$	346	26
8.5	227	322	$1.7 \cdot 10^{-18}$	$4.7 \cdot 10^{17}$	0.20	0.71	$4.3 \cdot 10^{20}$	912	25

5.5 Magnetic properties and heating abilities

Room temperature (RT) Mössbauer measurements have been carried out for all samples (**Fig. 5.5.1**) and the hyperfine parameters are shown in **Tab. 5.5.1**. The sample Co1, with crystallite size of 5.8 nm, shows a broad singlet associated with particles having a relaxation time near the Mössbauer measurement time window (τ_M) accompanied with a sharper one related to the particles in the superparamagnetic state. The spectrum of the sample Co2 with a crystallite size of 8.3 nm is fitted by one sextet deriving from the overlapping at room temperature of the two sextets accounting for Fe^{III} in the octahedral and tetrahedral sites of cobalt ferrite. Clear differences can be evidenced by the comparison of the cores with the correspondent core@shell systems: the appearance of two sextets in place of singlets indicating the formation of nanoparticles in the blocked state (Co1@Mn, Co1@Fe) and a separation of the two sextets (Co2@Mn, Co2@Fe). The two sextets can be due to two different spinel phases (CoFe$_2$O$_4$) and (MnFe$_2$O$_4$ or maghemite/magnetite) or to different sublattices (octahedral and tetrahedral sites) in a spinel phase due to the formation of a unique coherent structural domain,

99

as observed by HRTEM. The isomer shift values for the samples Co1@Mn, Co1@Fe and Co2@Mn) are in the range of Fe^{III} (0.28-0.39 mm/s), whereas Co2@Fe presents a higher isomer shift for one sextet (IS=0.50 mm/s), due to the presence of Fe^{II}, suggesting the presence of magnetite. However, the presence of maghemite cannot be completely excluded at least at the surface, as suggested by FT-IR measurements. The different behaviour with respect to the Co1@Fe, in which only Fe^{III} (maghemite) is present, is probably due to the reduced nanoparticle size that leads to a complete oxidation of magnetite to maghemite. The nature of the coating (manganese ferrite or spinel iron oxide) and the thickness of the shell (and consequently the final crystallite size) can affect the hyperfine field values. Specifically, Co1@Fe ($<D_{XRD}>$=10.8 nm) shows higher hyperfine fields for both sextets than Co1@Mn (($<D_{XRD}>$=8.4 nm). As manganese ferrite and maghemite are expected to have anisotropy constants of the same magnitude (for bulk materials: $3 \cdot 10^3$ J/m^3 and $5 \cdot 10^3$ J/m^3, respectively), the bigger crystallite size of the particles of Co1@Fe (10.8 nm) seems to be primarily responsible for the higher hyperfine field values. On the contrary, Co2@Mn ($<D_{XRD}>$=11.3 nm) and Co2@Fe ($<D_{XRD}>$=12.0 nm) have similar crystallite sizes and the increase in the hyperfine field for the sample Co2@Fe can be due principally to the higher anisotropy constant of magnetite, that for bulk material is $1.3 \cdot 10^4$ J/m^3).
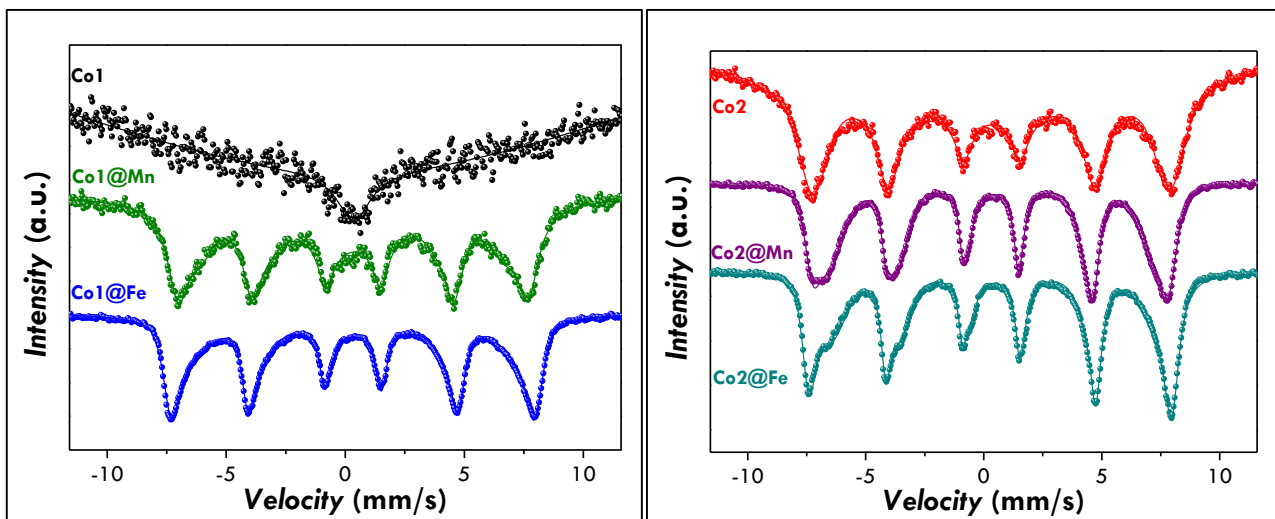
Fig. 5.5.1 Room Temperature Mössbauer spectra of the Co1 (*left panel*) and Co2 (*right panel*) samples and the corresponding core@shell systems.

Tab. 5.5.1 Room Temperature Mössbauer parameters of the spectra recorded on the Co1 and Co2 samples and the corresponding core@shell systems: isomer shift (δ), quadrupole splitting (ΔE$_Q$), hyperfine field (B$_{Hf}$) and Full-Width at Half-Maximum (FWHM).

Sample	Type	Size (nm)	Signal	δ (mm/s)	ΔE$_Q$ (mm/s)	B$_{Hf}$ (T)	FWHM (mm/s)
Co1	CoFe$_2$O$_4$	5.8±0.2	Singlet	0.2(1)	-	-	12(1)
			Singlet	0.44(6)	-	-	1.1 (2)
Co1@Mn	CoFe$_2$O$_4$@MnFe$_2$O$_4$	8.4±0.3	Sextet	0.34(2)	-0.10(1)	39.7(2)	1.56(5)
			Sextet	0.32(1)	0.00(1)	45.8(1)	0.67(2)
Co1@Fe	CoFe$_2$O$_4$@γ- Fe$_2$O$_3$/Fe$_3$O$_4$	10.8±0.4	Sextet	0.35(1)	-0.02(1)	42.4(2)	0.64(1)
			Sextet	0.32(1)	-0.01(1)	47.3(1)	0.47(1)
Co2	CoFe$_2$O$_4$	8.3±0.1	Sextet	0.32(1)	-0.02(1)	46.9(1)	0.87(2)
Co2@Mn	CoFe$_2$O$_4$@MnFe$_2$O$_4$	11.3±0.8	Sextet	0.39(1)	-0.02(1)	43.4(1)	0.55(1)
			Sextet	0.28(1)	0.01(1)	46.9(1)	0.28(1)
Co2@Fe	CoFe$_2$O$_4$@γ- Fe$_2$O$_3$/Fe$_3$O$_4$	12.0±0.4	Sextet	0.50(1)	0.00(1)	43.9(1)	0.64(1)
			Sextet	0.29(1)	-0.02(1)	47.8(1)	0.34(1)

In order to confirm the formation of a core@shell architecture was obtained, a reference sample (CoMn_R) made from a physical mixture of cobalt ferrite (Co_R) and manganese ferrite (Mn_R) nanoparticles in a mass ratio 1:1 was prepared and characterized by Mossbaur Spectrocopy at RT. The nanoparticles were synthesised by the same procedure reported in the experimental part, resulting in a crystallite size of about 8.7 nm for both Co_R and Mn_R samples, similar to the core-shell sample Co1@Mn (8.4 nm). In the physical mixture the oleate molecules that surround the particles should hinder the direct contact of the two magnetic phases. **Fig. 5.5.2** shows RT Mössbauer spectra of the pure phases (Co_R, Mn_R), the physical mixture (CoMn_R) and the core@shell nanoparticles (Co1@Mn). **Tab. 5.5.2** lists Mössbauer parameters for all these samples. The spectrum of the mixture (CoMn_R) is the sum of the two subspectra (one singlet and one sextet) having the same parameters as the pure phases. On the contrary, the spectrum of core@shell nanoparticles shows two sextets with values of hyperfine fields equal to 39.7 T and 45.8 T, which differ from the values found for pure cobalt ferrite or the physical mixture (47.3 T).
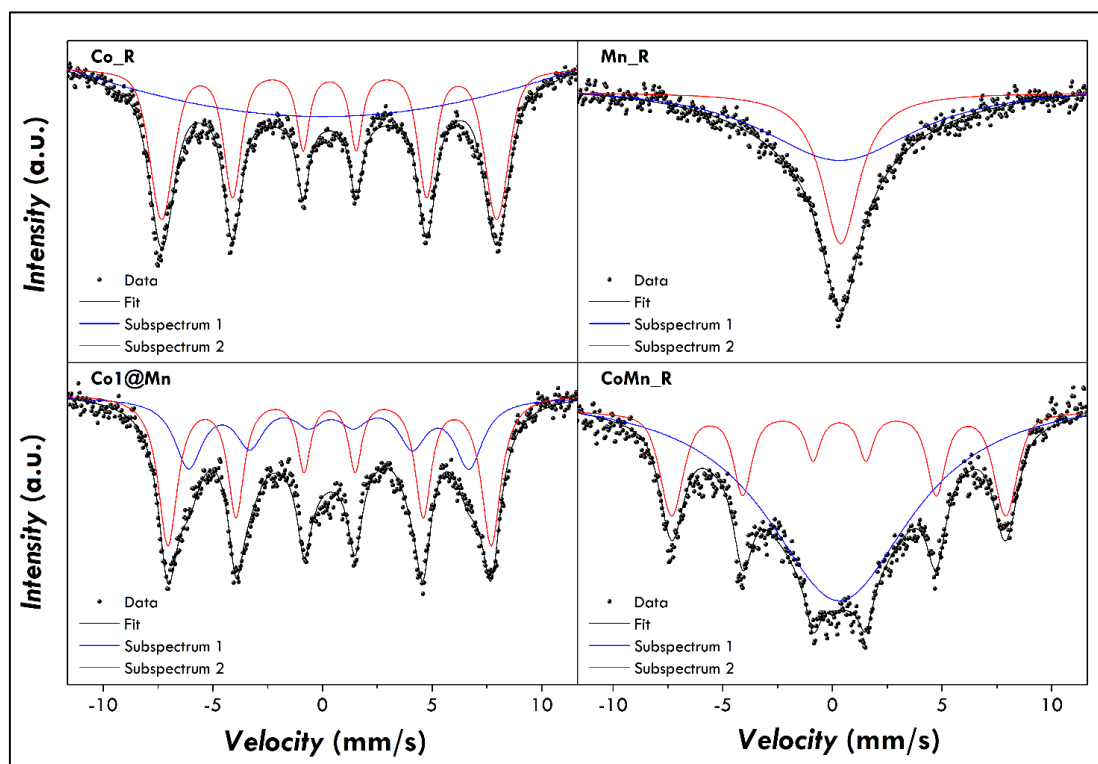
Fig. 5.5.2 Room Temperature Mössbauer spectra of the Co_R (pure cobalt ferrite nanoparticles), Mn_R (pure manganese ferrite nanoparticles) samples and the corresponding physical mixture (CoMn_R). For comparison, the RT spectrum of the sample Co1@Mn is also shown. Note that all these samples have similar crystallite size.

Tab. 5.5.2 Room Temperature Mössbauer parameters of the spectra recorded on the Co_R (pure cobalt ferrite nanoparticles), Mn_R (pure manganese ferrite nanoparticles) samples and the corresponding physical mixture (CoMn_R): isomer shift (δ), quadrupole splitting (Δ_{EQ}), hyperfine field (B_{Hf}) and Full-Width at Half-Maximum (FWHM). For comparison, the Mössbauer parameters for the sample Co1@Mn are also listed.

Sample	Type	Size (nm)	Signal	δ (mm/s)	ΔE_Q (mm/s)	B_{Hf} (T)	FWHM (mm/s)
Co_R	CoFe$_2$O$_4$	8.7±0.3	Sextet	0.32(1)	-0.02(1)	47.3(1)	0.65(2)
Mn_R	MnFe$_2$O$_4$	8.7±0.5	Singlet	0.32(6)	-	-	8(1)
			Singlet	0.38(2)	-	-	2.1(1)
CoMn_R	CoFe$_2$O$_4$ + MnFe$_2$O$_4$	8.0±0.5	Singlet	0.31(3)	-	-	8.1(1)
			Sextet	0.30(1)	-0.04(2)	47.3(1)	0.80(2)
Co1@Mn	CoFe$_2$O$_4$@MnFe$_2$O$_4$	8.4±0.3	Sextet	0.34(2)	-0.10(1)	39.7(2)	1.56(5)
			Sextet	0.32(1)	0.00(1)	45.8(1)	0.67(2)

This comparison permits to exclude the independent formation of two phases (CoFe$_2$O$_4$ and MnFe$_2$O$_4$) with similar size and can be considered as an indirect proof that in the sample Co1@Mn the two magnetic phases are in contact. This is in agreement with TEM data that evidence the formation of a monomodal distribution of

the particle size with lower polydispersity than the corresponding core for both systems(Co1 and Co2) and HRTEM that evidence a single crystal structure (**Fig. 5.5.3**).
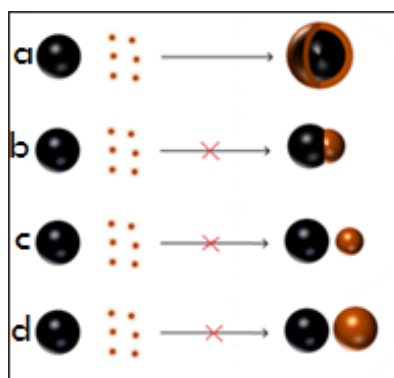
Fig. 5.5.3 Possible events of the seed-mediated growth process. (a) Core@shell architecture. (b) Heterodimer (excluded by HRTEM, formation of spherical nanoparticles). (c) Two phases with different final sizes (excluded by TEM, monomodal particle size distribution). (d) Two phases with the same final sizes (excluded by Mössbauer data on a physical mixture taken as reference sample).

Previous works(Lee et al., 2011; Noh et al., 2012) have already indicated that exchange-coupled bimagnetic ferrite-based core@shell structures can be heat mediators with improved heating abilities with respect to their single-phase counterparts. Following these promising results (although these studies were carried out by using extreme field parameters, i.e. f = 500 kHz, H_0 = 37.3 kA/m, and testing toluene colloidal dispersions), both Co1 and Co2 samples and their core@shell systems have been tested to determine the heating abilities of their water colloidal dispersions under f=183 kHz and H_0=17 kA/m. With this purpose, the hydrophobic nanoparticles were made hydrophilic by intercalation process with cetyltrimethylammonium bromide (CTAB, $(C_{16}H_{33})N(CH_3)_3Br$). The concentration of the colloidal dispersion was 3.4 mg/ml for all the samples.

Co1 sample, probably due to its small size, does not heat up. On the contrary, the sample Co2 is responsible for an increase of the temperature of about 4.5 °C in five minutes of active alternate magnetic field, leading to a SAR value of 33±3 W/g_{ox} (**Tab. 5.5.3**). This is also in agreement with the results reported in the paragraph 4.6.2 for the $CoFe_2O_4$ (CoFe_Zn0) prepared by a high temperature decomposition of metallorganic precursors showing a particle size between the two values determined for Co1 and Co2 (**Fig. 5.5.4**). The core@shell systems allow to reach higher SAR values (**Fig. 5.5.5**). In particular, even though the Co1 is not responsible for a heat release, both the manganese ferrite and maghemite-coatings led to a heating up of the solution with SAR values of 19±2 W/g_{ox} and 45±5 W/g_{ox}. A value of 51±5 W/g_{ox} is obtained for the sample Co2@Mn. These improved hyperthermal efficiencies might be coherent with formation of core-shell architecture that allow to maximise the contact between the two phases hypothesised by the multitechniques characterisation and, in particular, by the Mossbauer and TEM and HRTEM measurements.
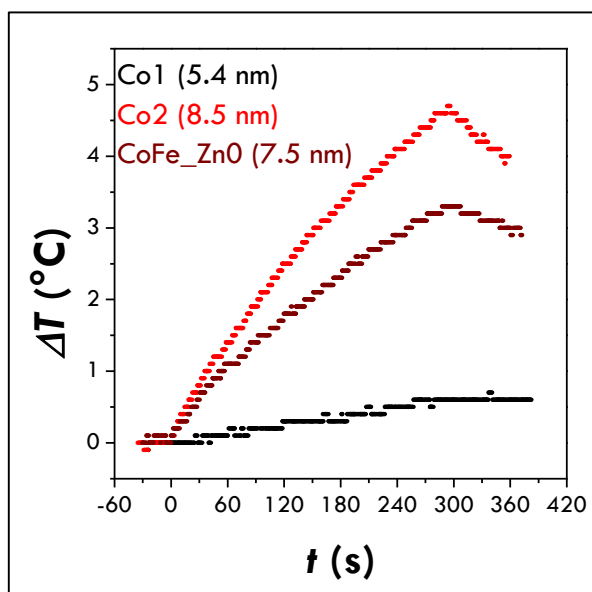
Fig. 5.5.4 Heating curves obtained on water colloidal dispersions of the Co1 and Co2 samples at 25 °C and under a magnetic field of f=183 kHz and H_0=17 kA/m. For comparison, the heating curve of the sample CoFe_Zn0 (Chapter 4) is shown.
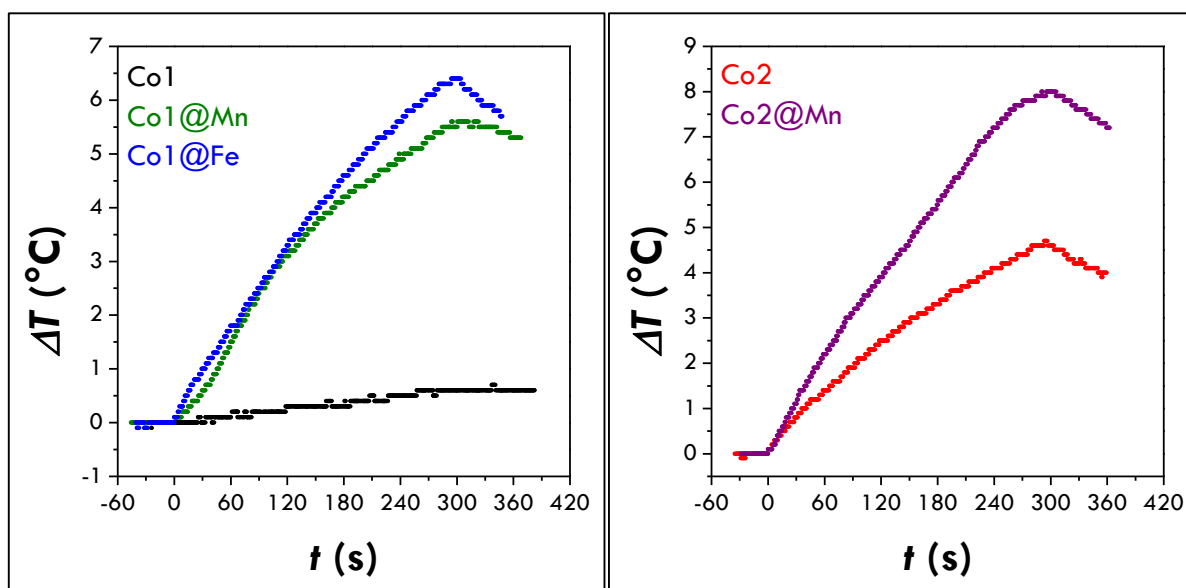
Fig. 5.5.5 Heating curves obtained on water colloidal dispersions of the Co1 (*left panel*) and Co2 (*right panel*) samples and the corresponding core@shell systems at 25 °C and under a magnetic field of f=183 kHz and H_0=17 kA/m.

Tab. 5.5.3 Specific Adsorpion Rate (SAR) and Intrinsic Loss Power (ILP) values for the Co1 and Co2 samples and the corresponding core@shell systems (25 °C, 183 kHz, 17 kA/m) together with the crystallite and particle sizes. SAR and ILP values are normalised for the total mass of ferrite (W/g$_{ox}$, nH·m^2/kg$_{ox}$).

Sample	<D$_{XRD}$> (nm)	<D$_{TEM}$> (nm)	SAR (W/g$_{ox}$)	ILP (W/g$_{ox}$)
Co1	5.8±0.2	5.4±0.9	-	-
Co1@Mn	10.8±0.3	10.5±1.3	19±2	0.36±0.04
Co1@Fe	8.3±0.3	8.5±1.2	45±5	0.85±0.08
Co2	8.4±0.3	9.4±1.0	33±3	0.63±0.06
Co2@Mn	11.3±0.8	14.3±1.6	51±5	0.97±0.09

In order to better understand the hyperthermic properties magnetic measurements were performed on Co1 and the corresponding core-shell system coated with manganese ferrite Co1@Mn. The temperature dependence of the magnetisation for the samples Co1 and Co1@Mn have been studied by ZFC-FC protocols and are shown in **Fig. 5.5.6**. ZFC curves for both the samples show a unique maximum that can be associated with a single nanoparticles population. This is confirmed by the first derivative, $d(M_{FC} - M_{ZFC})/dT$, which gives an estimate of the anisotropy energy barrier distribution (**Fig. 5.5.6**). Indeed, the difference $(M_{FC} - M_{ZFC})$ can be considered a good approximation of M_{TRM}(R.W. Chantrell et al., 1991). Values of T_{max}, T_{irr} and T_b (**Tab. 5.5.4**) have been found for the core@shell sample, as expected, higher than those of the core, in agreement with the higher particle size. The difference $(T_{irr} - T_{max})$ has been found to be 40 K for the Co1 sample and 16 K for the Co1@Mn sample, suggesting a decrease in the polydispersity of the barrier energy distribution. These data further support the hypothesised scenario of an homogenous growth of the Co1 cores for the creation a core@shell architecture.
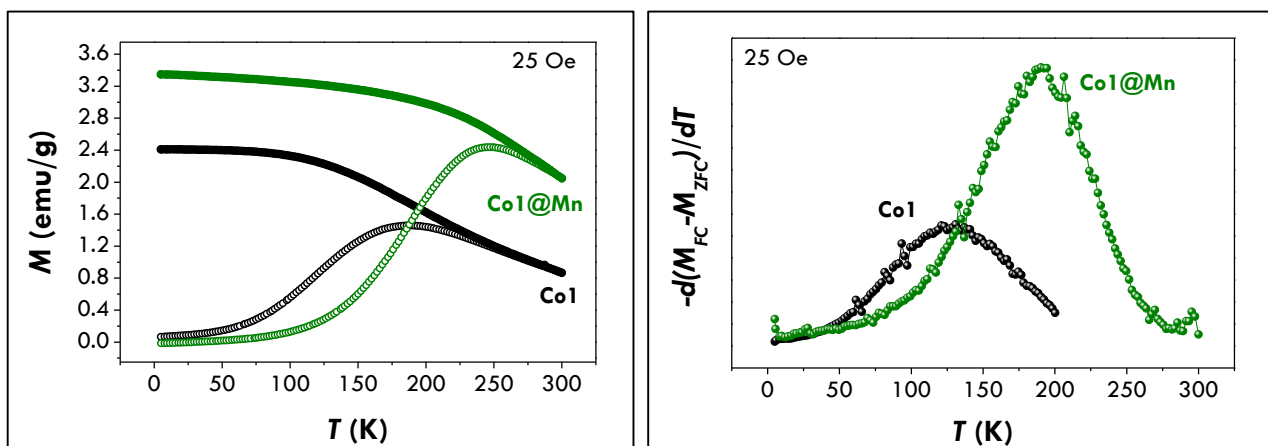
Fig. 5.5.6 Temperature dependence of the magnetisation obtained under 25 Oe by Zero Field Cooled – Field Cooled protocols (*left panel*) and anisotropy energy barrier distributions estimated by the first derivative $d(M_{FC} - M_{ZFC})/dT$ on the sample Co1 and the corresponding core@shell system (Co1@Mn).

Tab. 5.5.4 List of the main magnetic properties of the sample Co1 and the corresponding core@shell system (Co1@Mn).

Sample	D_{XRD} (nm)	D_{TEM} (nm)	Inorganic phase	T_{max} (K)	$T_{irr3\%}$ (K)	T_b (K)	H_c (kOe)	M^{5K} (50 kOe) (emu/g)	M_s^{RT} (emu/g)
Co1	5.8±0.2	5.4±0.9	73%	188±19	228±23	126±13	14±1	94±9	81±8
Co1@Mn	8.4±0.3	9.4±1.0	84%	248±25	264±26	183±18	8.1±0.8	92±8	77±3

M vs H curves at 5 K for the Co1 are characterised by a hysteresis loop that is closed only at the maximum applied field of 50 kOe (**Fig. 5.5.7**, *left panel*). Due to this peculiarity, it is not possible to estimate a saturation magnetisation for this sample but a high value of 94±9 emu/g is obtained for the magnetisation at 50 kOe (**Tab. 5.5.4**).
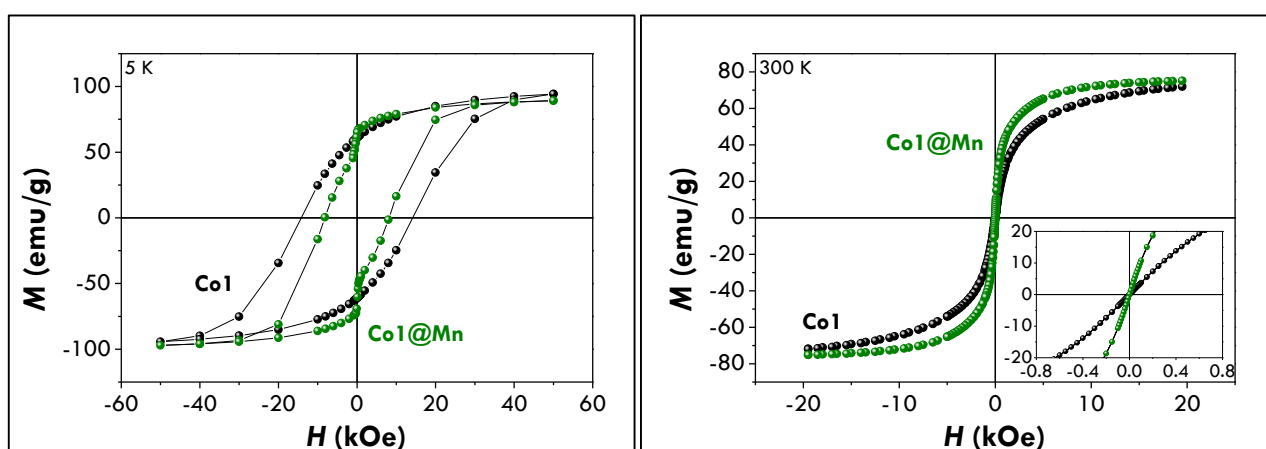
Fig. 5.5.7 Field dependence of the magnetisation at 5 K (*left panel*) and 300 K (*right panel*) of the sample Co1 and the corresponding core@shell system (Co1@Mn).

In-field Mössbauer measurements allowed to determine the cationic distribution and to estimate the corresponding theoretical saturation magnetisation for the sample Co1 (**Fig. 5.5.8**).
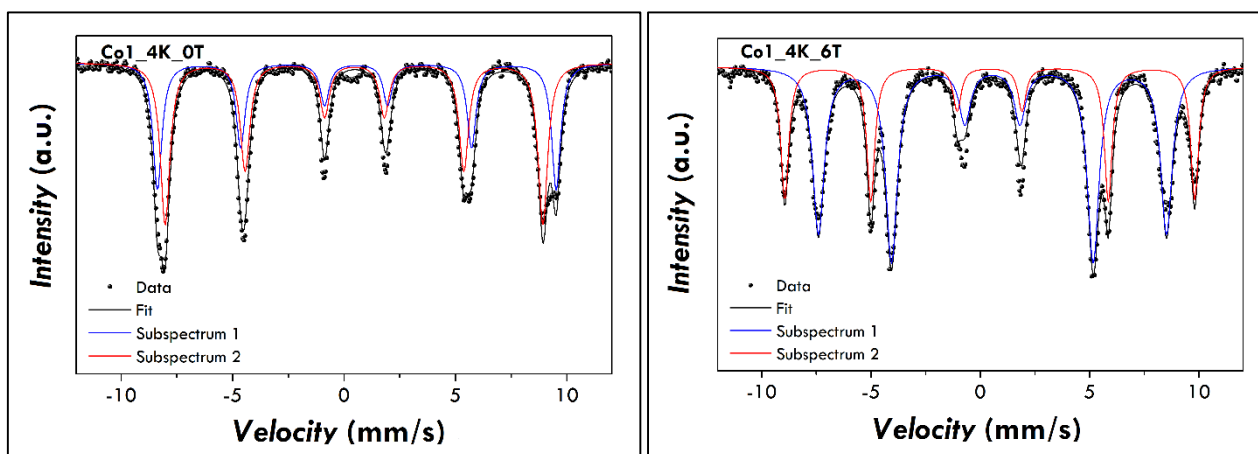
Fig. 5.5.8 4.2 K Mössbauer spectra of the Co1 sample recorded in the absence (*left panel*) and in the presence of an external magnetic field (6T) (*right panel*). Note that the doublet in the centre of the spectra is related to the metallic iron dissolved in the aluminium foil used as sample holder.

Tab. 5.5.5 Mössbauer parameters of the spectrum recorded on the Co1 sample at 4.2 K in the absence of an external magnetic field (0 T): isomer shift (δ), quadrupole splitting (ΔE_Q) and hyperfine field (B_{Hf}). Last column lists the interpretation for each subspectrum.

Sample	Signal	δ (mm/s)	ΔE_Q (mm/s)	B_{Hf} (T)	Interpretation
Co1	Sextet	0.43	0.01(1)	55.4(1)	Fe^{III} in the T_d of spinel
	Sextet	0.56	-0.01(1)	52.5(1)	Fe^{III} in the O_h of spinel

Tab. 5.5.6 Mössbauer parameters of the spectrum recorded on the Co1 sample at 4.2 K under an intense magnetic field (6 T): isomer shift (δ), quadrupole splitting (Δ_{EQ}), effective magnetic field (B_{Hf}) and relative area (A) of the components. Last column lists the interpretation for each subspectrum.

Sample	Signal	δ (mm/s)	ΔE_Q (mm/s)	B_{eff} (T)	A (%)	Interpretation
Co1	Sextet	0.43(1)	0.01(1)	58.3(1)	34%	Fe^{III} in the T_d of spinel
	Sextet	0.56(1)	0.01(1)	49.4(1)	66%	Fe^{III} in the O_h of pinel

Whereas the sample Co1 was in superparamagnetic state at room temperature, at 4K it exhibits two sextets, which means that it is already in the blocked state (**Tab. 5.5.5**). The sample measured at 6T shows two well splitted sextets, and it is found that 34% of iron cations are in tetrahedral position and 66% are located in octahedral positions (**Tab. 5.5.6**). Taking into account this results the inversion degree (percentage of bivalent cations in octahedral position) is 0.68 and the formula will be $(Co_{0.32}Fe_{0.68})[Co_{0.68}Fe_{1.32}]O_4$, in agreement with the values obtained for $CoFe_2O_4$ nanoparticles by other authors. (Blanco-Gutiérrez et al., 2012; Carta et al., 2009; D. Carta et al., 2013; Fantechi et al., 2012; Peddis et al., 2011) Indeed, in the case of nanoparticles,

the theoretical value of 1 (inverse spinel) is never observed, and typical values in the 0.6-0.7 range are found due to a random distribution of cobalt and iron cations. Using the cosine equation (as described in paragraph 4.6.1), it is also possible to calculate the canting angles. Within the experimental error, we can consider that the magnetic moments of both sublattices are not canted. This justifies the high magnetisation value observed at the maximum applied field.

On the basis of the Néel model, which describes the ferrimagnetic behaviour of spinel ferrite as the sum of independent T_d and O_h sublattices, it is possible to estimate the saturation magnetisation for the cationic distribution obtained for the sample Co1. The computation has been carried out by using the following formula:

$$M_s = \frac{\mu \cdot \mu_B \cdot N_A}{MM}$$

Eq. 5.5.1

where μ is the total magnetic moment, μ_B is the Bohr magneton, N_A is the Avogadro number and MM is the molar mass.

The as-obtained value of saturation magnetisation is about 100 emu/g, which is quite near the experimental one (94±9 emu/g) recorded under a 50 kOe external field. This value is higher than that for bulk-material (80-90 emu/g)(Cullity and Graham, 2009; Smit and Wijn, 1959) but it can be justified by the partially inverted structure.(Peddis et al., 2011) A high coercive field of 14 kOe has been also obtained. This value is near the values reported in the literature for cobalt ferrite nanoparticles of similar size.(Duong et al., 2006; Fantechi et al., 2012; Peddis et al., 2013)

It must be noted that 5K *M vs H* curves for the Co1@Mn do not show a single-phase-like behaviour (**Fig. 5.5.7**, *left panel*). For bimagnetic core@shell nanostructures, the *M vs H* curves can be indeed one or two-stage loops, depending on the volume fraction of the soft phase (f_{soft}). When a one-stage hysteresis loop is obtained, the two magnetic phases are strongly coupled so that all the spins reverse at the same magnetic field value, called nucleation field. On the contrary, for high volume fraction of the soft phase typical two-stage hysteresis loops are expected. Indeed, the soft phase reverses at magnetic field values well below those of the hard phase.(López-Ortega et al., 2015a) These systems are referred as spring magnets.

M vs H curves for the sample Co1@Mn seems to resemble this kind of behaviour controlled by the shell of the soft phase. Indeed, the volume fraction of the shell is 67% of the total volume. These data seem to support once again the hypothesis that a core@shell structure was formed. However, it should be note that there are only a few works on spinel ferrite-based bimagnetic core@shell nanostructures(Almeida et al., 2014; Anil Kumar et al., 2013; Dupuis et al., 2014; Gavrilov-Isaac et al., 2014; Kim et al., 2013; Kishimoto et al., 1979; Lee et al., 2011; Li et al., 2015; Salazar-Alvarez et al., 2007; Song and Zhang, 2012; Sudakar and Kutty, 2004; Vichery et al., 2013, 2012) and the great majority of these papers have been published within the last three years. Among these studies, some papers have dealt with the magnetic properties of $CoFe_2O_4@MnFe_2O_4$ nanoparticles.(Kim et al., 2013; Lee et al., 2011; Song and Zhang, 2012) Both the studies from Lee *et al.*(Lee et al., 2011) and Song & Zhang(Song and Zhang, 2012) show uniform single-stage hysteresis loops for 15 nm particle (with a 9 nm for the core size) and for 6.5-9 nm particles (with a 6 nm for the core size) despite a high

volume fraction of the shell. On the contrary, Angelakeris *et al.*(Angelakeris et al., 2015) revealed a two-stage hysteresis loop, similarly to what we have observed but with substantially different ZFC-FC curves.

Moreover, Song & Zhang(Song and Zhang, 2012) systematically compared core@shell nanostructures with physical and chemical mixtures. They found two-stage hysteresis loops only for physical mixtures and, in particular, for a physical mixture of $CoFe_2O_4$ and $MnFe_2O_4$ in a molar ratio 4.42:1 they indicated *M vs H* curves similar to the one that we have observed. However, the molar ratio in our case is less than one and, in that case, a physical mixture should show a complete different shape of the hysteresis loop, i.e. governed by the soft phase (similar to the one thay reported for the 1:3.27 $CoFe_2O_4$:$MnFe_2O_4$). Finally, our results are in agreement with the Mossbauer and HRTEM/TEM data.

The magnetisation at 50 kOe of the Co1@Mn is equal to 92±8 emu/g, the same value obtained for the pure cobalt ferrite nanoparticles (Co1, 94±9 emu/g) (**Tab. 5.5.4**). On the contrary, the coercive field value for the core@shell sample (8.1±0.8 kOe) is lower than the Co1 one. Both these findings are indeed expected for $CoFe_2O_4$@$MnFe_2O_4$ nanoparticles with a high shell volume fraction. First, these phases are generally characterised by similar M_s values of the two phases and the coercivity is expected to be lower than the pure cobalt ferrite due to the coupling with the soft phase.

Room temperature *M vs H* curves were also measured for Co1 and Co1@Mn (**Fig. 5.5.7**, *right panel*). Both the samples are superparamagnetic at room temperature with zero coercivity and zero remnant magnetisation. The saturation magnetisation is almost the same at 300 K, in agreement with the behaviour at 5 K. However, the saturation state is reached in the core@shell sample at a lower magnetic field value. This can be probably related to the influence that the soft phase exerts on the hard phase spins, leading to a less anisotropic response of the hard phase.

5.6   Conclusions and perspectives

A hydrothermal method based on the hydrolysis of mixed cobalt-iron oleates has been used to produce two different samples of cobalt ferrite nanoparticles of different sizes. $CoFe_2O_4$@$M^{II}Fe_2O_4$ architectures, being $M^{II}Fe_2O_4$ magnetite/maghemite or manganese ferrite, have been prepared by a seed-mediated growth carried out under hydrothermal conditions. An increase of the particles size, accompanied by a decrease of the polydispersity index, have been observed in all core@shell samples. Moreover, HRTEM have shown spherical particles with the crystalline planes extended over the whole particle with no evidences for defects. Room Temperature Mössbauer Spectroscopy have been also useful to study, in comparison with core@shell particles of similar sizes, a physical mixture *ah-hoc* prepared. These experiments allows to exclude the independent growth of the second phase and suggest the effective production of heterostructures with an intimate contact between the hard and the soft phases. Moreover, the effect has been clearly visualised with the SAR values, revealing an improved efficiency for all core@shell samples with respect to the corresponding core. Finally, preliminary magnetic measurements conducted on two samples could be probably coherent with the production of spring magnet systems but other measurements are needed to more carefully characterise the whole set of samples.

As already observed for the $Zn_xCo_{1-x}Fe_2O_4$ samples, it can be difficult to explain the heating abilities of the samples only on the basis of static magnetic properties. Therefore, in order to justify the obtained SAR values and the increase recorded for core@shell samples, it would be necessary to study the dynamic properties of the samples by means of AC magnetometry. To the best of our knowledge, only two works test the hyperthermic properties of spinel ferrite core@shell systems. These previous studies(Lee et al., 2011; Noh et al., 2012) justified the high SAR values of such nanostructures on the basis of exchange-coupled phenomena but an in-depth discussion of the dynamic properties and the exchange coupling phenomena is still lacking.

Together with the AC magnetometry, it would be also fundamental to characterise these samples in terms of single-particle chemical composition by Electron Energy Loss Spectroscopy (EELS) in order to verify if core@shell systems were effectively produced, and if a definite interface was created (i.e. a net confinement of the phases).

5.7   Materials and methods

5.7.1   Chemicals.

Oleic acid (>99.99%), 1-pentanol (99.89%), hexane (84.67%) and toluene (99.26%) were purchased from Lach-Ner; 1-octanol (>99.99%) and $Mn(NO_3)_2 \cdot 4H_2O$ (>97.0%) from Sigma-Aldrich; absolute ethanol and $Co(NO_3)_2 \cdot 6H_2O$ (99.0%) from Penta; NaOH (>98.0%) from Fluka; $Fe(NO_3)_3 \cdot 9H_2O$ (98.0%) from Lachema; $FeCl_2 \cdot 4H_2O$ (99%) from Merck.

5.7.2   X-ray Diffraction (XRD)

The samples were characterized by X-ray Diffraction (XRD), using a PANalytical X'Pert PRO with Cu Kα radiation (1.5418Å), secondary monochromator and PIXcel position sensitive detector. Calibration of peak position and instrumental width was done using powder LaB_6 from NITS. The hexane dispersions were dried on a glass plate and measured in the angular range 10°-90° with step 0.039°. The analyses of the XRD patterns (identification of the crystalline phase, background subtraction) were done by the PANalytical X'Pert HighScore software. The peaks in the interval 28°-66° were fitted in Gnuplot 4.2.6 by Voigt function (convolution of Gaussian and Lorentzian) in reciprocal space

$$q = \frac{2sin\theta}{\lambda} = \frac{\sqrt{h^2 + k^2 + l^2}}{a}$$

Eq. 5.7.1

The crystallite size (diameter) was obtained from full width at half maximum of q (denoted as Γ_q) by

$$d = \frac{1.10}{\Gamma_q}$$

Eq. 5.7.2

Peaks widths (Γ_q) were constrained in groups 311-511-422-222, 440-220-531, 440. The constant in the denominator of Eq. 5.7.2 was obtained for the peak of Fourier-transformed solid spheres with volume-weighted log-normal size distribution $\sigma= 0.18$ – in this case, the peak shape almost coincides with Gauss function.

5.7.3   Transmission Electron Microscope (TEM, HRTEM)

TEM images were obtained by using a JEOL 200CX operating at 200 kV. A drop of the colloidal dispersion was dried on a carbon-coated copper grid. The particle size distribution was obtained by measuring in the automatic mode over 1000 particles by means of the software Pebbles and adopting a spherical or cuboid shape.(Mondini et al., 2012) The mean particle diameter was calculated as the average value and the polydispersity index as the percent ratio between the standard deviation and the average value.

HRTEM images were carried out using JEM 2010 UHR equipped with a Gatan imaging filter (GIF) and a 794 slow scan CCD camera.

5.7.4   ICP-AES

The samples' chemical composition was studied by Inductively Coupled Plasma - Atomic Emission Spectrometry (ICP-AES). The dried samples were digested by using HNO_3. The digested sample solutions were stirred at room temperature for 1 h, then heated up to ~50 °C for 2 h. The solutions were left to cool down, filtered and diluted by using 1%v/v HNO_3 solution. The ICP measurements were made by means of a Liberty 200 ICP Varian spectrometer under the following conditions: Fe line: 259.940 nm, Co line: 238.892 nm, Mn line: 257.610 nm; Fe, Co and Mn concentration range: (0.1÷1.5) ppm; Fe detection range: (0.015÷750) ppm, Co detection range: (0.050÷2500) ppm, Mn detection range: (0.003÷150) ppm. The analyses have been repeated two times on different portions of the samples. The chemical formulas were calculated by assuming the absence of anions vacancies.

5.7.5   Fourier Transform - Infrared Spectroscopy (FT-IR)

Fourier Transform - Infrared Spectroscopy (FT-IR) and ThermoGravimetric Analyses (TGA) were carried out in order to study the capping agent and to estimate the organic phase content. Transform Infrared Spectroscopy (FT-IR) spectra were recorded in the region from 350 to 4000 cm^{-1} by using a Bruker Vertex 70 spectrophotometer on the colloidal dispersions by means of a Platinum ATR Unit A 225, (standard ATR crystal material: diamond).

5.7.6   ThermoGravimetric Analyses (TGA)

TGA curves were obtained on powders by using a Mettler-Toledo TGA/SDTA 851 in the 25 -1000 °C range, with a heating rate of 10 °C/min under 50 mL/min O_2 flow.

5.7.7 ^{57}Fe Mössbauer Spectroscopy

Room temperature ^{57}Fe Mössbauer spectroscopy was done on Wissel spectrometer using transmission arrangement and scintillating detector ND-220-M (NaI:Tl$^+$). The 4 K spectra (under zero or 6 T external magnetic field) were recorded in the Joint Laboratory of Low Temperatures in Troja. A α-Fe foil was used as a

standard, and fitting procedure was done by NORMOS program. The in-field measurements were done in a perpendicular arrangement of the external magnetic field with respect to the γ-beam and are useful to get information about the cationic distribution and the canting phenomena in the spinel structure. Indeed, the angle θ between the magnetic moment ($\vec{\mu}$) and the applied magnetic field have been estimated thanks to the following equation:

$$\mathbf{B}_{\mathbf{eff}}^2 = \mathbf{B}_{\mathbf{hf}}^2 + \mathbf{B}_{\mathbf{app}}^2 - 2\mathbf{B}_{\mathbf{hf}}\mathbf{B}_{\mathbf{app}}\mathbf{cos\theta}$$

Where B_{hf} is the hyperfine field, B_{eff} the total effective magnetic field at the nucleus, B_{app} the external applied magnetic field and α is the angle between B_{eff} and B_{app}.

The angle θ corresponds to the canting angle for the octahedral sites whereas for the tetrahedral ones, the canting angle is equal to π- θ . This is because of the relative arrangement of the hyperfine and applied fields vectors that are parallel or antiparallel aligned for tetrahedral or octahedral sites, respectively.

5.7.8 DC magnetometry

Magnetic properties were studied by means of a Quantum Design SQUID (Hmax = 50 kOe). Different kind of magnetic measurements were carried out. Magnetisation versus magnetic field curves were measured at 300 K and 5 k between -50 kOe and +50 kOe. The saturation magnetisation (Ms) was estimated if possible by using the equation

$$M = \boldsymbol{M_s} \cdot \left(1 - \frac{a}{H} - \frac{b}{H^2}\right)$$

for H tending to ∞.(Morrish, 1965)

Magnetisation versus temperature measurements were performed using Zero-Field-Cooled (ZFC), Field-Cooled (FC) protocols. ZFC and FC magnetisation measurements were carried out by cooling the sample from room temperature to 5 K in zero magnetic field; then, a static magnetic field of 25 Oe was applied. M_{ZFC} was measured during the warmup from 5 K to 300 K, whereas M_{FC} was recorded during the subsequent cooling. The difference ($M_{FC} - M_{ZFC}$), being a good approximation of M_{TRM}(R W Chantrell et al., 1991) has been used to describe the energy profile. From these curves and the ZFC-FC ones, the characteristics temperatures T_{max}, T_{irr} and T_b were obtained as follows. T_{max} is the temperature of the maximum in the ZFC curve. T_{irr} was calculated by considering a 3% of difference between the M_{FC} and the M_{ZFC}. T_b is the blocking temperature calculated by means of the first derivative of the difference curve ($M_{FC} - M_{ZFC}$) as the temperature at which the 50% of the nanoparticles are in the superparamagnetic state.

5.7.9 Specific Absorption Rate (SAR) measurements

Calorimetric measurements of SAR were carried out by means of a non-adiabatic experimental set-up built at the LAboratorio di Magnetismo Molecolare (LA.M.M) by means of a power supply CELESs MP6/400 (FIVES CELES), a water-cooled heating station connected to the power supply and an induction coil. Heating curves were recorded under a magnetic field of 17 kA/m and 183 kHz for 300 s on water colloidal dispersions of the magnetic nanoparticles. Indeed, the hydrophobic nanoparticles were made hydrophilic by intercalation process with cetyltrimethylammonium bromide (CTAB, $(C_{16}H_{33})N(CH_3)_3Br$). The concentration of the colloidal dispersion was 3.4 mg/ml for all the samples. The temperature of the sample was monitored by an optical fiber

probe (OPTOCON-FOTEMP) dipped into the solution. Samples were surrounded by polystyrene and hosted in a glass Dewar, equipped by an ethylene glycol thermostat, to ensure the proper thermal isolation. The Specific Adsorption Rate (SAR), i.e. the thermal power per mass unit, values has been estimated by a linear curve fitting in the first 20 s of the heating curves (*initial slope method*).

Conclusions

In this thesis, two different strategies have been investigated for tuning the magnetic properties of cobalt ferrite nanoparticles in order to study its effect on their heating abilities for Magnetic Fluid Hyperthermia. Dealing with the intrinsic toxicity of cobalt ferrite, the two approaches are based on the decrease of the concentration of cobalt in the material by zinc substitution or on the confinement of cobalt ferrite in core@shell architectures by means of magnetite/maghemite or manganese ferrite shell, which are considered biocompatible or with a reduced toxicity.

Zn-substitution samples have been prepared by the consolidated high temperature thermal decomposition of metalorganic precursors method (heating up) while the core@shell architectures have been achieved setting up a novel hydrothermal synthetic approach based on the seed-mediated growth process.

Zn-substitution strategy has produced nanoparticles differing only for the cobalt content so that the study of the magnetic and hyperthermic properties has been possible beyond other parameters effects (crystallite diameter, particle diameter and its distribution, hydrodynamic diameter and its distribution, type and amount of capping agent). High saturation magnetisation values have been obtained at 5 K for all samples and at 300 K for the cobalt ferrite sample and the substituted-one with the lowest zinc content. These latter two samples are capable to heat up the colloidal dispersion under the application of an alternate magnetic field but not in the same extent despite the same values of saturation magnetisation (~90 emu/g). These findings have highlighted the importance of other parameters affecting the hyperthermal efficiency. In order to better understand, these different behaviours AC magnetometry, Mössbauer Spectroscopy and DLS analyses were performed. By studying both the Néel and the Brown relaxation times, the higher SAR value obtained for cobalt ferrite nanoparticles have been justified by the higher magnetic anisotropy, which make the effective relaxation time of the particles matching the characteristic time of the SAR measurement. Although the SAR values are not among the most promising in the literature for Magnetic Fluid Hyperthermia, this characterisation approach can be considered extremely useful in order to design new heat mediators.

The production of core@shell nanostructures $CoFe_2O_4@M^{II}Fe_2O_4$ have been obtained by a seed-mediated growth carried out under hydrothermal conditions. Indeed, hydrothermal method has been chosen due to its several advantages, in particular its versatility. The characterisation by a multitechnique approach has suggested the formation of coupled systems: an increase of the particles size accompanied by a decrease of the polydispersity index (TEM), the crystalline planes extended within the entire spherical particles (HRTEM), the Room Temperature Mössbauer spectra not compatible with a physical mixture of the single phases, taken as reference sample. SAR measurements suggest the effective formation of bimagnetic core@shell nanoparticles with a higher efficiency of all these systems with respect to the original core. Finally, preliminary magnetic measurements have shown hysteretic behaviour compatible with of spring magnet systems. These heteroarchitectures represent promising materials for Magnetic Fluid Hyperthermia due to the homogeneous coating of the core with a biocompatible shell and due to the improved SAR values observed for all synthesised samples. However, for a deep understanding of the source of this optimisation, a further characterisation of a greater number of samples and also by means of AC magnetometry and Electron Energy Loss Spectroscopy

(EELS) would be necessary. Furthermore, it is worth to note that before any possible biomedical application cytotoxicity assays and cobalt release tests have to be assessed in order to verify the effective coating of the cobalt ferrite cores.

References

AIOM, AIRTUM, 2012. I numeri del cancro in Italia.

Almeida, T.P., Moro, F., Fay, M.W., Zhu, Y., Brown, P.D., 2014. Tuneable magnetic properties of hydrothermally synthesised core/shell CoFe2O4/NiFe2O4 and NiFe2O4/CoFe2O4 nanoparticles. J. Nanoparticle Res. 16, 2395. doi:10.1007/s11051-014-2395-1

Alphandéry, E., Faure, S., Raison, L., Duguet, E., Howse, P.A., Bazylinski, D.A., 2011a. Heat Production by Bacterial Magnetosomes Exposed to an Oscillating Magnetic Field. J. Phys. Chem. C 115, 18–22. doi:10.1021/jp104580t

Alphandéry, E., Faure, S., Seksek, O., Guyot, F., Chebbi, I., 2011. Chains of cobalt doped magnetosomes extracted from AMB-1 magnetotactic bacteria for application in alternative magnetic field cancer therapy. ACS Nano 5, 6279–6296. doi:10.1021/nn201290k

Alphandéry, E., Faure, S., Seksek, O., Guyot, F., Chebbi, I., 2011b. Chains of Magnetosomes Extracted from AMB-1 Magnetotactic Bacteria for Application in Alternative Magnetic Field Cancer Therapy. ACS Nano 5, 6279–6296. doi:10.1021/nn201290k

American Cancer Society [WWW Document], n.d. URL http://www.cancer.org/index

Angelakeris, M., Li, Z.-A., Hilgendorff, M., Simeonidis, K., Sakellari, D., Filippousi, M., Tian, H., Van Tendeloo, G., Spasova, M., Acet, M., Farle, M., 2015. Enhanced biomedical heat-triggered carriers via nanomagnetism tuning in ferrite-based nanoparticles. J. Magn. Magn. Mater. 381, 179–187. doi:10.1016/j.jmmm.2014.12.069

Anil Kumar, P., Ray, S., Chakraverty, S., Sarma, D.D., 2013. Engineered spin-valve type magnetoresistance in Fe3O4-CoFe2O4 core-shell nanoparticles. Appl. Phys. Lett. 103, 102406. doi:10.1063/1.4819956

Anno 2012 Le principali cause di morte in italia, 2014.

Arulmurugan, R., Vaidyanathan, G., Sendhilnathan, S., Jeyadevan, B., 2006. Thermomagnetic properties of Co1−xZnxFe2O4 (x=0.1–0.5) nanoparticles. J. Magn. Magn. Mater. 303, 131–137. doi:10.1016/j.jmmm.2005.10.237

Associazione Italiana per la Ricerca sul Cancro (AIRC) [WWW Document], n.d. URL http://www.airc.it/

Atkinson, W.J., Brezovich, I. a, Chakraborty, D.P., 1984. Usable frequencies in hyperthermia with thermal seeds. IEEE Trans. Biomed. Eng. 31, 70–75. doi:10.1109/TBME.1984.325372

Autumn, K., Sitti, M., Liang, Y. a, Peattie, A.M., Hansen, W.R., Sponberg, S., Kenny, T.W., Fearing, R., Israelachvili, J.N., Full, R.J., 2002. Evidence for van der Waals adhesion in gecko setae. Proc. Natl. Acad. Sci. U. S. A. 99, 12252–12256. doi:10.1073/pnas.192252799

Ayyappan, S., Gnanaprakash, G., Panneerselvam, G., Antony, M.P., Philip, J., 2008. Effect of Surfactant Monolayer on Reduction of Fe 3 O 4 Nanoparticles under Vacuum. J. Phys. Chem. C

112, 18376–18383. doi:10.1021/jp8052899

Ayyappan, S., Paneerselvam, G., Antony, M.P., Philip, J., 2011. Structural stability of ZnFe2O4 nanoparticles under different annealing conditions. Mater. Chem. Phys. 128, 400–404. doi:10.1016/j.matchemphys.2011.03.012

Baaziz, W., Pichon, B.P., Liu, Y., Grenèche, J.-M., Ulhaq-Bouillet, C., Terrier, E., Bergeard, N., Halté, V., Boeglin, C., Choueikani, F., Toumi, M., Mhiri, T., Begin-Colin, S., 2014. Tuning of Synthesis Conditions by Thermal Decomposition toward Core–Shell Co x Fe 1– x O@Co y Fe 3– y O 4 and CoFe 2 O 4 Nanoparticles with Spherical and Cubic Shapes. Chem. Mater. 26, 5063–5073. doi:10.1021/cm502269s

Baldi, G., Bonacchi, D., Innocenti, C., Lorenzi, G., Sangregorio, C., 2007. Cobalt ferrite nanoparticles: The control of the particle size and surface state and their effects on magnetic properties. J. Magn. Magn. Mater. 311, 10–16. doi:10.1016/j.jmmm.2006.11.157

Balivada, S., Rachakatla, R.S., Wang, H., Samarakoon, T.N., Dani, R.K., Pyle, M., Kroh, F.O., Walker, B., Leaym, X., Koper, O.B., Tamura, M., Chikan, V., Bossmann, S.H., Troyer, D.L., 2010. A/C magnetic hyperthermia of melanoma mediated by iron(0)/iron oxide core/shell magnetic nanoparticles: a mouse study. BMC Cancer 10, 119. doi:10.1186/1471-2407-10-119

Bao, N., Shen, L., Wang, Y.A., Ma, J., Mazumdar, D., Gupta, A., 2009. Controlled growth of monodisperse self-supported superparamagnetic nanostructures of spherical and rod-like CoFe2O4 nanocrystals. J. Am. Chem. Soc. 131, 12900–1. doi:10.1021/ja905811h

Barber, D.J., Freestone, I.C., 1990. An Investigatino of the Origin of the Colour of the Lycurgus Cup by Analytical Transmission Electron Microscopy. Archaeometry 1, 33–45. doi:10.1111/j.1475-4754.1990.tb01079.x

Baronzio, G.F., Hager, E.D., 2006. Hyperthermia in Cancer Treatment: A Primer, Landes Bio. ed. Springer US, Boston, MA. doi:10.1007/978-0-387-33441-7

Barry, M.A., Behnke, C.A., Eastman, A., 1990. Activation of programmed cell death (apoptosis) by cisplatin, other anticancer drugs, toxins and hyperthermia. Biochem. Pharmacol. 40, 2353–2362. doi:10.1016/0006-2952(90)90733-2

Batlle, X., Pérez, N., Guardia, P., Iglesias, O., Labarta, a., Bartolomé, F., García, L.M., Bartolomé, J., Roca, a. G., Morales, M.P., Serna, C.J., 2011. Magnetic nanoparticles with bulklike properties (invited). J. Appl. Phys. 109, 07B524. doi:10.1063/1.3559504

Bedanta, S., Kleemann, W., 2009. Supermagnetism. J. Phys. D. Appl. Phys. 42, 013001. doi:10.1088/0022-3727/42/1/013001

Bellini, S., 1963a. Su di un particolare comportamento di batteri d'acqua dolce.

Bellini, S., 1963b. Ulteriori studi sui "Batteri Magnetosensibili".

Blakemore, R., 1975. Magnetotactic bacteria. Science (80-.). 190, 377–379.

doi:10.1126/science.170679

Blanco-Andujar, C., Ortega, D., Southern, P., Pankhurst, Q. a, Thanh, N.T.K., 2015. High performance multi-core iron oxide nanoparticles for magnetic hyperthermia: microwave synthesis, and the role of core-to-core interactions. Nanoscale 7, 1768–75. doi:10.1039/c4nr06239f

Blanco-Gutiérrez, V., Gallastegui, J.A., Bonville, P., Torralvo-Fernández, M.J., Sáez-Puche, R., 2012. MFe2O4 (M: Co2+, Ni2+) nanoparticles: Mössbauer and X-ray absorption spectroscopies studies and high-temperature superparamagnetic behavior. J. Phys. Chem. C 116, 24331–24339. doi:10.1021/jp307371q

Bohara, R.A., Thorat, N.D., Chaurasia, A.K., Pawar, S.H., 2015. Cancer cells extinction through magnetic fluid hyperthermia treatment produced by superparamagnetic Co-Zn Ferrite nanoparticles. RSC Adv. 5, 47225–47234. doi:10.1039/C5RA04553C

Cancer Research UK [WWW Document], n.d. URL http://www.cancerresearchuk.org/

Cannas, C., Ardu, A., Musinu, A., Peddis, D., Piccaluga, G., 2008. Spherical Nanoporous Assemblies of Iso-Oriented Cobalt Ferrite Nanoparticles: Synthesis, Microstructure, and Magnetic Properties. Chem. Mater. 20, 6364–6371. doi:10.1021/cm801839s

Cannas, C., Ardu, A., Musinu, A., Suber, L., Ciasca, G., Amenitsch, H., Campi, G., 2015. Hierarchical Formation Mechanism of CoFe 2 O 4 Mesoporous Assemblies. ACS Nano 9, 7277–7286. doi:10.1021/acsnano.5b02145

Cannas, C., Musinu, A., Ardu, A., Orrù, F., Peddis, D., Casu, M., Sanna, R., Angius, F., Diaz, G., Piccaluga, G., 2010a. CoFe 2 O 4 and CoFe 2 O 4 /SiO 2 Core/Shell Nanoparticles: Magnetic and Spectroscopic Study. Chem. Mater. 22, 3353–3361. doi:10.1021/cm903837g

Cannas, C., Musinu, A., Ardu, A., Orrù, F., Peddis, D., Casu, M., Sanna, R., Angius, F., Diaz, G., Piccaluga, G., 2010b. CoFe2O4 and CoFe2O4/SiO2 Core/Shell Nanoparticles: Magnetic and Spectroscopic Study. Chem. Mater. 22, 3353–3361. doi:10.1021/cm903837g

Cannas, C., Musinu, A., Peddis, D., Piccaluga, G., 2004. New Synthesis of Ferrite–Silica Nanocomposites by a Sol–Gel Auto-Combustion. J. Nanoparticle Res. 6, 223–232. doi:10.1023/B:NANO.0000034679.22546.d7

Cannas, C., Musinu, A., Peddis, D., Piccaluga, G., 2006. Synthesis and Characterization of CoFe 2 O 4 Nanoparticles Dispersed in a Silica Matrix by a Sol−Gel Autocombustion Method. Chem. Mater. 18, 3835–3842. doi:10.1021/cm060650n

Cara, C., Musinu, A., Mameli, V., Ardu, A., Niznansky, D., Bursik, J., Scorciapino, M.A., Manzo, G., Cannas, C., 2015. Dialkylamide as Both Capping Agent and Surfactant in a Direct Solvothermal Synthesis of Magnetite and Titania Nanoparticles. Cryst. Growth Des. 15, 2364–2372. doi:10.1021/acs.cgd.5b00160

Carrey, J., Mehdaoui, B., Respaud, M., 2011. Simple models for dynamic hysteresis loop calculations

of magnetic single-domain nanoparticles: Application to magnetic hyperthermia optimization. J. Appl. Phys. 109, 083921. doi:10.1063/1.3551582

Carta, D., Casula, M.F., Falqui, a., Loche, D., Mountjoy, G., Sangregorio, C., Corrias, a., 2009. A Structural and Magnetic Investigation of the Inversion Degree in Ferrite Nanocrystals MFe 2 O 4 (M = Mn, Co, Ni). J. Phys. Chem. C 113, 8606–8615. doi:10.1021/jp901077c

Carta, D., Corrias, A., Falqui, A., Brescia, R., Fantechi, E., Pineider, F., Sangregorio, C., 2013. EDS, HRTEM/STEM, and X-ray absorption spectroscopy studies of co-substituted maghemite nanoparticles. J. Phys. Chem. C 117, 9496–9506. doi:10.1021/jp401706c

Carta, D., Marras, C., Loche, D., Mountjoy, G., Ahmed, S.I., Corrias, A., 2013. An X-ray absorption spectroscopy study of the inversion degree in zinc ferrite nanocrystals dispersed on a highly porous silica aerogel matrix. J. Chem. Phys. 138, 054702. doi:10.1063/1.4789479

Cavaliere, R., Ciocatto, E.C., Giovanella, B.C., Heidelberger, C., Johnson, R.O., Margottini, M., Mondovi, B., Moricca, G., Rossi-Fanelli, A., 1967. Selective heat sensitivity of cancer cells. Biochemical and clinical studies. Cancer 20, 1351–1381. doi:10.1002/1097-0142(196709)20:9<1351::AID-CNCR2820200902>3.0.CO;2-#

Céspedes, E., Byrne, J.M., Farrow, N., Moise, S., Coker, V.S., Bencsik, M., Lloyd, J.R., Telling, N.D., 2014. Bacterially synthesized ferrite nanoparticles for magnetic hyperthermia applications. Nanoscale 6, 12958–12970. doi:10.1039/C4NR03004D

Chantrell, R.W., El-Hilo, M., O'Grady, K., 1991. Spin-glass behavior in a fine particle system. IEEE Trans. Magn. 27, 3570–3578. doi:10.1109/20.102929

Chantrell, R.W., El-Hilo, M., O'Grady, K., 1991. Spin-Glass behaviour in fine particle system. IEEE Trans. Magn. 27, 3570–3578.

Cheng, Y.T., Rodak, D.E., Wong, C.A., Hayden, C.A., 2006. Effects of micro- and nano-structures on the self-cleaning behaviour of lotus leaves. Nanotechnology 17, 1359–1362. doi:10.1088/0957-4484/17/5/032

Coey, J.M.D., 2010. Magnetism and Magnetic Materials.

Cullity, B.D., Graham, C.D., 2009. Introduction to Magnetic Materials.

D'Arienzo, M., Carbajo, J., Bahamonde, A., Crippa, M., Polizzi, S., Scotti, R., Wahba, L., Morazzoni, F., 2011. Photogenerated defects in shape-controlled TiO2 anatase nanocrystals: a probe to evaluate the role of crystal facets in photocatalytic processes. J. Am. Chem. Soc. 133, 17652–61. doi:10.1021/ja204838s

Dalu, F., 2014. Un nuovo concetto di colore: sintesi e caratterizzazione di nanoparticelle collidali di argento. Università degli Studi di Cagliari.

Daou, T.J., Grenèche, J.M., Pourroy, G., Buathong, S., Derory, a., Ulhaq-Bouillet, C., Donnio, B., Guillon, D., Begin-Colin, S., 2008. Coupling agent effect on magnetic properties of functionalized magnetite-based nanoparticles. Chem. Mater. 20, 5869–5875. doi:10.1021/cm801405n

de la Presa, P., Luengo, Y., Multigner, M., Costo, R., Morales, M.P., Rivero, G., Hernando, A., 2012. Study of Heating Efficiency as a Function of Concentration, Size, and Applied Field in γ-Fe2O3 Nanoparticles. J. Phys. Chem. C 116, 25602–25610. doi:10.1021/jp310771p

de Mello Donegá, C., Liljeroth, P., Vanmaekelbergh, D., 2005. Physicochemical evaluation of the hot-injection method, a synthesis route for monodisperse nanocrystals. Small 1, 1152–62. doi:10.1002/smll.200500239

Deatsch, A.E., Evans, B.A., 2014. Heating efficiency in magnetic nanoparticle hyperthermia. J. Magn. Magn. Mater. 354, 163–172. doi:10.1016/j.jmmm.2013.11.006

Del Bianco, L., Fiorani, D., Testa, a. M., Bonetti, E., Savini, L., Signoretti, S., 2002. Magnetothermal behavior of a nanoscale Fe/Fe oxide granular system. Phys. Rev. B 66, 174418. doi:10.1103/PhysRevB.66.174418

Demortière, a, Panissod, P., Pichon, B.P., Pourroy, G., Guillon, D., Donnio, B., Bégin-Colin, S., 2011. Size-dependent properties of magnetic iron oxide nanocrystals. Nanoscale 3, 225–32. doi:10.1039/c0nr00521e

Dikomey, H. H. Kampinga, E., 2001. Hyperthermic radiosensitization: mode of action and clinical relevance. Int. J. Radiat. Biol. 77, 399–408. doi:10.1080/09553000010024687

Dinh, C., Nguyen, T., Kleitz, F., Do, T., 2009. Shape-controlled synthesis of highly crystalline titania nanocrystals. ACS Nano 3, 3737–43. doi:10.1021/nn900940p

Dowling, A., Clift, R., Grobert, N., Hutton, D., Oliver, R., O'neill, O., Pethica, J., Pidgeon, N., Porritt, J., Ryan, J., Et Al., 2004. Nanoscience and nanotechnologies: opportunities and uncertainties, The Royal Society & The Royal Academy of Engineering.

Duong, G. V., Sato Turtelli, R., Hanh, N., Linh, D. V., Reissner, M., Michor, H., Fidler, J., Wiesinger, G., Grössinger, R., 2006. Magnetic properties of nanocrystalline Co1-xZnxFe2O4 prepared by forced hydrolysis method. J. Magn. Magn. Mater. 307, 313–317. doi:10.1016/j.jmmm.2006.03.072

Dupuis, V., Gavrilov-Isaac, V., Neveu, S., Aouadi, M., Abramson, S., 2014. Synthesis And Properties Of Magnetic Nanoparticles With Tunable Magnetic Anisotropy Energy. MRS Proc. 1708, mrss14–1708–vv02–06. doi:10.1557/opl.2014.485

Fairbairn, J.J., Khan, M.W., Ward, K.J., Loveridge, B.W., Fairbairn, D.W., O'Neill, K.L., 1995. Induction of apoptotic cell DNA fragmentation in human cells after treatment with hyperthermia. Cancer Lett. 89, 183–8.

Fajardo, L.F., 1984. Pathological effects of hyperthermia in normal tissues. Cancer Res. 44, 4826s–4835s.

Fantechi, E., 2014. Magnetic nanoparticles for hyperthermic application. Università degli Studi di Firenze.

Fantechi, E., Campo, G., Carta, D., Corrias, A., de Julián Fernández, C., Gatteschi, D., Innocenti, C., Pineider, F., Rugi, F., Sangregorio, C., 2012. Exploring the Effect of Co Doping in Fine Maghemite Nanoparticles. J. Phys. Chem. C 116, 8261–8270. doi:10.1021/jp300806j

Fantechi, E., Innocenti, C., Albino, M., Lottini, E., Sangregorio, C., 2015. Influence of cobalt doping on the hyperthermic efficiency of magnetite nanoparticles. J. Magn. Magn. Mater. 380, 365–371. doi:10.1016/j.jmmm.2014.10.082

Feynman, R.P., 1959. Plenty of Room at the Bottom.

Foote, M., 2005. Oncology basics Part 1. What is cancer? J. Am. Med. Writ. Assoc. 20, 52–58.

Fortin, J.-P., Wilhelm, C., Servais, J., Ménager, C., Bacri, J.-C., Gazeau, F., 2007. Size-sorted anionic iron oxide nanomagnets as colloidal mediators for magnetic hyperthermia. J. Am. Chem. Soc. 129, 2628–35. doi:10.1021/ja067457e

Franchini, M.C., Baldi, G., Bonacchi, D., Gentili, D., Giudetti, G., Lascialfari, A., Corti, M., Marmorato, P., Ponti, J., Micotti, E., Guerrini, U., Sironi, L., Gelosa, P., Ravagli, C., Ricci, A., 2010. Bovine serum albumin-based magnetic nanocarrier for MRI diagnosis and hyperthermic therapy: A potential theranostic approach against cancer. Small 6, 366–370. doi:10.1002/smll.200901689

Freestone, I., Meeks, N., Sax, M., Higgitt, C., 2007. The Lycurgus Cup — A Roman nanotechnology. Gold Bull. 40, 270–277. doi:10.1007/BF03215599

Gavrilov-Isaac, V., Neveu, S., Dupuis, V., Talbot, D., Cabuil, V., 2014. Synthesis of Fe3O4@CoFe2O4@MnFe2O4 trimagnetic core/shell/shell nanoparticles 4–6.

Gittleman, J.I., Abeles, B., Bozowski, S., 1974. Superparamagnetism and relaxation effects in granular Ni-SiO2 and Ni-Al2O3 films. Phys. Rev. B 9, 3891–3897.

Gnanaprakash, G., Philip, J., Jayakumar, T., Raj, B., 2007. Effect of digestion time and alkali addition rate on physical properties of magnetite nanoparticles. J. Phys. Chem. B 111, 7978–7986. doi:10.1021/jp071299b

Gonzales-Weimuller, M., Zeisberger, M., Krishnan, K.M., 2009. Size-dependant heating rates of iron oxide nanoparticles for magnetic fluid hyperthermia. J. Magn. Magn. Mater. 321, 1947–1950. doi:10.1016/j.jmmm.2008.12.017

Guardia, P., Di Corato, R., Lartigue, L., Wilhelm, C., Espinosa, A., Garcia-Hernandez, M., Gazeau, F., Manna, L., Pellegrino, T., 2012. Water-soluble iron oxide nanocubes with high values of specific absorption rate for cancer cell hyperthermia treatment. ACS Nano 6, 3080–91. doi:10.1021/nn2048137

Guardia, P., Riedinger, A., Nitti, S., Pugliese, G., Marras, S., Genovese, A., Materia, M.E., Lefevre, C., Manna, L., Pellegrino, T., 2014. One pot synthesis of monodisperse water soluble iron oxide nanocrystals with high values of the specific absorption rate. J. Mater. Chem. B 2, 4426. doi:10.1039/c4tb00061g

Harmon, B.V., Takano, Y.S., Winterford, C.M., Gobé, G.C., 1991. The Role of Apoptosis in the Response

of Cells and Tumours to Mild Hyperthermia. Int. J. Radiat. Biol. 59, 489–501. doi:10.1080/09553009114550441

Hasegawa, R., Ray, R., 2014. Low-temperature magnetizaztion study of crystalline and glasyy Fe-B alloys. Phys. Rev. B 20, 211–214. doi:10.1007/s13398-014-0173-7.2

Hergt, R., Dutz, S., 2007. Magnetic particle hyperthermia—biophysical limitations of a visionary tumour therapy. J. Magn. Magn. Mater. 311, 187–192. doi:10.1016/j.jmmm.2006.10.1156

Hergt, R., Dutz, S., Zeisberger, M., 2010. Validity limits of the Néel relaxation model of magnetic nanoparticles for hyperthermia. Nanotechnology 21, 015706. doi:10.1088/0957-4484/21/1/015706

Hergt, R., Hiergeist, R., Zeisberger, M., Schüler, D., Heyen, U., Hilger, I., Kaiser, W. a., 2005. Magnetic properties of bacterial magnetosomes as potential diagnostic and therapeutic tools. J. Magn. Magn. Mater. 293, 80–86. doi:10.1016/j.jmmm.2005.01.047

Hervault, A., Thanh, N.T.K., 2014. Magnetic nanoparticle-based therapeutic agents for thermo-chemotherapy treatment of cancer. Nanoscale 6, 11553–73. doi:10.1039/c4nr03482a

Hessel, C.M., Pattani, V.P., Rasch, M., Panthani, M.G., Koo, B., Tunnell, J.W., Korgel, B.A., 2011. Copper selenide nanocrystals for photothermal therapy. Nano Lett. 11, 2560–6. doi:10.1021/nl201400z

Hildebrandt, B., Wust, P., Ahlers, O., Dieing, A., Sreenivasa, G., Kerner, T., Felix, R., Riess, H., 2002. The cellular and molecular basis of hyperthermia. Crit. Rev. Oncol. Hematol. 43, 33–56.

Hilger, I., Andrä, W., Hergt, R., Hiergeist, R., Schubert, H., Kaiser, W. a, 2001. Electromagnetic heating of breast tumors in interventional radiology: in vitro and in vivo studies in human cadavers and mice. Radiology 218, 570–575. doi:10.1148/radiology.218.2.r01fe19570

Hochepied, J.F., Bonville, P., Pileni, M.P., 2000. Nonstoichiometric Zinc Ferrite Nanocrystals: Syntheses and Unusual Magnetic Properties. J. Phys. Chem. B 104, 905–912. doi:10.1021/jp991626i

http://www.magforce.de/en/home.html [WWW Document], n.d. URL http://www.magforce.de/en/home.html

Hu, L., Montferrand, C. De, Lalatonne, Y., Motte, L., Brioude, A., 2012. Effect of Cobalt Doping Concentration on the Crystalline Structure and Magnetic Properties of Monodisperse $Co_x Fe_{3-x} O_4$ Nanoparticles within Nonpolar and Aqueous Solvents. J. Phys. Chem. C 116, 4349. doi:10.1021/jp205088x

Hugounenq, P., Levy, M., Alloyeau, D., Lartigue, L., Dubois, E., Cabuil, V., Ricolleau, C., Roux, S., Wilhelm, C., Gazeau, F., Bazzi, R., 2012. Iron Oxide Monocrystalline Nanoflowers for Highly Efficient Magnetic Hyperthermia. J. Phys. Chem. C 116, 15702–15712. doi:10.1021/jp3025478

Hyeon, T., Lee, S.S., Park, J., Chung, Y., Na, H.B., 2001. Synthesis of highly crystalline and monodisperse

maghemite nanocrystallites without a size-selection process. J. Am. Chem. Soc. 123, 12798–801.

Ibrahim, E.M.M., Hampel, S., Wolter, a. U.B., Kath, M., El-Gendy, a. a., Klingeler, R., Täschner, C., Khavrus, V.O., Gemming, T., Leonhardt, A., Büchner, B., 2012. Superparamagnetic FeCo and FeNi Nanocomposites Dispersed in Submicrometer-Sized C Spheres. J. Phys. Chem. C 116, 22509–22517. doi:10.1021/jp304236x

Iyer, A.K., Khaled, G., Fang, J., Maeda, H., 2006. Exploiting the enhanced permeability and retention effect for tumor targeting. Drug Discov. Today 11, 812–8. doi:10.1016/j.drudis.2006.07.005

Jadhav, S.S., Shirsath, S.E., Patange, S.M., Jadhav, K.M., 2010. Effect of Zn substitution on magnetic properties of nanocrystalline cobalt ferrite. J. Appl. Phys. 108, 093920. doi:10.1063/1.3499346

Jadhav, N. V, Prasad, A.I., Kumar, A., Mishra, R., Dhara, S., Babu, K.R., Prajapat, C.L., Misra, N.L., Ningthoujam, R.S., Pandey, B.N., Vatsa, R.K., 2013. Synthesis of oleic acid functionalized Fe3O4 magnetic nanoparticles and studying their interaction with tumor cells for potential hyperthermia applications. Colloids Surf. B. Biointerfaces 108, 158–68. doi:10.1016/j.colsurfb.2013.02.035

Jia, X., Chen, D., Jiao, X., He, T., Wang, H., Jiang, W., 2008. Monodispersed Co , Ni-Ferrite Nanoparticles with Tunable Sizes : Controlled Synthesis , Magnetic Properties , and Surface Modification Monodispersed Co , Ni-Ferrite Nanoparticles with Tunable Sizes : Controlled Synthesis ,. J. Phys. Chem. C 112, 911–917. doi:10.1021/jp077019

Jordan, A., Scholz, R., Wust, P., Fähling, H., 1999. Magnetic fluid hyperthermia (MFH): Cancer treatment with AC magnetic field induced excitation of biocompatible superparamagnetic nanoparticles. J. Magn. Magn. Mater. 201, 413–419. doi:10.1016/S0304-8853(99)00088-8

Jordan, A., Wust, P., Fählin, H., John, W., Hinz, A., Felix, R., 1993. Inductive heating of ferrimagnetic particles and magnetic fluids: Physical evaluation of their potential for hyperthermia. Int. J. Hyperth. 9, 51–68. doi:10.3109/02656739309061478

Joshi, H.M., Lin, Y.P., Aslam, M., Prasad, P. V, Schultz-Sikma, E. a., Edelman, R., Meade, T., Dravid, V.P., 2009. Effects of shape and size of cobalt ferrite nanostructures on their MRI contrast and thermal activation. J. Phys. Chem. C 113, 17761–17767. doi:10.1021/jp905776g

Kallumadil, M., Tada, M., Nakagawa, T., Abe, M., Southern, P., Pankhurst, Q. a., 2009. Suitability of commercial colloids for magnetic hyperthermia. J. Magn. Magn. Mater. 321, 1509–1513. doi:10.1016/j.jmmm.2009.02.075

Kerr, J.F., Wyllie, A.H., Currie, A.R., 1972. Apoptosis: a basic biological phenomenon with wide-ranging implications in tissue kinetics. Br. J. Cancer 26, 239–57. doi:10.1111/j.1365-2796.2005.01570.x

Kikuchi, T., Kasuya, R., Endo, S., Nakamura, A., Takai, T., Metzler-Nolte, N., Tohji, K., Balachandran, J., 2011. Preparation of magnetite aqueous dispersion for magnetic fluid hyperthermia. J. Magn.

Magn. Mater. 323, 1216–1222. doi:10.1016/j.jmmm.2010.11.009

Kim, D.-H., Nikles, D.E., Johnson, D.T., Brazel, C.S., 2008. Heat generation of aqueously dispersed CoFe2O4 nanoparticles as heating agents for magnetically activated drug delivery and hyperthermia. J. Magn. Magn. Mater. 320, 2390–2396. doi:10.1016/j.jmmm.2008.05.023

Kim, M., Kim, C.S., Kim, H.J., Yoo, K.-H., Hahn, E., 2013. Effect hyperthermia in CoFe2O4@MnFe2O4 nanoparticles studied by using field-induced Mössbauer spectroscopy. J. Korean Phys. Soc. 63, 2175–2178. doi:10.3938/jkps.63.2175

Kishimoto, M., Sueyoshi, T., Hirata, J., Amemiya, M., Hayama, F., 1979. Coercivity of γ-Fe2O3 particles growing iron-cobalt ferrite. J. Appl. Phys. 50, 450. doi:10.1063/1.325632

Kita, E., Hashimoto, S., Kayano, T., Minagawa, M., Yanagihara, H., Kishimoto, M., Yamada, K., Oda, T., Ohkohchi, N., Takagi, T., Kanamori, T., Ikehata, Y., Nagano, I., 2010. Heating characteristics of ferromagnetic iron oxide nanoparticles for magnetic hyperthermia. J. Appl. Phys. 107, 09B321. doi:10.1063/1.3355917

Kline, T.L., Xu, Y.-H., Jing, Y., Wang, J.-P., 2009. Biocompatible high-moment FeCo-Au magnetic nanoparticles for magnetic hyperthermia treatment optimization. J. Magn. Magn. Mater. 321, 1525–1528. doi:10.1016/j.jmmm.2009.02.079

Krishnan, K.M., 2010. Biomedical Nanomagnetics: A Spin Through Possibilities in Imaging, Diagnostics, and Therapy. IEEE Trans. Magn. 46, 2523–2558. doi:10.1109/TMAG.2010.2046907

Kwon, S.G., Hyeon, T., 2008a. Colloidal chemical synthesis and formation kinetics of uniformly sized nanocrystals of metals, oxides, and chalcogenides. Acc. Chem. Res. 41, 1696–709. doi:10.1021/ar8000537

Kwon, S.G., Hyeon, T., 2008b. Colloidal chemical synthesis and formation kinetics of uniformly sized nanocrystals of metals, oxides, and chalcogenides. Acc. Chem. Res. 41, 1696–709. doi:10.1021/ar8000537

Lacroix, L., Huls, N.F., Ho, D., Sun, X., Cheng, K., Sun, S., 2011. Stable single-crystalline body centered cubic Fe nanoparticles. Nano Lett. 11, 1641–5. doi:10.1021/nl200110t

Lacroix, L.-M., Malaki, R.B., Carrey, J., Lachaize, S., Respaud, M., Goya, G.F., Chaudret, B., 2009. Magnetic hyperthermia in single-domain monodisperse FeCo nanoparticles: Evidences for Stoner–Wohlfarth behavior and large losses. J. Appl. Phys. 105, 023911. doi:10.1063/1.3068195

Ladgaonkar, B.P., Vaingankar, A.S., 1998. X-ray diffraction investigation of cation distribution in CdxCu1-xFe2O4 ferrite system. Mater. Chem. Phys. 56, 280–283.

LaMer, V.K., Dinegar, R.H., 1950. Theory, Production and Mechanism of Formation of Monodispersed Hydrosols. J. Am. Chem. Soc. 72, 4847–4854. doi:10.1021/ja01167a001

Laniado, M., Chachuat, A., 1995. Compatibility profile of ENDOREM. Radiologe 35, 266–270.

Lartigue, L., Innocenti, C., Kalaivani, T., Awwad, A., Sanchez Duque, M.D.M., Guari, Y., Larionova, J.,

Guérin, C., Montero, J.-L.G., Barragan-Montero, V., Arosio, P., Lascialfari, A., Gatteschi, D., Sangregorio, C., 2011. Water-dispersible sugar-coated iron oxide nanoparticles. An evaluation of their relaxometric and magnetic hyperthermia properties. J. Am. Chem. Soc. 133, 10459–72. doi:10.1021/ja111448t

Laurent, S., Forge, D., Port, M., Roch, A., Robic, C., Vander Elst, L., Muller, R.N., 2008. Magnetic iron oxide nanoparticles: synthesis, stabilization, vectorization, physicochemical characterizations, and biological applications. Chem. Rev. 108, 2064–110. doi:10.1021/cr068445e

Lawen, A., 2003. Apoptosis-an introduction. BioEssays 25, 888–896. doi:10.1002/bies.10329

Lee, J.-H., Jang, J.-T., Choi, J.-S., Moon, S.H., Noh, S.-H., Kim, J.-G.J.-W., Kim, I.-S., Park, K.I., Cheon, J., 2011. Exchange-coupled magnetic nanoparticles for efficient heat induction. Nat. Nanotechnol. 6, 418–22. doi:10.1038/nnano.2011.95

Lepock, J.R., 2003. Cellular effects of hyperthermia: relevance to the minimum dose for thermal damage. Int. J. Hyperth. 19, 252–266. doi:10.1080/0265673031000065042

Li, J., Li, J., Chen, L., Lin, Y., Liu, X., Gong, X., Li, D., 2015. Characterization and magnetism of Co-modified γ-Fe2O 3 core-shell nanoparticles by enhancement using NaOH. J. Magn. Magn. Mater. 374, 157–163. doi:10.1016/j.jmmm.2014.08.033

Lim, C.-U., Zhang, Y., Fox, M.H., 2006. Cell cycle dependent apoptosis and cell cycle blocks induced by hyperthermia in HL-60 cells. Int. J. Hyperth. 22, 77–91. doi:10.1080/02656730500430538

Lim, J., Yeap, S., Che, H., Low, S., 2013. Characterization of magnetic nanoparticle by dynamic light scattering. Nanoscale Res. Lett. 8, 381. doi:10.1186/1556-276X-8-381

Liu, C., Zou, B., Rondinone, A.J., Zhang, Z.J., 2000. Chemical Control of Superparamagnetic Properties of Magnesium and Cobalt Spinel Ferrite Nanoparticles through Atomic Level Magnetic Couplings. J. Am. Chem. Soc. 122, 6263–6267. doi:10.1021/ja000784g

Liu, X.L., Fan, H.M., Yi, J.B., Yang, Y., Choo, E.S.G., Xue, J.M., Fan, D. Di, Ding, J., 2012. Optimization of surface coating on Fe3O4 nanoparticles for high performance magnetic hyperthermia agents. J. Mater. Chem. 22, 8235. doi:10.1039/c2jm30472d

Lo, M.A., Va, C., Rivas, J., Buja, M.C., Vázquez-Vázquez, C., López-Quintela, M. a., Buján-Núñez, M.C., 2011. Finite size and surface effects on the magnetic properties of cobalt ferrite nanoparticles. J. Nanoparticle Res. 13, 1663–1676. doi:10.1007/s11051-010-9920-7

López-Ortega, A., Estrader, M., Salazar-Alvarez, G., Roca, A.G., Nogués, J., 2015a. Applications of exchange coupled bi-magnetic hard/soft and soft/hard magnetic core/shell nanoparticles. Phys. Rep. 553, 1–32. doi:10.1016/j.physrep.2014.09.007

López-Ortega, A., Lottini, E., Fernández, C. de J., Sangregorio, C., 2015b. Exploring the Magnetic Properties of Cobalt-Ferrite Nanoparticles for the Development of a Rare-Earth-Free Permanent Magnet. Chem. Mater. 27, 4048–4056. doi:10.1021/acs.chemmater.5b01034

Lutterotti, L., Scardi, P., 1990. Simultaneous structure and size–strain refinement by the Rietveld method. J. Appl. Crystallogr. 23, 246–252. doi:10.1107/S0021889890002382

Lv, Y., Yang, Y., Fang, J., Zhang, H., Peng, E., Liu, X., Xiao, W., Ding, J., 2015. Size dependent magnetic hyperthermia of octahedral Fe_3O_4 nanoparticles. RSC Adv. 5, 76764–76771. doi:10.1039/C5RA12558H

Mack, Y. Rong, P., 2000. Apoptosis induced by hyperthermia in Dunn osteosarcoma cell line in vitro. Int. J. Hyperth. 16, 19–27. doi:10.1080/026567300285394

Mazarío, E., Herrasti, P., Morales, M.P., Menéndez, N., 2012. Synthesis and characterization of $CoFe_2O_4$ ferrite nanoparticles obtained by an electrochemical method. Nanotechnology 23, 355708. doi:10.1088/0957-4484/23/35/355708

Mazario, E., Menéndez, N., Herrasti, P., Cañete, M., Connord, V., Carrey, J., 2013. Magnetic hyperthermia properties of electrosynthesized cobalt ferrite nanoparticles. J. Phys. Chem. C 117, 11405–11411. doi:10.1021/jp4023025

McNamara, K., Tofail, S. a. M., 2015. Nanosystems: the use of nanoalloys, metallic, bimetallic, and magnetic nanoparticles in biomedical applications. Phys. Chem. Chem. Phys. 17, 27981–27995. doi:10.1039/C5CP00831J

Mehdaoui, B., Meffre, A., Carrey, J., Lachaize, S., Lacroix, L.-M., Gougeon, M., Chaudret, B., Respaud, M., 2011. Optimal Size of Nanoparticles for Magnetic Hyperthermia: A Combined Theoretical and Experimental Study. Adv. Funct. Mater. 21, 4573–4581. doi:10.1002/adfm.201101243

Mehdaoui, B., Meffre, A., Lacroix, L.-M., Carrey, J., Lachaize, S., Gougeon, M., Respaud, M., Chaudret, B., 2010. Large specific absorption rates in the magnetic hyperthermia properties of metallic iron nanocubes. J. Magn. Magn. Mater. 322, L49–L52. doi:10.1016/j.jmmm.2010.05.012

Mohapatra, J., Mitra, A., Bahadur, D., Aslam, M., 2013. Surface controlled synthesis of MFe_2O_4 (M = Mn, Fe, Co, Ni and Zn) nanoparticles and their magnetic characteristics. CrystEngComm 15, 524. doi:10.1039/c2ce25957e

Mondini, S., Ferretti, A.M., Puglisi, A., Ponti, A., 2012. Pebbles and PebbleJuggler: software for accurate, unbiased, and fast measurement and analysis of nanoparticle morphology from transmission electron microscopy (TEM) micrographs. Nanoscale 4, 5356–72. doi:10.1039/c2nr31276j

Morrish, A.H., 1965. The Physical Principles of Magnetism. doi:10.1002/9780470546581

Murad, E., Johnston, J.H., 1985. Iron Oxides and Oxyhydroxides, in: Mössbauer Spectroscopy Applied to Inorganic Chemistry. pp. 507–583.

Murray, C.B., Norris, D.J., Bawendi, M.G., 1993. Synthesis and Characterization of Nearly Monodisperse CdE (E = S, Se, Te) Semiconductor Nanocrystallites. J. Am. Chem. Soc. 115, 8706–8715.

Muscas, G., Yaacoub, N., Concas, G., Sayed, F., Sayed Hassan, R., Greneche, J.M., Cannas, C., Musinu,

A., Foglietti, V., Casciardi, S., Sangregorio, C., Peddis, D., 2015. Evolution of the magnetic structure with chemical composition in spinel iron oxide nanoparticles. Nanoscale 7, 13576–13585. doi:10.1039/C5NR02723C

Nappini, S., Magnano, E., Bondino, F., Píš, I., Barla, A., Fantechi, E., Pineider, F., Sangregorio, C., Vaccari, L., Venturelli, L., Baglioni, P., 2015. Surface Charge and Coating of CoFe$_2$O$_4$ Nanoparticles: Evidence of Preserved Magnetic and Electronic Properties. J. Phys. Chem. C acs.jpcc.5b04910. doi:10.1021/acs.jpcc.5b04910

Natividad, E., Castro, M., Mediano, A., 2008. Accurate measurement of the specific absorption rate using a suitable adiabatic magnetothermal setup. Appl. Phys. Lett. 92, 093116. doi:10.1063/1.2891084

Natividad, E., Castro, M., Mediano, A., 2009. Adiabatic vs. non-adiabatic determination of specific absorption rate of ferrofluids. J. Magn. Magn. Mater. 321, 1497–1500. doi:10.1016/j.jmmm.2009.02.072

Nikam, D.S., Jadhav, S. V., Khot, V.M., Ningthoujam, R.S., Hong, C.K., Mali, S.S., Pawar, S.H., 2014. Colloidal stability of polyethylene glycol functionalized Co0.5Zn0.5Fe2O4 nanoparticles: effect of pH, sample and salt concentration for hyperthermia application. RSC Adv. 4, 12662. doi:10.1039/c3ra47319h

Noh, S.-H., Na, W., Jang, J.-T., Lee, J.-H., Lee, E.J., Moon, S.H., Lim, Y., Shin, J., Cheon, J., 2012. Nanoscale magnetism control via surface and exchange anisotropy for optimized ferrimagnetic hysteresis. Nano Lett. 12, 3716–21. doi:10.1021/nl301499u

Pan, D., An, L., Sun, Z., Hou, W., Yang, Y., Yang, Z., Lu, Y., 2008. Synthesis of Cu-In-S ternary nanocrystals with tunable structure and composition. J. Am. Chem. Soc. 130, 5620–1. doi:10.1021/ja711027j

Pankhurst, Q. a, Connolly, J., Jones, S.K., Dobson, J., 2003. Applications of magnetic nanoparticles in biomedicine. J. Phys. D. Appl. Phys. 36, R167–R181. doi:10.1088/0022-3727/36/13/201

Papadimitriou, J.M., Van Bruggen, I., 1993. Quantitative Investigations of Apoptosis of Murine Mononuclear Phagocytes during Mild Hyperthermia. Exp. Mol. Pathol. 59, 1–12. doi:10.1006/exmp.1993.1022

Park, J., Joo, J., Kwon, S.G., Jang, Y., Hyeon, T., 2007. Synthesis of monodisperse spherical nanocrystals. Angew. Chem. Int. Ed. Engl. 46, 4630–60. doi:10.1002/anie.200603148

Park, S., Kim, S., Lee, S., Khim, Z.G., Char, K., Hyeon, T., 2000. Synthesis and Magnetic Studies of Uniform Iron Nanorods and Nanospheres. J. Am. Chem. Soc. 122, 8581–8582. doi:10.1021/ja001628c

Peddis, D., Cannas, C., Musinu, A., Ardu, A., Orrù, F., Fiorani, D., Laureti, S., Rinaldi, D., Muscas, G., Concas, G., Piccaluga, G., 2013. Beyond the Effect of Particle Size: Influence of CoFe2O4 Nanoparticle Arrangements on Magnetic Properties. Chem. Mater. 25, 2005–2013.

doi:10.1021/cm303352r

Peddis, D., Rinaldi, D., Ennas, G., Scano, A., Agostinelli, E., Fiorani, D., 2012. Superparamagnetic blocking and superspin-glass freezing in ultra small δ-(Fe(0.67)Mn(0.33))OOH particles. Phys. Chem. Chem. Phys. 14, 3162–9. doi:10.1039/c2cp22473a

Peddis, D., Yaacoub, N., Ferretti, M., Martinelli, A., Piccaluga, G., Musinu, A., Cannas, C., Navarra, G., Greneche, J.M., Fiorani, D., 2011. Cationic distribution and spin canting in CoFe2O4 nanoparticles. J. Phys. Condens. Matter 23, 426004. doi:10.1088/0953-8984/23/42/426004

Pichon, B.P., Gerber, O., Lefevre, C., Florea, I., Fleutot, S., Baaziz, W., Pauly, M., Ohlmann, M., Ulhaq, C., Ersen, O., Pierron-Bohnes, V., Panissod, P., Drillon, M., Begin-Colin, S., 2011. Microstructural and Magnetic Investigations of Wüstite-Spinel Core-Shell Cubic-Shaped Nanoparticles. Chem. Mater. 23, 2886–2900. doi:10.1021/cm2003319

Pradhan, P., Giri, J., Samanta, G., Sarma, H.D., Mishra, K.P., Bellare, J., Banerjee, R., Bahadur, D., 2007. Comparative evaluation of heating ability and biocompatibility of different ferrite-based magnetic fluids for hyperthermia application. J. Biomed. Mater. Res. B. Appl. Biomater. 81, 12–22. doi:10.1002/jbm.b.30630

Purushotham, S., Chang, P.E.J., Rumpel, H., Kee, I.H.C., Ng, R.T.H., Chow, P.K.H., Tan, C.K., Ramanujan, R. V, 2009. Thermoresponsive core-shell magnetic nanoparticles for combined modalities of cancer therapy. Nanotechnology 20, 305101. doi:10.1088/0957-4484/20/30/305101

Rao, C.N.R., Cheetham, a K., 2001. Science and technology of nanomaterials: current status and future prospects. J. Mater. Chem. 11, 2887–2894. doi:10.1039/b105058n

Reibold, M., Pätzke, N., Levin, a. a., Kochmann, W., Shakhverdova, I.P., Paufler, P., Meyer, D.C., 2009. Structure of several historic blades at nanoscale. Cryst. Res. Technol. 44, 1139–1146. doi:10.1002/crat.200900445

Repko, A., Nižňanský, D., Matulková, I., Kalbáč, M., Vejpravová, J., 2013. Hydrothermal preparation of hydrophobic and hydrophilic nanoparticles of iron oxide and a modification with CM-dextran. J. Nanoparticle Res. 15, 1767. doi:10.1007/s11051-013-1767-2

Repko, A., Nižňanský, D., Poltierová-Vejpravová, J., 2011. A study of oleic acid-based hydrothermal preparation of CoFe2O4 nanoparticles. J. Nanoparticle Res. 13, 5021–5031. doi:10.1007/s11051-011-0483-z

Repko, A., Vejpravová, J., Vacková, T., Zákutná, D., Nižňanský, D., 2015. Oleate-based hydrothermal preparation of CoFe2O4 nanoparticles, and their magnetic properties with respect to particle size and surface coating. J. Magn. Magn. Mater. 390, 142–151. doi:10.1016/j.jmmm.2015.04.090

Riha, S.C., Parkinson, B.A., Prieto, A.L., 2009. Solution-based synthesis and characterization of Cu2ZnSnS4 nanocrystals. J. Am. Chem. Soc. 131, 12054–5. doi:10.1021/ja9044168

Roca, a. G., Morales, M.P., O'Grady, K., Serna, C.J., 2006. Structural and magnetic properties of uniform magnetite nanoparticles prepared by high temperature decomposition of organic precursors. Nanotechnology 17, 2783–2788. doi:10.1088/0957-4484/17/11/010

Roca, A.G., Marco, J.F., Del Puerto Morales, M., Serna, C.J., 2007. Effect of nature and particle size on properties of uniform magnetite and maghemite nanoparticles. J. Phys. Chem. C 111, 18577–18584. doi:10.1021/jp075133m

Roca, A.G., Niznansky, D., Poltierova-Vejpravova, J., Bittova, B., Gonzalez-Fernandez, M.A., Serna, C.J., Morales, M.P., 2009. Magnetite nanoparticles with no surface spin canting. J. Appl. Phys. 105, 114307–114309.

Rosensweig, R.E., 2002. Heating magnetic fluid with alternating magnetic field. J. Magn. Magn. Mater. 252, 370–374. doi:10.1016/S0304-8853(02)00706-0

Roti Roti, J.L., 2008. Cellular responses to hyperthermia (40–46 ° C): Cell killing and molecular events. Int. J. Hyperth. 24, 3–15. doi:10.1080/02656730701769841

Salazar-Alvarez, G., Sort, J., Uheida, A., Muhammed, M., Suriñach, S., Baró, M.D., Nogués, J., 2007. Reversible post-synthesis tuning of the superparamagnetic blocking temperature of γ-Fe 2 O 3 nanoparticles by adsorption and desorption of Co(ii) ions. J. Mater. Chem. 17, 322–328. doi:10.1039/B613026G

Sasikala, A.R.K., GhavamiNejad, A., Unnithan, A.R., Thomas, R.G., Moon, M., Jeong, Y.Y., Park, C.H., Kim, C.S., 2015. A smart magnetic nanoplatform for synergistic anticancer therapy: manoeuvring mussel-inspired functional magnetic nanoparticles for pH responsive anticancer drug delivery and hyperthermia. Nanoscale 18119–18128. doi:10.1039/C5NR05844A

Sharifi, I., Shokrollahi, H., 2012. Nanostructural, magnetic and Mössbauer studies of nanosized Co1−xZnxFe2O4 synthesized by co-precipitation. J. Magn. Magn. Mater. 324, 2397–2403. doi:10.1016/j.jmmm.2012.03.008

Shchepotin, I.B., Soldatenkov, V., Wroblewski, J.T., Surin, A., Shabahang, M., Buras, R.R., Nauta, R.J., Pulyaeva, H., Evans, S.R.T., 1997. Apoptosis induced by hyperthermia and verapamil in vitro in a human colon cancer cell line. Int. J. Hyperth. 13, 547–557. doi:10.3109/02656739709023553

Shete, P.B., Patil, R.M., Thorat, N.D., Prasad, A., Ningthoujam, R.S., Ghosh, S.J., Pawar, S.H., 2014. Magnetic chitosan nanocomposite for hyperthermia therapy application: Preparation, characterization and in vitro experiments. Appl. Surf. Sci. 288, 149–157. doi:10.1016/j.apsusc.2013.09.169

Shliomis, M.I., 1974. Magnetic fluids. Sov. Phys. Uspekhi 17, 153–169. doi:10.1070/PU1974v017n02ABEH004332

Sickafus, K.E., Wills, J.M., Grimes, N.W., 2004. Structure of Spinel. J. Am. Ceram. Soc. 82, 3279–

3292. doi:10.1111/j.1151-2916.1999.tb02241.x

Singhal, S., Namgyal, T., Bansal, S., Chandra, K., 2010. Effect of Zn Substitution on the Magnetic Properties of Cobalt Ferrite Nano Particles Prepared Via Sol-Gel Route. J. Electromagn. Anal. Appl. 2, 376–381. doi:10.4236/jemaa.2010.26049

Smit, J., Wijn, H.P.J., 1959. Ferrites. Philips' Technical Library.

Song, C.W., 1984. Effect of Local Hyperthermia on Blood Flow and Microenvironment: A Review. Cancer Res. 44, 4721–4730.

Song, C.W., Park, H., Griffin, R.J., 2001. Improvement of Tumor Oxygenation by Mild Hyperthermia. Radiat. Res. 155, 515–528. doi:10.1667/0033-7587(2001)155[0515:IOTOBM]2.0.CO;2

Song, M., Zhang, Y., Hu, S., Song, L., Dong, J., Chen, Z., Gu, N., 2012. Influence of morphology and surface exchange reaction on magnetic properties of monodisperse magnetite nanoparticles. Colloids Surfaces A Physicochem. Eng. Asp. 408, 114–121. doi:10.1016/j.colsurfa.2012.05.039

Song, Q., Zhang, Z.J., 2004. Shape control and associated magnetic properties of spinel cobalt ferrite nanocrystals. J. Am. Chem. Soc. 126, 6164–8. doi:10.1021/ja049931r

Song, Q., Zhang, Z.J., 2006. Correlation between spin-orbital coupling and the superparamagnetic properties in magnetite and cobalt ferrite spinel nanocrystals. J. Phys. Chem. B 110, 11205–9. doi:10.1021/jp060577o

Song, Q., Zhang, Z.J., 2012. Controlled synthesis and magnetic properties of bimagnetic spinel ferrite CoFe2O4 and MnFe2O4 nanocrystals with core-shell architecture. J. Am. Chem. Soc. 134, 10182–90. doi:10.1021/ja302856z

Stauffer, P.R., Cetas, T.C., Fletcher, a M., DeYoung, D.W., Dewhirst, M.W., Oleson, J.R., Roemer, R.B., 1984. Observations on the use of ferromagnetic implants for inducing hyperthermia. IEEE Trans. Biomed. Eng. 31, 76–90. doi:10.1109/TBME.1984.325373

Strohbehn, J.W., Douple, E.B., 1984. Hyperthermia and cancer therapy: a review of biomedical engineering contributions and challenges. IEEE Trans. Biomed. Eng. 31, 779–87. doi:10.1109/TBME.1984.325238

Sudakar, C., Kutty, T.R.., 2004. Structural and magnetic characteristics of cobalt ferrite-coated nano-fibrous γ-Fe2O3. J. Magn. Magn. Mater. 279, 363–374. doi:10.1016/j.jmmm.2004.02.005

Sun, S., Zeng, H., Robinson, D.B., Raoux, S., Rice, P.M., Wang, S.X., Li, G., 2004. Monodisperse MFe2O4 (M=Fe, Co, Mn) Nanoparticles. J. Am. Chem. Soc. 126, 273–279.

Suto, M., Hirota, Y., Mamiya, H., Fujita, A., Kasuya, R., Tohji, K., Jeyadevan, B., 2009. Heat dissipation mechanism of magnetite nanoparticles in magnetic fluid hyperthermia. J. Magn. Magn. Mater. 321, 1493–1496. doi:10.1016/j.jmmm.2009.02.070

Takano, Y.S., Harmon, B. V, Kerr, J.F., 1991. Apoptosis induced by mild hyperthermia in human and murine tumour cell lines: a study using electron microscopy and DNA gel electrophoresis. J. Pathol.

163, 329–36. doi:10.1002/path.1711630410

Taylor, R.M., 1974. Maghemite in Soils and Its Origin I. PROPERTIES AND OBSERVATIONS ON SOIL MAGHEMITES. Clay Miner. 10, 289–298. doi:10.1180/claymin.1974.010.4.08

Thanh, N.T.K., Dung, N.T., Tung, L.D., Thanh, C.T., Ong, Q.K., Chuc, N. Van, Maenosono, S., Lu, L.T., 2015. Synthesis of magnetic cobalt ferrite nanoparticles with controlled morphology, monodispersity and composition: the influence of solvent, surfactant, reductant and synthetic condition. Nanoscale 19596–19610. doi:10.1039/C5NR04266F

Thuy, T.T., Maenosono, S., Thanh, N.T.K., 2012. Next Generation Magnetic Nanoparticles for Biomedical Applications, in: Magnetic Nanoparticles: From Fabrication to Clinical Applications. pp. 99–126.

Tian, Y., Yu, B., Li, X., Li, K., 2011. Facile solvothermal synthesis of monodisperse Fe3O4 nanocrystals with precise size control of one nanometre as potential MRI contrast agents. J. Mater. Chem. 21, 2476. doi:10.1039/c0jm02913k

Topkaya, R., Baykal, A., Demir, A., 2012. Yafet–Kittel-type magnetic order in Zn-substituted cobalt ferrite nanoparticles with uniaxial anisotropy. J. Nanoparticle Res. 15, 1359. doi:10.1007/s11051-012-1359-6

Torres, T.E., Roca, a G., Morales, M.P., Ibarra, A., Marquina, C., Ibarra, M.R., Goya, G.F., 2010. Magnetic properties and energy absorption of CoFe 2 O 4 nanoparticles for magnetic hyperthermia. J. Phys. Conf. Ser. 200, 072101. doi:10.1088/1742-6596/200/7/072101

van Bruggen, I., Robertson, T.A., Papadimitriou, J.M., 1991. The effect of mild hyperthermia on the morphology and function of murine resident peritoneal macrophages. Exp. Mol. Pathol. 55, 119–134. doi:10.1016/0014-4800(91)90047-2

van der Zee, J., 2002. Heating the patient: a promising approach? Ann. Oncol. 13, 1173–1184. doi:10.1093/annonc/mdf280

van Ewijk, G. a., Vroege, G.J., Philipse, a. P., 1999. Convenient preparation methods for magnetic colloids. J. Magn. Magn. Mater. 201, 31–33. doi:10.1016/S0304-8853(99)00080-3

Varshney, D., Verma, K., Kumar, A., 2011. Substitutional effect on structural and magnetic properties of AxCo1−xFe2O4 (A=Zn, Mg and x=0.0, 0.5) ferrites. J. Mol. Struct. 1006, 447–452. doi:10.1016/j.molstruc.2011.09.047

Vegard, L., 1921. Die Konstitution der Mischkristalle und die Raumfüllung der Atome. Zeitschrift für Phys. 5, 17–26. doi:10.1007/BF01349680

Vestal, C.R., Zhang, Z.J., 2003. Effects of surface coordination chemistry on the magnetic properties of MnFe(2)O(4) spinel ferrite nanoparticles. J. Am. Chem. Soc. 125, 9828–33. doi:10.1021/ja035474n

Veverka, M., Veverka, P., Jirák, Z., Kaman, O., Knížek, K., Maryško, M., Pollert, E., Závěta, K., 2010.

Synthesis and magnetic properties of Co1−xZnxFe2O4+γ nanoparticles as materials for magnetic fluid hyperthermia. J. Magn. Magn. Mater. 322, 2386–2389. doi:10.1016/j.jmmm.2010.02.042

Vichery, C., Maurin, I., Boilot, J.-P., Gacoin, T., 2012. Post-synthesis heat treatments of γ-Fe2O3 nanoparticles embedded in a refractory matrix: From annealing of structural defects to doping. J. Appl. Phys. 111, 07B541. doi:10.1063/1.3680539

Vichery, C., Maurin, I., Proux, O., Kieffer, I., Hazemann, J.-L., Cortès, R., Boilot, J.-P., Gacoin, T., 2013. Introduction of Cobalt Ions in γ-Fe2O3 Nanoparticles by Direct Coprecipitation or Postsynthesis Adsorption: Dopant Localization and Magnetic Anisotropy. J. Phys. Chem. C 3, 130918100525007. doi:10.1021/jp405450p

Walker, M., Mayo, P.I., O'Grady, K., Charles, S.W., Chantrell, R.W., 1993. The magnetic properties of single-domain particles with cubic anisotropy. I. Hysteresis loops. J. Phys. Condens. Matter 5, 2779–2792. doi:10.1088/0953-8984/5/17/012

Wang, H., Shrestha, T.B., Basel, M.T., Dani, R.K., Seo, G., Balivada, S., Pyle, M.M., Prock, H., Koper, O.B., Thapa, P.S., Moore, D., Li, P., Chikan, V., Troyer, D.L., Bossmann, S.H., 2012. Magnetic-Fe/Fe(3)O(4)-nanoparticle-bound SN38 as carboxylesterase-cleavable prodrug for the delivery to tumors within monocytes/macrophages. Beilstein J. Nanotechnol. 3, 444–55. doi:10.3762/bjnano.3.51

Wang, X., Zhuang, J., Peng, Q., Li, Y., 2005. A general strategy for nanocrystal synthesis. Nature 437, 121–4. doi:10.1038/nature03968

Weiss, P., 1907. The molecular field hypothesis and ferromagnetism. J. Phys. Radium 6, 661.

White, W.B., DeAngelis, B.A., 1967. Interpretation of the vibrational spectra of spinels. Spectrochim. Acta Part A Mol. Spectrosc. 23, 985–995. doi:10.1016/0584-8539(67)80023-0

Wildeboer, R.R., Southern, P., Pankhurst, Q.A., 2014. On the reliable measurement of specific absorption rates and intrinsic loss parameters in magnetic hyperthermia materials. J. Phys. D. Appl. Phys. 47, 495003. doi:10.1088/0022-3727/47/49/495003

Wolska, E., Riedel, E., Wolski, W., 1992. The Evidence of Cd2+xFe1−x3+[Ni1−x2+Fe1+x3+]O4 Cation Distribution Based on X-Ray and Mössbauer Data. Phys. Status Solidi 132, K51–K56. doi:10.1002/pssa.2211320137

World Health Organisation, 2015. Cancer [WWW Document]. Media Cent. URL http://www.who.int/mediacentre/factsheets/fs297/en/

Yoo, D., Lee, J.-H., Shin, T.-H., Cheon, J., 2011. Theranostic magnetic nanoparticles. Acc. Chem. Res. 44, 863–74. doi:10.1021/ar200085c

Young, R.A., Wiles, D.B., 1982. Profile shape functions in Rietveld refinements. J. Appl. Crystallogr. 15, 430–438. doi:10.1107/S002188988201231X

Zeisberger, M., Dutz, S., Müller, R., Hergt, R., Matoussevitch, N., Bönnemann, H., 2007. Metallic cobalt nanoparticles for heating applications. J. Magn. Magn. Mater. 311, 224–227. doi:10.1016/j.jmmm.2006.11.178

Zeng, Q., Baker, I., Loudis, J. a., Liao, Y., Hoopes, P.J., Weaver, J.B., 2007. Fe/Fe oxide nanocomposite particles with large specific absorption rate for hyperthermia. Appl. Phys. Lett. 90, 233112. doi:10.1063/1.2746064

Zhang, L.-Y., Gu, H.-C., Wang, X.-M., 2007. Magnetite ferrofluid with high specific absorption rate for application in hyperthermia. J. Magn. Magn. Mater. 311, 228–233. doi:10.1016/j.jmmm.2006.11.179

Zhen, G., Muir, B.W., Moffat, B. a., Harbour, P., Murray, K.S., Moubaraki, B., Suzuki, K., Madsen, I., Agron-Olshina, N., Waddington, L., Mulvaney, P., Hartley, P.G., 2011. Comparative Study of the Magnetic Behavior of Spherical and Cubic Superparamagnetic Iron Oxide Nanoparticles. J. Phys. Chem. C 115, 327–334. doi:10.1021/jp104953z

Zi, Z., Sun, Y., Zhu, X., Yang, Z., Dai, J., Song, W., 2009. Synthesis and magnetic properties of CoFe2O4 ferrite nanoparticles. J. Magn. Magn. Mater. 321, 1251–1255. doi:10.1016/j.jmmm.2008.11.004